

**Dosimetric Analysis of a Laser Accelerated Electron
Beam and Optimization of FBX Chemical Dosimeter**

by
Róbert Polanek

PhD Thesis

Szeged
2020

Dosimetric Analysis of a Laser Accelerated Electron Beam and Optimization of FBX Chemical Dosimeter

by
Róbert Polanek

Supervisor:
Dr. Katalin Hideghéty

A thesis presented for the degree of
Doctor of Philosophy



University of Szeged
Doctoral School of Clinical Medicine

Department of Oncotherapy & ELI-ALPS Szeged

Szeged
2020

For the birth of something new, there has to be a happening. Newton saw an apple fall; James Watt watched a kettle boil; Roentgen fogged some photographic plates. And these people knew enough to translate ordinary happenings into something new...

Sir Alexander Fleming

Abstract

Cancer is the second leading cause of death worldwide, and it has become a global social and economic problem due to the continuous rise in incidence and mortality. Traditionally, there are three major treatment modalities for cancer diseases: surgery, radiotherapy and systematic therapy (chemo-, hormon-, immunotherapy).

Radiation therapy is applied during the course of disease management in 70% of cancer cases and the number of radiation treatments have been growing due to increasingly efficient treatment methods, precise and homogenous dose delivery. In fact, we may claim that the number of treated cases is limited by the quantity of available radiotherapy equipment and/or the relative costs of treatment.

Beside the classical particle acceleration techniques, laser wakefield acceleration (LWFA) offers a promising compact solution for the production of high and very high energy electron (VHEE) beams, which have an ultrashort pulse duration with a high instantaneous dose rate and small source size. These unique properties are of radiobiological as well as clinical interest.

This thesis is focused on the potential application of high repetition rate LWFA electron beams for radiotherapy. On the basis of particle-in-cell and Monte Carlo simulations it is expected that using a commercially available 1 kHz laser system we can generate electron beams with 35.7 MeV mean energy and 3 pC electron bunch charge at 1 kHz repetition rate to deliver a dose rate of 18 Gy/min.

This electron beam could be extremely useful for real radiotherapy applications. Thanks to the high repetition rate, dose delivery can be performed with high precision making this system a reliable alternative to conventional clinical electron accelerators.

The success of radiation therapy crucially depends on the accuracy of dose delivery to the target volume. For this reason radiation dosimetry plays an important role in the successful and safe use of radiotherapy procedures. The consistency and accuracy of the applied dosimetry methods pre-define the outcomes of these applications.

This thesis presents a version of the well-known ferrous sulfate – benzoic acid – xylenol orange (FBX) chemical dosimeter with improved sensitivity, accuracy and precision. Sensitivity is increased due to a slight modification in composition and the preparation procedures. We use stock solutions for the preparation of the dosimeter solution, which consists of 1 mM ferrous sulphate and 16 mM benzoic acid with 0.25 mM xylenol orange added post-irradiation. The nonlinear response to the absorbed dose of this system is eliminated by the increased ferrous sulphate concentration, permitting the calculation of the absorbed dose by a linear relationship between the absorbed dose and the optical absorbance of the solution.

The measured chemical yield of our dosimeter is $9.08 \cdot 10^{-6}$ mol/J for 6 MV photon beams and $6.42 \cdot 10^{-6}$ mol/J for 250 kVp x-rays. This is a 24% enhancement over the original FBX solution, which permits a finer dose resolution.

The accuracy and precision of this method is assured by a well-designed and consistently used practice. A custom-designed multipurpose PMMA slab phantom was used for irradiation in reference conditions. This phantom can be used for irradiation in reference conditions of dosimetric solutions, dosimetric films and chemical or biological samples.

The combined standard uncertainty of this system is 1.12 %, which can be improved by using an appropriate temperature correction factor. Furthermore, a working protocol has been established which allows dosimetry measurements using less than 1 mL dosimetric solutions.

The results of this *in silico* study represent a promising start for further scientific work on laser-driven electron source development. Further efforts are needed to choose the best beam steering solution as well as to develop the suitable beam monitoring and dosimetry system. Taking advantage of their particular future (very short pulse length, high instantaneous dose rate, narrow beam size etc.) we may be able to develop novel radiotherapy techniques such as microbeams, FLASH techniques etc. In case of the developed chemical dosimeter further work are needed to make our reference dosimetry system more widely accepted. My aim is to further optimize and refine the dosimetric characteristics and measurement practices and to ensure the reliability of this system as a reference dosimeter. It is also crucial to prove its suitability in various practical situations, especially in the dosimetry of radiobiological experiments, as well as in radiotherapy measurements. Furthermore, its suitability for measurements of beams with high instantaneous dose rate is still an open question.

Kivonat

A rosszindulatú daganatos betegségek világviszonylatban a második vezető halálok. Az esetek számának folyamatos növekedése miatt a jelenség komoly szociális és gazdasági problémát jelent szerte a világban. Kezelésükre, hagyományosan háromféle eljárást alkalmaznak: sebészeti beavatkozásokat, szisztémás terápiát és sugárterápiát. Köszönhetően a ma elérhető hatékony sugárterápiás kezelési módszereknek és technológiáknak a sugárterápia szinte az összes rákos megbetegedés kezelésénél használható. A kezelések száma folyamatosan növekszik és ebben gyakorlatilag csak a szükséges infrastruktúra és a kezelések ára szab határt.

A lézer-plazma gyorsítók, a klasszikus elektrongyorsítók mellett egy új, hatékony alternatívát nyújthatnak a nagy energiájú elektronnyalábok előállításában. Ezek az elektronforrások ultra-rövid nyaláb impulzust szolgáltatnak, ultra-nagy dózisteljesítménnyel és mikrométeres nyaláb átmérővel. Ezek az egyedi tulajdonságok új lehetőségeket nyújthatnak úgy a sugárbiológiai kutatásokban mint a sugárterápiás alkalmazások terén.

Dolgozatomban egy nagyfrekvenciás lézer-plazma gyorsító klinikai alkalmazhatóságát vizsgáltam. Particle-in-cell és Monte Carlo szimulációs módszerekkel kimutattam, hogy egy kommerciális, 1 kHz ismétlési frekvenciájú lézerrendszerrel létre lehet hozni egy 35.7 MeV átlagenergiájú elektronnyalábot, átlag 3 pC impulzustöltéssel. Ezzel a rendszerrel elérhető dózisteljesítmény 18 Gy/min. A viszonylag kis impulzusonkénti dózisonak és a nagy ismétlési frekvenciának köszönhetően a sugárdózist nagy pontossággal lehet leadni. Ezekkel a tulajdonságokkal ez a rendszer valós alternatívát jelenthet a mai, klasszikus klinikai elektrongyorsítóknak.

A sugárterápia hatékony és biztonságos alkalmazásában fontos szerepet játszanak a dozimetriai mérések. A sugárterápiás kezelés sikerének kulcsa az előírt sugárdózis nagy pontosságú leadása a céltérfogatra. Ehhez nagy pontossággal ismerni kell az alkalmazott sugárnyaláb fizikai és dozimetriai jellemzőit. Mérésükhöz, a sugárterápiás módszernek megfelelő dozimetriai rendszer szükséges, mely klinikai feltételek mellett is képes nagy pontosságú és megbízható mérési eredményeket szolgáltatni.

Dolgozatomban bemutatok egy általam kifejlesztett kémiai dozimétert, melyet olyan különleges körülmények közt is alkalmazni lehet abszolút mérésekhez, ahol más doziméterek nem vagy csak korlátozva képesek mérni. A doziméter a jól ismert FBX típusú kémiai doziméter egy továbbfejlesztett változata melynek megnövekedett érzékenységét az eredeti összetétel megváltoztatásával értem el. A mérések pontosságát és megbízhatóságát egy, az oldat előállítását valamint a mérési folyamatot leíró protokoll következetes használata biztosítja. Ehhez egy speciális PMMA fantomot terveztem mely használható a dozimetriai oldat, dozimetriai filmek, valamint kémiai vagy biológiai minták referencia körülmények közti besugarazásához.

A dozimetriai oldat új összetétele 1 mM vas-szulfát és 16 mM benzoésav 25 mM-os kénsav oldata, amihez a besugarazást követően 0.25 mM xylénol orange 25 mM-os kénsav oldatát adtam. A dozimetriai oldat előállításához törzsoldatokat használtam, így az oldat előállítása könnyebb és gyorsabb. Az oldat nemlineáris dóziszválaszát a vas-szulfát koncentrációjának növelésével küszöböltem ki, így az elnyelt dózist egy lineáris összefüggés alapján számolhatjuk ki a mért abszorpcióból.

Az új dozimetriai oldat radiokémiai hozama 6 MV fotonsugárzás esetén $9.08 \cdot 10^{-6}$ mol/J, valamint 250 kVp Röntgen sugárzás esetén $6.42 \cdot 10^{-6}$ mol/J, ami egy 24 %-os többletet jelent az eredeti FBX oldathoz képest. Ez a radiokémiai hozam növekedés érzékenyebb dóziszválaszt biztosít.

A dozimetriai rendszer kombinált standard bizonytalansága 1.12 % mely tovább csökkenthető, ha figyelembe vesszük a rendszer hőmérsékletfüggését is. Továbbá kidolgoztunk egy olyan mérési módszert is mely lehetővé teszi 1 ml-nél kisebb térfogatú dozimetriai oldatokkal való mérést is, mely sugárbiológiai mérések során jelenthet előnyt.

Ugyanakkor további kutatói és fejlesztői munkára van szükség ahhoz, hogy az általam bemutatott lézeres elektrongyorsító elérje a klinikai alkalmazások által elvárt fejlettségi szintet. Meg kell találni az optimális nyalábformáló technikát, meg kell vizsgálni az energia és intenzitás moduláció lehetőségét valamint további kutatásokra van szükség a különösen nagy dózisteljesítmény lehetséges biológiai következményeinek alapos ismeretéhez. Hasonlóképpen, további munkára van szükség ahhoz, hogy a továbbfejlesztett kémiai doziméter széles körben elfogadott legyen. Szükség van a doziméter laboratóriumok közti keresztkalibrációja, valamint minél több gyakorlati alkalmazására úgy a sugárbiológiai mint sugárterápiás gyakorlatban.

Foreword

This work has been carried out during the years 2015–2020 mainly at ELI-ALPS Research Institute, which is part of the Extreme Light Infrastructure (ELI) project, and at the Department of Oncotherapy at the University of Szeged, Faculty of Medicine.

Several laser-driven particle sources suitable for radiobiological experiments will be available at ELI-ALPS [1] in the near future. In order to exploit these sources, the Biomedical Application Research Group conducts research in the fields of radiobiology, radiotherapy and medical physics. Our research activities focus on the biological effects of laser-driven electron, ion and X-ray beams and their potential clinical applications. We aim to exploit the properties of laser-driven particle sources, improve the efficiency of radiation therapies, and to contribute to the dosimetry of such types of radiation.

Being a member of this group, I have been responsible for the preparation of the necessary technical and dosimetric conditions for future radiobiological experiments and for finding potential clinical applications of laser-driven ionizing radiation. This work involves comprehensive interdisciplinary studies and computer simulations. I have devoted particular attention to laser-driven high and very high energy electron beams, as well as to the potential applications of laser-driven ionizing radiation sources to be installed at ELI-ALPS in radiobiological and preclinical research. I specifically focus on the dosimetric properties of the laser-driven electron beam which will be powered by the high repetition rate SYLOS laser system.

During my activities I have written several Monte Carlo simulation codes using the Geant4 development framework. These simulations include the detailed description of irradiation geometry, the physics behind the interaction of ionizing radiation with matter and the analysis of the obtained data.

Due to the special properties of laser-driven ionizing radiation, the dosimetry of such radiation beams represents one of the main challenges. To contribute to this research area, I conducted experiments with the principal aim of devising a comprehensive dosimetry system for absolute measurements in reference conditions. When implemented, this system could subsequently be used in everyday radiotherapy, in radiobiological research, as well as in the dosimetry of laser-driven ionization radiation.

As a member of the research group I was also trusted with the dosimetry of radiobiological experiments and theoretical studies in collaboration with other research groups working with laser-driven ionizing radiation sources. Some of these studies were published in peer reviewed articles.

Acknowledgments

First, I wish to thank my doctoral advisor Dr. Katalin Hideghéty for giving me the opportunity to work in her group and for her advice and encouragement. I would like to thank all my co-workers for their contribution and for their help which they always offered when needed.

Special thanks go to my colleagues at the IT department for their technical support in assuring the computational infrastructure and for responding to my special requests. I would also like to thank the workshop staff for their effort in phantom development and other technical support. Special thanks go to Zoltán Vajna who has never refused my special requests.

I would like to thank Emese Fodor for her time and energy invested in explaining the secrets of treatment planning. Many thanks to Zoltán Varga PhD for his dosimetric support and his invaluable advice.

Special thanks go to Nasr Hafiz PhD for his invaluable advice and encouragement. I would also like to thank him for his support in conducting the study on the laser wakefield acceleration.

I would like to thank Zsolt Léczi PhD for his contribution in the study of laser-driven electron acceleration. I would also like to thank him for performing the PIC simulations and for his contribution to these results.

Special thanks go to Dániel Papp PhD and Christos Kamperidis PhD for their support. I am very grateful for all the time and energy they invested in our work.

I am indebted to Károly Mogyorósi for his valuable guidance and to Csaba Janáky for his technical support.

Also, I am indebted to András Fenyvesi PhD and Barna Bíró PhD from the Institute for Nuclear Research, Hungarian Academy of Sciences, Debrecen for their invaluable technical support and guidance in neutron irradiation and dosimetry.

I would also like to express my thanks to Judit Zelena for her efforts and time supporting me by proofreading our articles and my thesis.

Most of all, I would like to express my gratitude to my family. I am extremely grateful to my wife Tünde, for her support and trust. Thanks to my daughter Eszter and my son Lehel for their patience and time they accorded to me to be able to successfully finish this project.

Finally, I would like to thank my parents for their love and support. I will be eternally grateful to them for that. As a sign of gratitude I would like to dedicate this work to them.

Structure of the thesis

This thesis presents the results of two scientific works. In the introductory part I highlight the importance of radiotherapy in the modern treatment of neoplastic diseases, and then I present the current state of radiotherapy technology in general and of laser-driven particle sources in particular, and the scientific and technical barriers that need to be addressed. After briefly presenting the history of accelerators, I introduce the dosimetry framework used in this work, highlighting the expected difficulties of application in case of laser-driven particle beams.

After this introductory part, the thesis is divided into two sections. Both sections follow the standard scientific structure: each has an introductory part followed by methods, results and discussion.

The first subject presented here is the theoretical study of the dosimetric properties of high energy laser-driven electron beams. Based on this study, I have concluded that such electron beams can be useful for preclinical experiments. After further developments, such electron beams can be a potential candidate for electron source in clinical applications. The results of this work are under publication in *Nuclear Instruments and Methods in Physics Research, section A: Accelerators, Spectrometers, Detectors and Associated Equipment*.

The second subject is the development of a reliable dosimetry system applicable in radiobiological and preclinical experiments, as well as in radiotherapy measurements. It focuses on an enhanced chemical dosimetry system, suitable for dose measurements in the low dose regime, with high sensitivity and precision. The system will be suitable for the absolute dosimetry of laser-driven ionizing radiation. The result of this work appeared in the article “Improved FBX chemical dosimeter system with enhanced radiochemical yield for reference dosimetry in radiobiology and radiotherapy research”, which was published in *Radiation Physics and Chemistry* on 14 April 2020.

The thesis ends with a general conclusion, in which I summarize the main scientific achievements of my work.

Publications related to the subjects of the dissertation

- [1] R. Polanek, Z. Varga, E. Fodor, Sz. Brunner, E.R. Szabó, T. Tókécs, and K. Hideghéty. Improved fbx chemical dosimeter system with enhanced radiochemical yield for reference dosimetry in radiobiology and radiotherapy research. *Radiation Physics and Chemistry*, 174:108899, 2020. doi: 10.1016/j.radphyschem.2020.108899.
- [2] R. Polanek, Nasr A.M. Hafz, Zs. Léczi, D. Papp, C. Kamperidis, Sz. Brunner, E.R. Szabó, T. Tókécs, and K. Hideghéty. 1 kHz Laser Accelerated Electron Beam Feasible for Radiotherapy Uses: a PIC-Monte Carlo Based Study. *Nuclear Instruments and Methods in Physics Research section A: Accelerators, Spectrometers, Detectors and Associated Equipment*, 987:164841, 2021. doi: 10.1016/j.nima.2020.164841

Other publications

- [1] Thomas F. Rösch, Zoltán Szabó, Daniel Haffa, Jianhui Bin, Szilvia Brunner, Franz S. Englbrecht, Anna A. Friedl, Ying Gao, Jens Hartmann, Peter Hilz, Christian Kreuzer, Florian H. Lindner, Tobias M. Ostermayr, Róbert Polanek, Martin Speicher, Emília R. Szabó, Derya Taray, Tünde Tóké, Matthias Wür, Katia Parodi, Katalin Hideghéty, and Jörg Schreiber. A feasibility study of zebrafish embryo irradiation with laser-accelerated protons. *Review of Scientific Instruments*, 91(6):063303, 2020. doi: 10.1063/5.0008512. URL <https://doi.org/10.1063/5.0008512>.
- [2] Katalin Hideghéty, Szilvia Brunner, Andrew Cheesman, Emilia Rita Szabó, Róbert Polanek, Daniele Margarone, Tünde Tóké, and Károly Mogyorósi. ¹¹Boron delivery agents for boron proton-capture enhanced proton therapy. *Anticancer Research*, 39(5):2265–2276, 2019. doi: 10.21873/anticancer.13343. URL <https://doi.org/10.21873/anticancer.13343>.
- [3] N. Lemos, P. King, J. L. Shaw, A. L. Milder, K. A. Marsh, A. Pak, B. B. Pollock, C. Goyon, W. Schumaker, A. M. Saunders, D. Papp, R. Polanek, J. E. Ralph, J. Park, R. Tommasini, G. J. Williams, Hui Chen, F. V. Hartemann, S. Q. Wu, S. H. Glenzer, B. M. Hegelich, J. Moody, P. Michel, C. Joshi, and F. Albert. X-ray sources using a picosecond laser driven plasma accelerator. *Physics of Plasmas*, 26(8):083110, 2019. doi: 10.1063/1.5091798. URL <https://doi.org/10.1063/1.5091798>.
- [4] Melinda Katona, Tünde Tóké, Emília Rita Szabó, Szilvia Brunner, Imre Zoltán Szabó, Róbert Polanek, Katalin Hideghéty, and László G. Nyúl. *Automatic Segmentation and Quantitative Analysis of Irradiated Zebrafish Embryos*, pages 95–107. Computational Modeling of Objects Presented in Images. Fundamentals, Methods, and Applications. Springer International Publishing, 2019. doi: 10.1007/978-3-030-20805-9-9. URL <https://doi.org/10.1007/978-3-030-20805-9-9>.
- [5] Melinda Katona, Tünde Tóké, Emília Rita Szabó, Szilvia Brunner, Róbert Polanek, Katalin Hideghéty, and László Nyúl. Sugárkezelésen átesett zebrahal embriók eutomatikus morfológiai elemzése. page 21. Képfeldolgozók, és Alakfelismerők Társasága, 2019.
- [6] N Lemos, F Albert, J L Shaw, D Papp, R Polanek, P King, A L Milder, K A Marsh, A Pak, B B Pollock, B M Hegelich, J D Moody, J Park, R Tommasini, G J Williams, Hui Chen, and C Joshi. Bremsstrahlung hard x-ray source driven by an electron beam from a self-modulated laser wakefield accelerator. *Plasma Physics*

- and Controlled Fusion*, 60(5):054008, 2018. doi: 10.1088/1361-6587/aab3b5. URL <https://doi.org/10.1088/1361-6587/aab3b5>.
- [7] Szilvia Brunner, T Tokes, R Szabo, Z Szabo, Róbert Polanek, Elke Beyreuther, Jörg Pawelke, and Katalin Hideghéty. Dose-dependent changes after proton and photon irradiation in zebrafish model. In *Radiotherapy and Oncology*, volume 127, pages S587–S588. Elsevier Ireland Ltd. Elsevier House, Brookvale Plaza, East Park Shannon, CO . . . , 2018.
- [8] E. R. Szabó, Z. Reisz, R. Polanek, T. Tóké, Sz. Czifrus, Cs. Pesznyák, B. Biró, A. Fenyvesi, B. Király, J. Molnár, Sz. Brunner, B. Daroczi, Z. Varga, and K. Hideghéty. A novel vertebrate system for the examination and direct comparison of the relative biological effectiveness for different radiation qualities and sources. *International Journal of Radiation Biology*, 94(11):985–995, 2018. doi: 10.1080/09553002.2018.1511928. URL <https://doi.org/10.1080/09553002.2018.1511928>.
- [9] E.R. Szabó, T. Tóké, R. Polanek, Z. Szabó, S. Brunner, S. Czifrus, A. Fenyvesi, B. Biró, E. Beyreuther, J. Pawelke, and K. Hideghéty. Po-1043: Development of zebrafish embryo model for radiobiology research on laser driven hadron beams. *Radiotherapy and Oncology*, 127(nil):S585–S586, 2018. doi: 10.1016/s0167-8140(18)31353-7. URL [https://doi.org/10.1016/s0167-8140\(18\)31353-7](https://doi.org/10.1016/s0167-8140(18)31353-7).
- [10] K. Hideghéty, E.R. Szabó, R. Polanek, Z. Szabó, B. Ughy, S. Brunner, and T. Tóké. An evaluation of the various aspects of the progress in clinical applications of laser driven ionizing radiation. *Journal of Instrumentation*, 12(03):C03038–C03038, 2017. doi: 10.1088/1748-0221/12/03/c03038. URL <https://doi.org/10.1088/1748-0221/12/03/c03038>.
- [11] Katalin Hideghéty, Szilvia Brunner, Zoltán Imre Szabó, Emília Rita Szabó, Róbert Polanek, and Tünde Tóké. Sugárkezelés és immunterápia kombinációja. *KLINIKAI ONKOLÓGIA*, 4(2):121–129, 2017.
- [12] Katalin Hideghéty, Rita Emilia Szabó, Róbert Polanek, Zoltán Szabó, Szilvia Brunner, and Tünde Tóké. New approaches in clinical application of laser-driven ionizing radiation. In *Medical Applications of Laser-Generated Beams of Particles IV: Review of Progress and Strategies for the Future*, page nil, 5 2017. doi: 10.1117/12.2268300. URL <https://doi.org/10.1117/12.2268300>.
- [13] Polanek Robert, Szabó Emilia, Tokés Tünde, Szabó Zoltán, Kovács Máté, Flender Roland, Kiss Bálint, Ughy Bettina, Börzsönyi Ádám, and Huszár et al. Emese. Study of biological effects of femtosecond ir laser beam filamentation for cancer therapy. SPIE Optical Engineering Press, 2017, Prague.
- [14] R Polanek, E R Szabó, Z I Szabó, T Tóké, B Ughy, and B Hideghéty. Radiation dosimetry for radiobiological experiments with laser accelerated electron and ion beams. Prague, 2016.

- [15] K Hideghéty, R E Szabó, R Polanek, T Tökés, Z Szabó, and B Ughy. Potential clinical applications of laser driven ionizing radiation. Prague, 2016.
- [16] Daniel Papp, Robert Polanek, Zsolt Lecz, Luca Volpe, Alvaro Peralta Conde, and Alexander A. Andreev. A proposed 100-khz fs laser plasma hard x-ray source at the eli-alps facility. *IEEE Transactions on Plasma Science*, 44(10):2382–2392, 2016. doi: 10.1109/tps.2016.2606761. URL <https://doi.org/10.1109/tps.2016.2606761>.
- [17] Katalin Hideghéty, Rita Szabó, Bettina Ughy, Róbert Polanek, Zoltán Szabó, and Tünde Tökés. *ELI-ALPS ionizáló sugárforrások és orvosbiológiai kutatási lehetőségek*, pages 57–61. I. 2016.
- [18] Emília Rita Szabó, Imola Plangár, Tünde Tökés, Imola Mán, Róbert Polanek, Róbert Kovács, Gábor Fekete, Zoltán Szabó, Zsolt Csenki, Ferenc Baska, and Katalin Hideghéty. L-alpha glycerylphosphorylcholine as a potential radioprotective agent in zebrafish embryo model. *Zebrafish*, 13(6):481–488, 2016. doi: 10.1089/zeb.2016.1269. URL <https://doi.org/10.1089/zeb.2016.1269>.
- [19] E R Szabó, R Polanek, T Tökés, B Ughy, Z I Szabó, and K Hideghéty. Simple vertebrate model development for radiobiology research at eli-alps. Prague, 2016.
- [20] Z I Szabó, R Polanek, E R Szabó, T Tökés, K Hideghéty, and B Ughy. Microorganisms and high-dose ionizing radiations. Prague, 2016.
- [21] Róbert Polanek, Emilia Rita Szabó, and Katalin Hideghéty. Preliminary studies of radiobiological experiments with laser accelerated particle beams. RAD Association, Nis, Szerbia, 2015.
- [22] Rita Szabó Emília, Plangár Imola, Tökés Tünde, Polanek Róbert, and Hideghéty Katalin. Zebrafish embryo model for testing potential radioprotective agent. 2015.
- [23] Brinyiczki Kitti, Hideghéty Katalin, Nokta-Mán Imola, Plangár Imola, Polanek Róbert, Rita Szabó Emília, and Tökés Tünde. Preclinical model of brain radiation injury of electron beam in preparation for investigations on laser driven electrons. 2015.
- [24] E. Szabo, R. Kovács, I. Plangár, T. Tokés, R. Polanek, S.Z. Czifrus, D. Bencsik, and K. Hideghéty. Po-1074 vertebrate model to examine the biological effectiveness of different radiation qualities. *Radiotherapy and Oncology*, 115(nil):S580, 2015. doi: 10.1016/s0167-8140(15)41066-7. URL [https://doi.org/10.1016/s0167-8140\(15\)41066-7](https://doi.org/10.1016/s0167-8140(15)41066-7).
- [25] Mihaela Luminita Kiss, Marius Chirita, Corina Ana Beljung, Robert Polanek, Cecilia Savii, Adrian Ieta, and Alexandru Ionut Mihaila Chirita. Single crystalline iron oxide micrometric particles with superparamagnetic behaviour for mri applications. NSTI-Nanotech, 2014.

- [26] G Ciobanu, R Polanek, C Ciobanu, L Piros, A Birau, and V Leordean. The mass irradiation of population - a social issue. The 10th DKMT Conference on Cross-border Bioecology And Public Health, 2008.
- [27] Burlacu Ramona, Poenaru Mariana, Both Lavinia, Burlacu A, and Robert Polanek. Advantages in using a ct multislice over ct singleslice. The 10th DKMT Conference on Cross-border Bioecology And Public Health, 2008.

Contents

1	Introduction	1
1.1	Motivation	1
1.2	The technical framework of radiation therapy	2
1.3	Electron beams by laser wakefield acceleration	5
1.4	The very high energy electron therapy	7
1.5	Actual limitations of LWFA electron beams	8
1.6	Particle accelerators: a short historical overview	9
1.7	The dosimetry framework of ionizing radiation	13
1.8	Aims of the thesis	16
2	Laser driven electron beam	18
2.1	Introduction	18
2.2	The SYLOS laser system	21
2.3	Methods	21
2.4	Results and discussion	24
3	Enhanced FBX dosimeter	33
3.1	Introduction	33
3.1.1	The Fricke chemical dosimeter	33
3.1.2	The ferrous ammonium sulphate – benzoic acid – xylenol orange dosimeter	34
3.1.3	The sources of uncertainties	36
3.2	Methods	36
3.2.1	Dosimeter preparation	37
3.2.2	Reference irradiation	37
3.2.3	Spectrophotometric measurements	39
3.2.4	Density measurements	40
3.2.5	Determination of the molar mass absorption coefficient	40
3.2.6	Determining the radiochemical yield of ferric ions	40
3.2.7	Dose determination	41
3.2.8	Diluted eFBX solution measurements	41
3.3	Results and discussion	41
3.3.1	Sensitivity	41
3.3.2	The problem of nonlinearity	42

3.3.3	Radiochemical yield of ferric ions	44
3.3.4	Uncertainty budget	47
4	Conclusion and new scientific results	51

List of Figures

- 1.1 Central depth dose of different beam qualities. 3
- 1.2 Electron density distribution showing the laser pulse induced plasma bubble. Electrons are expelled to form this bubble whilst the heavier ions are practically stationary. Within this bubble, on the propagation axis, a longitudinal electric field builds up and, as a result, electrons “injected” at the back of the bubble are accelerated to highly relativistic speeds (arrow). 6
- 2.1 The semi-realistic model of irradiation geometry used in the MC simulations. The laser beam (b) enters the vacuum chamber (a) and is focused using optics (c) onto a gas jet target (d) where LWFA acceleration takes place. The accelerated electrons (f) exit the vacuum chamber through a Mylar window (e). The absorbed dose was calculated in the water phantom (g) placed at different source-to-surface distances (SSD). 22
- 2.2 (a) The energy spectra of the simulated electron beam at the acceleration site (solid line) and at the phantom surface situated at an SSD of 100 cm. The long high-energy tail of the energy spectrum is a specific feature of the self-injection mechanism. (b) The energy spectra of electrons with low energy (up to 20 MeV). They are excluded from simulations due to their large divergence. 24
- 2.3 (a) The electron beam divergence (defined as the angle between the electrons’ direction and z axis): the solid line represents the initial angular distribution while the dashed line represents the angular mean energy distribution. The dash-dotted line represents the angular distribution at the phantom surface. (b) The angular distribution – energy map of the accelerated electrons. 25
- 2.4 The absorbed dose characteristics of the unconditioned electron beam; 2.4a the dose distribution map and depth dose curve with its key characteristics: the dose maximum $D_{max} = 9.7 \text{ cGy/pC/s}$ at a depth of 1.93 cm; the therapeutic range $R_{90} = 5 \text{ cm}$ defined as the depth where the absorbed dose equals 90% of D_{max} . 2.4b the depth dose profile at the depth of the dose maximum with the full width at half maximum $FWHM = 4 \text{ cm}$ 28

2.5	Dose map, depth dose curve and dose profile at maximum dose depth, obtained with the spot scanning technique. The dose distribution was obtained by summing as many beams as necessary to produce a 20 cm × 20 cm square beam. In Fig. 2.5a it can be observed that the therapeutic range is enlarged, due to the electronic equilibrium, which is only partially realized in case of original beam.	31
2.6	The time structure of the electron bunch at 100 cm from the acceleration site and the time structure of the dose deposition events.	31
3.1	Acrylic slab phantom for reference irradiation. The phantom has two functional parts: a 30 cm × 30 cm PMMA sheet with different thicknesses for variable PMMA phantom heights (3.1b) and a PMMA sheet with thickness of 2.5 cm with a 15 cm × 15 cm and 1.5 cm deep hollow in the middle which can accept inserts with the same dimensions (3.1a). These inserts are designed to accept different types of sample holders (3.1c). Another piece of 2.5 cm thick PMMA sheet is designed to house one or two multi-well plates with dosimetric solutions or biological samples (3.1d).	38
3.2	Optical absorbance as a function of benzoic acid concentration for irradiated solution and for nonirradiated solution.	42
3.3	Dose response curve of different dosimetric solutions for a standard Fricke solution, measured with xylenol orange techniques; an FBX solution and an FB solution.	43
3.4	The effects of increased ferrous sulphate concentrations. The lower line is the graph of linear fitting of the measurement points (marked with circles) in case of eFBX solutions with 0.2 mM ferrous sulphate concentration. The dashed line is the graph of fitting with a rational function of the same measurements points. The upper line represents the graph of linear fitting of the measurements points (marked with squares) obtained with 1 mM ferrous sulphate concentration.	43
3.5	Graphical representation of absorbance variation as a function of Fe ³⁺ ion concentrations. The gradient is the molar attenuation coefficient, $\epsilon = 14615 \pm 18 \text{ M}^{-1}\text{cm}^{-1}$	45
3.6	The absorption spectra of the blank solution and of the irradiated eFBX solution. The dotted vertical lines represent the wavelengths for maximum absorptions and for the actual measurement wavelength.	47
3.7	The relative uncertainties for the eFBX dosimeter due to the photometric measurements (solid curve) and due to the combination of photometric and volume measurements (dashed line).	48

List of Tables

2.1	Key parameters and results of the simulations.	27
3.1	Phantom dose conversion factor for RW3 and PMMA materials	40
3.2	The radiochemical yield of the eFBX dosimetric solution for different beam qualities.	46
3.3	The radiochemical yield of diluted eFBX dosimetric solution for different dilutions grades. All values refer to 250 kVp X-ray beam quality.	46
3.4	Uncertainty budget of the eFBX solution. Temperature correction was calculated based on the relations used for the Fricke dosimeter[2] as the temperature dependence measurement has not yet been performed. The combined standard uncertainty without this term becomes 1.0 %.	49

Abbreviations

3DCRT three-dimensional conformal radiation therapy.

AAPM American Association of Physicists in Medicine.

BA benzoic acid.

CPA chirped pulse amplification.

eFBX enhanced FBX dosimeter.

FBX ferrous ammonium sulphate – benzoic acid – xylenol orange dosimeter.

FS ferrous ammonium sulphate.

FWHM full width at half maximum.

HPLC high-performance liquid chromatography.

HVL half value layer.

IAEA International Atomic Energy Agency.

IGRT image-guided radiation therapy.

IMRT intensity-modulated radiation therapy.

IORT intraoperative radiotherapy.

IPEM Institute of Physics and Engineering in Medicine.

LET linear energy transfer.

LINAC linear particle accelerator.

LWFA laser wakefield acceleration.

MLC multi-leaf collimator.

MRC Medical Research Council.

NIST National Institute of Standards and Technology.

OPCPA optical parametric chirped pulse amplification.

OSL optically stimulated dosimeter.

PBWA plasma beatwave acceleration.

PDA polydiacetylene.

PIC particle in cell.

PMMA Poly(methyl methacrylate).

PSDL primary standard dosimetry laboratory.

PWFA plasma wakefield acceleration.

RF radio frequency.

SSD source to surface distance.

TLD thermoluminescence dosimeter.

VHEE very high energy electron.

XO xylenol orange.

Chapter 1

Introduction

1.1 Motivation

Malignant neoplastic disease or cancer is the second leading cause of death worldwide and the number is constantly growing. In 2018 (the latest statistical year available from the Global Cancer Observatory), there were an estimated 18 million cancer cases around the world. Lung, breast, colorectal and prostate cancers are the most common cancers worldwide (each contributing 12.3%, 12.3%, 10.6% and 7.5%, respectively, to the total number of new cases diagnosed in 2018, excluding non-melanoma skin cancer; data from the Global Cancer Observatory, gco.iarc.fr).

Due to their growing number, cancer diseases have become a global social and economic problem. The costs of cancer treatments as well as the impact on the patients' ability to work prove to be a major financial blow for countries, and in some cases they can be a source of poverty. Therefore, enormous resources are channelled into cancer research to develop new techniques and modalities.

In the last few decades impressive progress has been made in the understanding and early detection of cancers, and in the various treatment modalities. These achievements have made many cancer types curable.

Traditionally, there are three major treatment modalities for cancer diseases: surgery, radiotherapy and systematic therapy. Recently, new treatment modalities have been added, such as immunotherapy or targeted therapies [3], the aim of which is to control the essential functions of the cancer cells while protecting healthy cells.

Due to their ionization potential, high-energy ionization radiation (such as X-ray or high-energy particle beams) damages the genetic material of cells, which leads to cell death by blocking the cell's ability to divide and proliferate further [4]. This property was recognized early on, and motivated curative applications immediately. Its exact pathomechanisms were not known at the time of discovery, but it was soon recognized that ionizing radiation kills normal cells too. This recognition led to the birth of radiobiology and to the systematic study of biological effects of ionizing radiations.

The principal aim of curative cancer treatment is to eradicate all tumour cells while leaving healthy cells undamaged. In radiation therapy the entire tumour can be irradiated

homogeneously with the killing doses of ionization radiation. The cell killing capability depends on the intrinsic radiation sensitivity, DNA repair capacity, repopulation, oxygenation etc.[5].

In practice, the efficacy of radiation therapy is determined by the limitations in the imaging of malignant cells (target volume definition), precision of treatment delivery (patient positioning and immobilization, dosimetry etc.), and various factors related to tumour biology (oxygenation, cell cycle distribution etc.). The increasingly sophisticated technical solutions and our growing radiobiological knowledge extensively utilize the advantages of radiation therapy.

Therefore, the importance of radiotherapy is evident and the number of radiation treatments have been growing thanks to increasingly efficient treatment methods, as well as precise and homogenous dose delivery. Radiation therapy is applied in most cancers. In fact, we may claim that the number of treated cases is limited by the quantity of available radiotherapy equipment and/or the relative costs of treatment.

1.2 The technical framework of radiation therapy

There are three ways to deliver ionizing radiation to the tumour: from the exterior of the body (external beam radiotherapy), from inside the body by inserting radioactive sources sealed in catheters (brachytherapy) and using cancer specific molecules labelled with radioactive isotopes (nuclear medicine, which is considered as a stand-alone clinical speciality).

More than 90% of the current external radiation therapies is based on photon beams due to their greater penetration compared to electron beams, which are also commonly used as a source in everyday external radiation therapy treatments. The former is used to treat deeper tumours, while electron beams are mainly used to treat tumours situated close to the body surface [6].

However, besides their high penetrability, photon beams deposit much of their energy in the surrounding healthy tissues, which leads to undesirable side effects influencing both the curative index of treatment and the prognosis of stochastic late effects. The side effects can be reduced using different treatment techniques, allowing multi-beam irradiations at different angles [7]. Using these techniques it is possible to maximize the dose in the target volume while the dose to healthy tissue is minimized, but it can never be reduced to zero.

In general, photon and electron beams are generated by linear particle accelerators (LINACs). LINACs accelerate electrons which are used directly for treatments or indirectly for the generation of X-ray radiation. The available LINAC technology has an acceptable cost and offers a compact setup with appropriate flexibility in adjusting the beam parameters (beam energy, direction, intensity etc.), which ensures the worldwide accessibility of photon based radiotherapy techniques. With LINAC based photon beams we are able to perform 3D conformal radiotherapy (3DCRT), intensity modulated radiation therapy (IMRT) or image-guided radiotherapy (IGRT) [8, 9].

However, the obvious disadvantage of photon beams led the researcher to search for other radiation types with more favourable properties. Today we are witnessing the be-

ginning of a new era represented by the use of heavy particles in radiotherapy. Heavy particles offer new opportunities to improve the quality of radiotherapy. Heavy charged particle beams such as proton or carbon ion beams have an energy deposition characteristic in tissue which is superior to single photon or electron beams (see Fig. 1.1). The depth dose curve of a monochromatic heavy charged particle beam has a relative low entrance dose region which slowly increases, and is followed by a sharp rise, called Bragg peak, near the end of its propagation. These properties lead to highly conformal dose distribution, which can be achieved with fewer proton beams.

Several studies were conducted on the biological advantages and clinical benefits of proton [10, 11, 12, 13, 14] and carbon ion [15, 16, 17] based radiotherapy.

The idea to use heavy charged particles for radiotherapy is not new. Hadron therapy was first proposed in 1946 by Wilson [18], which was followed by pioneering clinical studies [19, 11, 20, 10]. However, the technical conditions were missing and the first clinical centre with a dedicated proton accelerator facility was constructed at Loma Linda Hospital in California (USA) in 1990 [21, 22]. Until the 1990s, proton therapy was performed exclusively with particle accelerators installed in physics laboratories and used for nuclear physics research. When the efficacy of proton therapy was justified, dedicated accelerators started to emerge. There are 65 active proton therapy centres worldwide, including 24 in the USA. Nowadays hadron therapy is the primary interest for future radiotherapy techniques.

In the last decades, the number of centres and the number of treatments has grown almost exponentially, mainly due to the rapidly evolving accelerators technology. However, in spite of this rapid growth, the total number of patients receiving hadron therapy is still low compared to the number of patients treated with photon based therapies. The major drawbacks of this technique is the size and cost of construction and maintenance of such facilities.

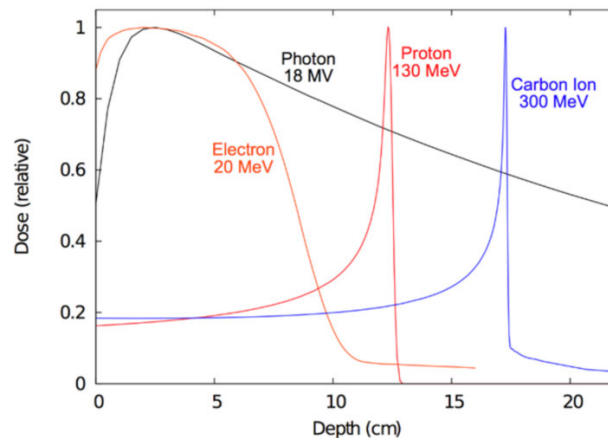


Figure 1.1: Central depth dose of different beam qualities.

Currently, the cyclotron and the synchrotron are the two reliable accelerator types for clinical hadron therapy. The choice depends on the treatment method, price and local conditions. Modern cyclotrons are small, they can be used well in relatively small

spaces, however the extraction energy of accelerated protons is fixed. The energy is spread by using a range-shifter, but this results in some degradation in beam quality. With synchrotron, the particle energy can be modulated, which offers more flexibility in beam energy modulation, but such accelerators are very large, and require a vast area for operation.

Despite the technological developments, especially in relation to synchrotrons, these accelerators have remained relatively bulky [23]. Unfortunately, due to the electrical breakdown the acceleration gradient cannot be larger than a few tens of MV/m. This implies that the diameter of a clinical accelerator ring is several tens of metres (for energies up to 400 MeV/u). The accelerator itself is installed in a separate room from where the beam is transported by the beamline equipped with large quadrupole magnets. When the beam reaches the treatment room, it must be directed towards the target volume. This is realized by a very heavy gantry system. Moreover, this gantry must be moved and positioned with sufficient precision, which requires a sophisticated mechanism and control. All these technical aspects make synchrotrons a costly investment, which in turn affects the availability of proton and ion therapy [12, 24].

Given the technical constraints of cyclotron and synchrotron based proton therapy facilities and the increased need for proton therapy, plenty of research projects aim to improve the existing accelerators technologies and develop new ones. In the last few years, these systems have become more cost-effective, and hopefully more active centres will be available in the future. At the same time, a new technology seems to be emerging using powerful lasers to accelerate particles. It is expected that this technology will significantly reduce the size of accelerators and make operation more cost-effective. The laser part can be detached from the acceleration part, which reduces the investment costs. Furthermore, the special properties of laser-driven particle beams (high dose rate, very short pulse duration etc.) may result in more effective treatment techniques.

But the laser-driven acceleration technology offers new possibilities not only for proton or heavy ion acceleration but also for electron acceleration. In fact, the acceleration of electrons is much easier and more efficient than that of heavier particles, and most of the requirements for clinical application have already been achieved. Considering the present state of the art, the laser-driven electron acceleration to energies suitable for radiation therapy is well established. This technology is capable of producing monoenergetic electron beams with small divergence and dose rates suitable for practical clinical applications. However, there is still a lot to do regarding the efficiency, stability and reliability of the acceleration process.

With this electron source it is possible to produce high-energy X-ray beams which can be used as an alternative for conventional LINAC based X-ray sources. Furthermore, a collision between the laser-driven electron bunch with another powerful laser pulse can generate quasi-monochromatic and polarized photon beams via Thomson or Compton scattering [25, 26, 27]. There are some experiments to produce a clinically usable laser-based X-ray source via Thomson scattering [28, 29], and obtain photon beams of several tens of MeV. Furthermore, an electron beam of 40 MeV can generate bremsstrahlung radiation with a strong component in the range of 10 to 20 MeV (using a tantalum foil as target). Subsequently, this radiation can be used to activate a foil of gold via the nuclear reaction $^{197}\text{Au}(\gamma, n)^{196}\text{Au}$, providing a clinically usable neutron source [30].

1.3 Electron beams by laser wakefield acceleration

The basic idea of plasma-based particle acceleration is to use intense, relativistic, longitudinal plasma waves. Consider the case in which plasma electrons are displaced from their quasi-neutral positions by an infinitesimal distance. An equal and positive charge density develops on the opposite side. The generated electric field tends to restore the equilibrium state and the electrons start to oscillate around this. The frequency of such electron oscillations depends on the electron density and is called “electron plasma frequency” or simply, plasma frequency, ω_p . If an external perturbation such as intense ultrashort laser pulse, typically generated in terawatt (TW) femtosecond (fs) laser systems, propagates through an underdense plasma (with the laser frequency larger than the plasma frequency), the laser’s ponderomotive force pushes/kicks the electrons sideways around the laser pulse and displaces them from their original locations, leaving the plasma ions unperturbed due to their heavy masses. Those displaced electrons are then electrostatically pulled back by the stationary ions creating a large amplitude plasma wave that is an intense longitudinal electric field wave in the wake of the laser pulse. Such a plasma wave (called, wakefield) propagates with a relativistic phase velocity that is the same as the laser’s propagation (group) velocity in the plasma, making such a wave ideal for particle acceleration, especially the electrons. Depending on laser and plasma parameters (peak power, focused spot size, pulse duration, electron density, interaction length, etc.), some background plasma electrons receive a sufficiently high ponderomotive kick and get trapped into the wakefield and get accelerated to relativistic energies over a short distance. Generation of multi-GeV electron beams was reported from cm-scale laser-plasma accelerators driven by sub-PW laser systems [31]. Therefore, laser-plasma accelerators provide ultrahigh gradient electron acceleration as compared to conventional RF-based linear accelerators “LINACs”, where acceleration gradients are practically limited to 10-20 MV/m, due to the electrical breakdown of the metallic accelerating cavities if the applied RF- electric field exceeds 10-20 MV/m. The electric fields of the wakefield is determined by the ambient electron number density of the plasma, through the so-called nonrelativistic wave breaking field equation:

$$E_0 = \frac{cm_e}{e}\omega_p, \quad (1.1)$$

where $\omega_p = \sqrt{4\pi n_0 e^2/m_e}$ is the electron plasma frequency, n_0 is the ambient electron number density, c is the speed of light in vacuum, m_e and e are the electron rest mass and charge, respectively. For a plasma density of $n_0 = 10^{18} \text{ cm}^{-3}$ we obtain an electric field gradient of $E_0 \simeq 96 \text{ GV/m}$, which is approximately three orders of magnitude greater than that obtained in conventional LINACs.

So far, different excitation schemes have been proposed, including *plasma wakefield acceleration (PWFA)*, *plasma beatwave acceleration (PBWA)* and *laser wakefield acceleration (LWFA)*.

In the PWFA scheme, one or more relativistic electron bunches are used to generate the plasma wave. After excitation, another pre-accelerated particle bunch is injected and accelerated by the plasma wave [32]. The concept was first proposed in 1956 [33], but for many years, maximum energy gains were moderate [34].

The PBWA scheme was proposed by Tajima and Dawson [35] as a solution to drive a plasma wakefield without using ultrashort, high-power lasers, which was not available until 1985, when the chirped pulse amplification (CPA) technique was invented. In this scheme, two long-pulse (in the range of nanoseconds) laser beams with slightly different wavelengths are used to excite the plasma wave [35]. The wavelengths of the two laser beams are tuned to ensure that the running beat-wave resonantly excites a plasma wave which can subsequently be used to accelerate injected electrons. The energy gains so obtained equal up to 28 MeV [36, 37].

In the LWFA accelerator scheme, an ultrashort, typically 30 fs (which is approximately equal to or shorter than the plasma wavelength), multi-10 TW laser pulse being focused on a gas target in a vacuum chamber [38]. The gas target (gas jet or cell), is kept at around atmospheric pressure, having an electron density of 10^{18} to 10^{20} cm^{-3} . At sufficiently high focused laser intensities (above 10^{18} W/cm^2), the laser pulse generates compressions and rarefactions of the plasma electrons around the stationary plasma ions background (Fig. 1.2), creating the wakefield or intense plasma waves, as described above [39, 40].

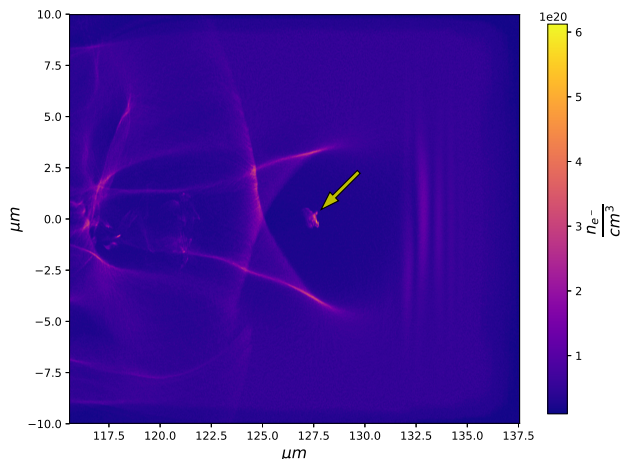


Figure 1.2: Electron density distribution showing the laser pulse induced plasma bubble. Electrons are expelled to form this bubble whilst the heavier ions are practically stationary. Within this bubble, on the propagation axis, a longitudinal electric field builds up and, as a result, electrons “injected” at the back of the bubble are accelerated to highly relativistic speeds (arrow).

LWFA electron beams have several unique properties which make them very attractive for applications in radiobiology and radiotherapy. The use of optical mirrors instead of high-power magnets provides relative flexibility in beam delivery, and offers new possibilities in facility design, cost reduction, and in the development of new radiotherapy techniques. For example, the low divergence of the generated electron beams facilitates

the formation of microbeams, which in the MeV energy range may be beneficial in cancer therapy [41] [42]. In general, an electron beam having a short bunch duration (ps at the sample position) leads to a very high instantaneous radiation dose rate. This can be useful for the state-of-the-art FLASH technique, which requires a high instantaneous dose rate. This novel radiotherapy technique seems to increase the therapeutic ratio by reducing both the acute side effects on normal tissues and late complications [43, 44]. In fact, LWFA electron bunches are extremely short; they are in the order of a few femtoseconds (fs) immediately after acceleration, which enables radiation chemists to conduct pulse radiolysis experiments at a time scale which has not been available until now [45]. Such ultrafast pulse radiolysis (also known as femtolysis) experiments significantly contribute to our understanding of the biological effects of radiation.

1.4 The very high energy electron therapy

Unlike traditional LINAC based technologies, where the achievable electron energies are limited by the technological constraints, with laser based electron acceleration it is possible to generate very high energy electrons (above 60 MeV or even above 100 MeV). These very high energy electron beams ((50-250 MeV)) have similar dosimetric properties as photon beams.

Very high energy electron (VHEE) radiation has recently emerged as a novel option for cancer radiotherapy. In spite of the fact that the laser system, the subject of this study, will probably not be able to produce very high energy electron beams, the potential of LWFA to reach such energies has motivated me to outline the concept and the benefits of this technique.

In silico studies have shown that VHEE beams have a more favourable dose distribution than advanced photon techniques, and in some situations, the results approach the charged particle therapy values. Monte Carlo simulation based plans, using electron beams with energies above 100 MeV provided a very good dose conformation, while offering significantly improved dose sparing of healthy tissue when compared to intensity modulated and volumetric arc photon therapy [46], [47], [48, 49]. VHEE plans were superior to IMRT plans, but they could also be delivered orders of magnitude faster than photon plans mainly due to higher particle production efficiency and the ability to steer charged particles in a millisecond timescale [49].

These VHEE beams with energies in the range of 150 to 250 MeV are very penetrating compared with the low energy electron beams currently used in classical radiation therapy. For example, the depth of dose maximum for an electron beam with a kinetic energy of 20 MeV is around 5 cm, while for an electron beam with 150 MeV kinetic energy it is 20 cm with a very broad depth dose curve. Furthermore, at such energies the practical range of the electron beams is larger than the patient's body, permitting the irradiation of deep situated tumours.

Additionally, the high scattering effect, characteristic of electron beams with conventional energies, can be neglected at such high energies. As a consequence, the dose perturbation effect of interface between different density is low, so the tissue heterogeneity has no effect on dose distribution [50]. Using multiple beams, higher conformity and lower

integral dose can be obtained for the same target coverage, compared to photons [51].

However, VHEE electron beams have high entrance and exit doses compared to photon beams. The high entrance dose decreases with increasing beam energies. At GeV energies this dose is lower than in the case of photon beams with conventional energies, but the depth dose increases continuously with depth, which results in a higher exit dose [52]. Recently, Kokurewicz et al. [52] have shown that focused 200 MeV and 2 GeV beams achieve highly localized dose deposition at the target depth. They have demonstrated that VHEE beams can be focused into tissue to create a high dose in small volumes with a very low dose to surrounding healthy tissues, while the entrance and exit doses are lower compared to doses achievable by collimated VHEE beams [52].

These promising clinical advantages have motivated technical development in two directions to produce clinical VHEE beams. In 2013, a Californian group developed and patented the “Pluridirectional Very High Electron Energy Radiation Therapy Systems” – a compact high-gradient electron accelerator and delivery system designed for treating patients from multiple beam directions with great speed [53].

The other approach is the high power laser plasma acceleration for VHEE generation [54, 55, 56, 57, 58, 59]. In recent years, several high power laser systems have been installed, which makes this technique available for research groups engaged in VHEE source development and preclinical investigations [60], [61].

Concurrently, there are several issues which can limit the applicability of VHEE beams in therapy. For example, neutron contamination and bremsstrahlung generation can pose serious obstacles to practical applications.

Furthermore, no suitable dosimetry protocols have been laid down, and detectors that could serve as secondary standard dosimeters for such applications have not yet been developed. Usually, detectors are calibrated for energies up to 22 MeV, and the extrapolation to higher energies is not straightforward. Recently, several theoretical studies have been dedicated to this problem. For example, Subiel et al. [62] conducted Monte Carlo simulations on the evolution of the temporal and spectral profile of 150 MeV electron beams propagating through a water phantom. Performing measurements with an ion chamber in a 165 MeV electron beam at the SPARC beamline [63] they showed that ultrashort high-dose-per-pulse VHEE beams produce significant ion recombination in the air-filled ion chamber [62]. Similar results have been obtained by McManus et al. [64] using graphite calorimetry as a primary standard and a Roos ionization chamber to determine the absolute recombination factor.

1.5 Actual limitations of LWFA electron beams

Active research in LWFA has revealed some efficiency, stability and reliability issues that need to be resolved prior to clinical implementation. Efficiency in terms of pulse charge and repetition rate ensures the necessary dose rate, which must be at least 4 Gy/min for real radiotherapy applications. The moderate stability of LWFA accelerators in terms of energy and pulse charge is the primary task which requires immediate attention before such accelerators are introduced into real radiobiological or medical applications. Furthermore, the reliability and effectiveness of beam shaping must be enhanced.

One of the main tasks is the optimization of the laser system and the target (gas-jet or solid targets), as well as their synchronization. This involves serious technological developments including mechanical, optical design as well as control and monitoring. Furthermore, we need a better understanding of the physics involved in the acceleration process. All this combined is essential to reach the highest efficiency, stability and output control. Fortunately, significant progress is being made towards stable LWFA electron beams [65, 66].

Another important issue to be studied before any clinical application is the radiobiological effects of the laser-driven particle source, especially with respect to the extremely short bunch durations in the range a few fs. Travelling towards the target, this bunch expands over the sub-ps timescale, which is by three orders of magnitude shorter than classical beams with μs bunches. This ultrashort bunch duration may involve unexpected radiobiological effects. Until now there has been no experimental evidence that higher instantaneous doserates have different biological effects with clinical consequences [67, 68, 69, 70, 71, 72, 73].

From the physics point of view, we can also expect effects which cannot be described by the classical simulation methods. The extreme particle density which can be produced with laser acceleration could lead to nonlinear effects due to the collective actions of the particles [41]. These physical consequences may affect not only radiobiological phenomena but also the dosimetry of such radiation types. Furthermore, the extremely short particle bunch duration allows for the investigation — at a very short timescale — of physical, chemical and biological processes induced by ionizing radiation, and hence it contributes to the development of femtochemistry and ultrafast radiation biology [74, 75, 76, 77].

1.6 Particle accelerators: a short historical overview

Today’s scientific advances have brought about great progress in laser-driven accelerator techniques. Since the idea was first mentioned by Tajima and Dawson [35] in 1979, we have become able to produce laser-driven electron beams with energies of a few GeV. Of course, we realize that this technology is still in its infancy, and there is a lot to do before real clinical applications can be started. The progress is slow and expensive and plenty of open questions remain to be answered. To appreciate these efforts, in this section I will give an outline of the history of clinical accelerators with special attention to clinical LINACs.

Before the discovery of ionizing radiation physicians had few possibilities for treating cancers. In 1895, Wilhelm Conrad Roentgen discovered a new kind of ray which he presented in 1896 in a lecture entitled “Concerning a New Kind of Ray” [78]. He described the discovery to a journalist as follows: “It seemed at first a new kind of invisible light. It was clearly something new, something unrecorded...”. Roentgen named this new ray “X-ray”.

This historical moment marked the beginning of the radiation therapy. Within just a few months after its discovery, the X-ray was used for diagnosis and one year later it was used by Emil Herman Grubbe to treat a patient with breast cancer [79]. In the same year, Antoni Henri Becquerel began to study the properties of X-rays, but accidentally

he discovered radioactivity, the natural source of ionizing radiation.

In 1898, Maria Sklodowska Curie and her husband Pierre Curie discovered radium, a natural source of radiation. In 1901, Becquerel and Curie reported the physiological effects of radium rays [80]. In the following years, the number of studies discussing the use of X-rays and radium in medicine are increased. Due to the low penetrability of this kind of radiation, skin cancers were the most frequently treated diseases. Due to the lack of knowledge, such treatments yielded poor curative results and were accompanied by considerable side effects. Recognizing this, physicians started new studies to explore the biological effects of ionizing radiation [81]. They began to understand the nature of ionizing radiation, its interaction with matter and the impact of the time and dose of radiation on cell survival. In 1920, physicians realized that fractionating the total therapeutic dose was a more efficient method to control cancers than a single treatment session, and had fewer side effects [82].

However, until 1950 radium-based interstitial irradiation was used with kilovoltage X-ray tubes that were able to produce X-rays with energies from 50 kV to 200 kV. These radiations have a low penetrability and their applicability is limited to superficial tumours. More deeply situated malignancies require higher energies.

In the meantime, in the early 1940s, the development of the Van de Graaff and betatron accelerators made megavoltage radiation therapy possible. The Van de Graaff generator was one of the first devices used for electron beam therapy. However, the electron energies were limited to a few MeV, and were hence suitable for superficial treatments only. On the other hand, betatrons were able to accelerate electrons in the energy range of 5 MeV to 30 MeV, which was useful for the direct radiation of deep lying tumours and for generating high-energy X-ray beams.

Betatrons were large, heavy and noisy devices with a limited dose rate. The magnetic field makes it difficult to extract electrons in a straight line, which made it difficult to obtain clinically useful electron beams. However, betatrons could produce electron beams with selectable energies, over a wide range with a small energy spread.

Recognizing the limitations of betatrons, scientists and engineers were looking for new possibilities. As early as in 1924, Ising proposed a method based on the use of drift tubes and time varying fields which did not exceed the electrical breakdown voltage. In these accelerators, a series of spaced metal cylinders with increasing lengths are placed in a vacuum tube. The cylinders are connected to an RF voltage source which generates an accelerating electric field between them. The increasing cylinder lengths assure that the accelerating particle bunch arrives at the end of each drift tube in phase with the accelerating RF voltage. By selecting an appropriate RF frequency and voltage, a variety of charged particles (electrons and heavy ions) could be accelerated.

The first functional RF linear accelerator (LINAC) was constructed by Widerör [83] in 1928. He replaced the high voltage pulses with radio-frequency voltage. In 1931, Sloan and Lawrence built the first LINAC with 30 drift tubes. In 1946, Luis W. Alvarez and his colleagues at the Radiation Laboratory at the University of California, Berkeley constructed a linear ion accelerator based on a somewhat different principle.

These first linear accelerators were not able to accelerate electrons because electrons reach relativistic energies very rapidly and therefore such accelerators were extremely long. Therefore, electron acceleration required more efficient designs with microwave

frequencies. However, at that time high voltage pulses could not be timed satisfactorily for such applications. Unfortunately, for the lack of a proper high power RF generator no further progress was made until WWII, when the development of radars offered the desired high-power, high-frequency microwave power equipment [84]. After the war, the development of linear accelerators gained new momentum and over the years LINACs became the dominant machinery in modern radiotherapy.

Sixty-eight years ago, in June 1952, works began for the installation of the first clinical linear accelerator in the Medical Research Council (MRC) Radiotherapeutic Research Unit at Hammersmith Hospital, London. The hospital began treating the first patient a year later, on 7 September. This LINAC produced 8 MV X-rays using a 3 m long horizontal accelerating waveguide [85]. It was developed and built by the Metropolitan-Vickers (Met-Vic or Metrovic) Company, which was purchased by the well-known General Electric Company in 1967. In 1955 and 1956 two other clinical LINACs were installed, one in the Western General Hospital, Edinburgh and the other in Mount Vernon Hospital, Northwood, Middlesex [9]. Meanwhile, researchers at Stanford University, California, USA had developed a 6 MeV clinical LINAC, and treated the first patient at Stanford Department of Radiology in January 1956. At that time seven clinical LINACs were operational in the world and the dissemination of LINACs continued. Three Met-Vic accelerators were installed in Australia (1956-1957, Brisbane, Melbourne, Adelaide) and others followed suit in New Zealand, Japan and Russia. 1962 saw the installation of the first fully isocentric 6 MeV LINAC by Varian in the UCLA Medical Center [86]. In 1968 IAEA registered 79 LINACs worldwide.

No further considerable development took place between the 1970s and the beginning of the 1990s. It was the period of slow but continuous improvements: waveguide design, the reliability and stability of different components and control systems improved, new functionalities were added. However, a major breakthrough occurred in the late 1980s and early 1990s, when the spread of computer technology accelerated. A lot of early ideas came true and became part of everyday clinical techniques. For example, the multi-leaf collimator (MLC) had been used since the 1960s but the lack of a proper control system did not allow it to spread [9]; intensity modulation has a long history too [87] but it could only be realized in this period. The use of computers brought about plenty of changes in the field of radiotherapy/accelerators technology. All this together contributed to the rapid growth in the number of clinical accelerators and the treatments performed.

In 1985, Philips introduced the SL25 LINAC, the first fully digitally controlled medical linear accelerator. Three years later, in 1988 Varian introduced the Varian Clinac 2100C, the first computer controlled accelerator in its product range. In 1994, scientists at Stanford developed a technique, known as CyberKnife, which continually tracks the position of tumours in real time. The year 2004 saw the implementation of the 4D radiotherapy. With this technique the motion of breathing can be considered during the radiation therapy.

Today, the majority of the development efforts is addressed to further improve resolution and flexibility, and enhance automatic control, robotics, imaging technologies etc. All these features serve the purpose of making the entire process safer, more precise and more tolerable by patients. Integrated imaging systems allow treatment replanning, as well as adaptive modifications of the dosimetry plan and patient positioning before radiation dose

delivery, which significantly increases the therapeutic index of the treatments.

As far as the particle accelerator technology is concerned, efforts are being made to use high-power laser beams and gaseous plasma (fully ionized gas) media to build compact electron accelerators. The original idea of acceleration using plasma was introduced by Veksler in 1956 [88]. He proposed injecting a relativistic electron beam into plasma to produce a high-amplitude plasma wave to accelerate pre-accelerated electrons or heavier ions. However, the experiments revealed new problems, mostly in relation to the stability of the generated wakefield. Despite initial failures, the idea was significant due to the fact that using plasma as an accelerating medium bypasses the electric breakdown which limits the maximum of the accelerating gradient in the case of RF acceleration.

In 1979, Tajima and Dawson [35] proposed a scheme for electron acceleration to relativistic energies by ultraintense electrostatic plasma waves (called “wakefield”) driven by ultrashort focused laser pulses during their propagation in under-dense gaseous plasma medium. They showed that this resonant wave can reach large amplitudes in which the electrons gain relativistic energies. Unfortunately, ultrashort, high-power lasers, capable of producing resonant waves in plasma were not available at that time. To overcome this issue, in the initially proposed acceleration scheme (called plasma beat-wave accelerator, PBWA) they used two, spatially overlapping, long laser pulses with different wavelengths which resonantly excited a plasma wave [35].

Later, when powerful, ultrashort lasers became available, the two laser pulses were replaced with a short (sub ps), ultraintense laser pulse. The first experimental evidence of the success of this acceleration scheme was demonstrated by Hamster et al. [89]. This laser-plasma acceleration scheme is called “laser wakefield acceleration” (LWFA) and it has attracted significant interest in recent years [31, 90, 91] due to the availability of commercial, ultracompact, solid-state terawatt laser systems [92].

In the last decades, intensive research and development has been conducted to produce laser-generated monoenergetic electron and other particle beams suitable for practical applications. Laser-driven particle beams offers a compact alternative to conventional RF-based accelerators for the production of high energy electron and heavy ion beams as well as very high energy electron beams (VHEE, electrons with energies above 50 MeV).

Moreover, laser-driven particle beams have several unique properties which make them very attractive for applications in radiobiology and radiotherapy. The use of optical mirrors instead of high-power magnets provides relative flexibility in beam delivery, and offers new possibilities in facility design, cost reduction, and in the development of new radiotherapy techniques. For example, the low divergence of the generated electron beams facilitates the formation of micro-beams, which in the MeV energy range may be beneficial in cancer therapy [41] [42]. In general, a particle beam having a short bunch duration (ps at the sample position) leads to a very high instantaneous radiation dose rate. This can be useful for the state-of-the-art FLASH technique, which requires a high instantaneous dose rate. This novel radiotherapy technique seems to increase the therapeutic ratio by reducing both the acute side effects on normal tissues and late complications [43, 44]. In fact, LWFA particle bunches are extremely short; they are in the order of a few femtoseconds (fs) immediately after acceleration, which enables radiation chemists to conduct pulse radiolysis experiments at a time scale which has not been available until now [45]. Such ultrafast pulse radiolysis (also known as femtolysis) experiments significantly

contribute to our understanding of the biological effects of radiation.

This short and inherently incomplete review of the history of clinical accelerators help us understand and correctly appreciate the current state of development of new accelerator techniques such as laser-driven particle accelerators. Since we are interested in the development of a laser-driven particle source and its early clinical application, our expectations are sometimes unreasonably high compared to the actual state of development. When viewed against the timeline of particle accelerators, the development of laser-driven particle accelerators has only just begun. A lot of issues need to be resolved before the first clinical application but the preliminary results are promising.

1.7 The dosimetry framework of ionizing radiation

The success of radiation therapy crucially depends on the accuracy of dose delivery to the target volume and on how much the dose absorbed by the surrounding healthy tissue is minimized. Technological developments in radiation therapy permit to create more complex and conformal treatment plans to irradiate with high target doses smaller volumes that have narrow margins and are located in hard to reach anatomical regions. Without proper dosimetric data and verification, the technological benefits of modern radiotherapy techniques are valueless.

Radiobiological experiments have shown [93] that a change of 7% to 10% in dose can lead to different biological responses which significantly affect tumour control probability. This has led to a consensus that in radiotherapy practice the absorbed dose delivered to the tumour volume should be within 5% of the prescribed dose. The uncertainties in dose delivery contain all possible sources of error in dose delivery such as dose errors from dose measurements, patient positioning and movements, target volume specification etc. Therefore, the dosimetric measurements must be as accurate as possible. The international dosimetry standards recommend appropriate procedures to be followed in order to assure this required high precision [94, 95, 96, 97].

Dosimetry in radiation therapy has two important tasks: to supply the necessary dosimetric data for treatment planning calculations (radiotherapy machine commissioning) and to verify the delivered dose. Both tasks require a proper calibrated dosimetry system capable of measuring absorbed doses with high precision, sensitivity and accuracy at high spatial and dose resolution.

In general, measuring the absorbed dose is not an easy tasks. In principle the absorbed dose in point P of a homogeneously irradiated volume can be calculated with the following simple relation:

$$D = \Phi \cdot S, \quad (1.2)$$

where Φ is the particle energy fluence in point P and S is a quantity which characterizes the absorption process (mass attenuation coefficient in case of photon radiation or stopping power in case of charged particle). This means that knowing parameter S and measuring the particle fluence in point P, the absorbed dose in point P can – in principle – be determined.

However, in practice neither the particle fluence, nor the exact value of S in point P is known. Particle energy fluence is perturbed by the scattering effects of the absorber

and depends on the exact irradiation conditions. Parameter S depends on the particle energy, on the effective atomic number and on the physical state of the absorber material. Both the energy spectra and the angular distribution of particles are affected during propagation in the absorber, and precise calculation is possible only in a few simple cases.

Moreover, if we try to measure the absorbed dose due to a homogenous irradiation field, the detector used for measurements introduces a certain degree of perturbation. This means that the measured dose differs from the dose actually absorbed. This intrinsic nature of dose measurements cannot be neglected and various models have been developed. All these models are an improved version of the Bragg-Gray cavity theory which relates the absorbed dose in a cavity volume of material A to the absorbed dose in the same point and volume of the surrounding medium of material B in the absence of the cavity volume.

The Bragg-Gray cavity theory is based on the assumption that fluence Φ of identically charged particles having a kinetic energy of E_k , and which pass through an interface between two different media, A and B, is continuous across the interface. But this is valid only with a certain degree of approximation [98]. The original Bragg-Gray theory formulates the following assumptions: the absorbed dose in the cavity is imparted entirely by the charged particles crossing it, and the cavity does not perturb the charged particle field. The latter assumption is true if the dimensions of the cavity are small in comparison to the particle range. When these two conditions are met, the absorbed dose in the cavity can be calculated with the following relation:

$$D_B = D_A \frac{\left(\frac{dE_k}{\rho dx}\right)_{c,B}}{\left(\frac{dE_k}{\rho dx}\right)_{c,A}}, \quad (1.3)$$

where D_B is the dose absorbed in the volume of cavity containing the material B, D_A is the dose absorbed in the same volume containing the surrounding material A and in the absence of the cavity [99, 100].

Of course, the conditions of the Bragg-Gray theory are difficult to fulfil in practice. To this end, a series of modifications and additional conditions was introduced to extend the validity of the cavity theory. These extensions lead to the Spenser cavity theory [101] or to the Burlin cavity theory [102], to name only a few.

Therefore, measuring the absolute value of the absorbed dose for a clinical beam would be a sophisticated procedure, necessitating expensive instrumentation and very careful analysis and control of the measurement conditions.

In practice, professionals follow a dosimetry protocol, published by national and international organizations such AAPM (American Association of Physicists in Medicine, USA), IPEM (Institute of Physics and Engineering in Medicine, UK) or IAEA (International Atomic Energy Agency). These procedures are based on the use of a reference dosimeter (usually an ionization chamber) which has a calibration factor, traceable to a Primary Standard Dosimetry Laboratory (PSDL) and ensures consistency in dose determination.

In this thesis I follow the recommendation of the dosimetry protocol established by the IAEA through Technical Report No. 398 (TRS 398) [95]. This code of practice is based

on the absorbed dose to water calibration using an absolute dosimetric method. There are three methods currently known as sufficiently accurate for measurements of absorbed dose to water: calorimetry, chemical dosimetry and ionization dosimetry [103]. The most commonly used instrument is the ionization chamber due to its good reproducibility and stability. For primary standard the ionization chamber consists of a graphite cavity chamber designed to fulfil the requirements of the Bragg-Gray cavity theory. The ionization chamber is placed in a water phantom at a reference depth [104].

Another method for accurate measurements of absorbed dose to water is the Fricke type chemical dosimeter. This method uses the response of the Fricke solution using the total absorption of an electron beam in the solution [105]. Two other methods are the water calorimeter [106, 107] and the water calorimeter with Fricke transfer dosimeter [108]. Several works have been conducted to compare these methods and they have been found to show good agreement within the relatively standard uncertainties estimated by each primary standard dosimetry laboratory [103, 109, 110, 111].

In concordance with this formalism, the absorbed dose to water at the reference depth in water for a reference beam quality Q_0 and in the absence of the chamber can be obtained by:

$$D_{w,Q_0} = M_{Q_0} N_{D,w,Q_0}, \quad (1.4)$$

where M_{Q_0} is the reading of the dosimeter under the reference conditions (in case of ionization chambers the produced charge in units of pC) and N_{D,w,Q_0} is the calibration factor in terms of absorbed dose to water obtained from a standard laboratory. It is important to note that in most clinical situations, the measurement conditions differ from the reference conditions used in a standard laboratory, which may affect the response of the dosimeter. The measured dose can be influenced by a series of quantities that may arise from the dosimeter itself or may be related to the radiation field or irradiation conditions. All these influencing factors have to be considered by applying an appropriate correction factor to Equation 1.4, and the absorbed dose to water for the measured beam quality Q :

$$D_{w,Q} = M_Q N_{D,w,Q_0} \sum_i k_i, \quad (1.5)$$

where M_Q is the dosimeter reading for beam quality Q and k_i is the correction factors.

Once the radiation field is calibrated and a detailed dosimetric characterization is made, the dosimetric planning of patient irradiation can be performed.

The main aim of treatment planning is to maximize the dose delivered to the cancer cells while keeping the dose to the neighbouring tissues and organs at risk as low as possible. Difficulties in determining the target volume, in designing the proper radiation field by the complex superposition of individual radiation fields, in calculating the absorbed dose in inhomogeneous tissue, as well as the difficulties in correct and secure patient positioning, all contribute to the uncertainty of dose delivery.

The laser-driven radiation beam has some features which differ from the LINAC based beams. For example, at an electron beam accelerated by LINAC the bunch duration is in the order of micro-seconds, while for laser-driven electron beams it is in the order of pico-seconds. Consequently, the instantaneous dose rate for LINAC is around 10^7 , while for laser-driven beams it is 10^{12} to 10^{13} Gy/s. Furthermore, with laser-driven electron beams

the kinetic energy of the electrons can reach up to 100 MeV or even a few GeV, while the maximum kinetic energy produced with a conventional LINAC is around 24 MeV.

At such a high dose rate and beam energy the collection efficiency of the ionization chamber is reduced, consequently saturation correction cannot be determined with the classical approach [112]. There are several attempts to overcome this problem and with an appropriate correction of ion recombination it is possible to perform absolute dosimetry measurements even in the case of high dose rate clinical accelerators such as intraoperative radiotherapy (IORT). However, laser-driven accelerators produce beams with much higher dose rates than clinical accelerators, and more detailed studies are required to use ionization chambers for measuring the absorbed dose with a laser-driven particle beam. Yet, an ionization chamber can be used for relative dosimetry to control the delivered dose [113, 69]. In this case, the ionization chamber is usually accompanied by a Faraday cup detector which measures the current generated by the charged particle beams that run through the cup. This current can be used to determine the particle fluence [114, 115, 116, 117].

Recent studies have shown that thermoluminescence dosimeters (TLD), optically stimulated luminescence dosimeters (OSL) and radiochromic films (Gafchromic EBT) have no dependence up to $4 \cdot 10^9$ Gy/s within 2% and they are thought to be suitable for laser accelerated beams [118].

Today radiochromic films are preferred due to their easy-to-use and favourable dosimetric properties. Radiochromic films are extensively used in medical applications [119, 120, 121]. They are based on a class of polymers (polydiacetylene, PDA) which become opaque as a result of ionizing radiations. Current studies show that radiochromic films are insensitive to dose rate [122, 123] and exhibit low dependence on the beam energy [124, 125, 126]. Therefore, radiochromic films are suitable for dosimetry measurements of laser-driven particle sources. However, in order to account for possible differences, calibration with a clinical accelerator is always recommended.

To date, no dosimetric protocols have been established for the absolute dosimetry of radiation beams with such high instantaneous dose rates due to the lack of knowledge related to the response of dosimeters to such high dose rate radiation. My effort was to prepare the necessary methodology for future dosimetric measurements in such radiation fields using a modified version of the Fricke type chemical dosimeter, as an alternative to ionization chambers. The results of this work are presented in the second part of this thesis.

1.8 Aims of the thesis

In this study we investigate the dosimetric properties of an 1 kHz repetition rate LWFA electron beams. High repetition rate electron beams can be generated by commercially available 1 kHz laser systems (multi-TW power & few-cycle pulse duration); one such system is currently operational at ELI-ALPS Research Institute [92]. Such a high repetition electron beam was recently reported by Guénot et al. [127], Ouillé et al. [128]. Using the PIC and Monte Carlo simulation techniques the following statements were examined:

1. The energy spectra of an 1 kHz repetition rate LWFA electron beams generated with a 1 kHz laser system with parameters of the laser system currently operational at ELI-ALPS Research Institute are suitable for radiotherapy applications.
2. With the achievable radiation dose and dose rate and depth dose characteristics such particular LWFA systems could be used to address different practical needs (irradiate large target volumes, intensity or energy modulations etc.).
3. The high repetition rate compensate for the shot-to-shot reproducibility issue.

Furthermore, an enhanced chemical dosimetry system was developed to be used in various irradiation arrangements where common dosimetry tools are not suitable (for example in case of LWFA electron beams) or are difficult to use (like in radiobiological experiments where the standard reference conditions cannot be provided in most cases). The main aim of this work was to develop such a dosimetry tool, capable of measuring the absorbed dose with high precision and accuracy in reference conditions. To achieve this aim, the following statements were examined:

1. With appropriate modification of the composition the FBX chemical dosimeter can be further optimized considering its dosimetric properties and capabilities as well as accuracy and precision.
2. With full characterization of the technique and developing the necessary tools and accessories for radiation dose measurements in reference conditions, as well as establishing the dosimetry methodology necessary to assure the desired accuracy and precision, the optimized FBX chemical dosimeter can be used as an absolute dosimetry technique suitable for measurements of radiation dose in the clinical dose domain (up to 20 Gy).

Chapter 2

Feasibility of laser-driven electron beams

2.1 Introduction

Electron beam therapy is a widely used radiotherapy technique for the irradiation of superficial target volumes. The characteristics of depth dose distribution make the electron beams suitable in a variety of clinical situations. Nowadays, electron beams are used in the treatment of skin, breast and chest wall cancers; peripheral lymphatic regions of head and neck cancers; and for the irradiation of other neoplastic diseases. Electron beams can also be used in intra-operative applications for selective dose delivery to the tumour bed after the surgical removal of pancreatic, colorectal cancers and soft tissue sarcomas [129].

Similarly to lightweight charged particles, electrons lose their energy continuously as they propagate in matter and undergo significant scatter. Therefore, beam characteristics are extremely sensitive to surface irregularities and volume inhomogeneities. Moreover, scatter from the structural elements of the accelerator head has a considerable effect on dose distribution, which leads to unique depth dose characteristics for each machine.

In general, the central depth dose has a uniform plateau of dose around the depth of dose maximum, varying from 90% to 100% of the maximum central-axis dose. The depth dose drops steeply both laterally and distally which permits the irradiation of superficially situated targets (up to approximately 6 cm of the patient's surface) with some dose absorbed by the underlying normal tissues. This property offers protection for the anatomical structures beyond the target volumes.

The depth of dose maximum is a function of electron beam energy. Therefore, the necessary beam energy is determined by the depth of target volume. As a rule of thumb, the electron energy should be at least 3.0–3.3 times the maximum depth of the target volume, in cm, situated in water. In this case the target volume is covered with 80%–90% relative doses [129]. However, dose distribution is affected by several physical characteristics. The isodose curve is narrowed as the depth increases to the depth of 90% of the dose maximum [130]. Furthermore, there is considerable dose perturbation due to tissue inhomogeneity, which leads to dose inhomogeneity in the target volume [131]. Oblique incidence also has

an effect on dose distribution as well as on the source to surface distance (SSD) or field size and shape [8].

Concurrently, the build-up region is short with a high entrance dose. Within a few cm of tissue, the dose rises up to 90 % of the dose maximum. The relative surface dose is the lowest for low-energy electron beams ($\approx 70\%$ at 6 MeV) and increases with the beam energy ($\approx 95\%$ at 20 MeV) [129, 8].

These physical characteristics of the electron beam make it a unique therapeutic modality. However, the currently available clinical electron beams have their limitations. The relatively low penetration is a decisive factor when we deal with deeply situated target volumes. In this case, high energy photon therapy is used for deeper localized tumors applying volumetric imaging based 3D planned irradiation techniques with growing selectivity (3DCRT, IMRT, volumetric arch therapy etc.) [132]. The penumbra region of the depth dose profile becomes larger with penetration depth, which makes it difficult to protect the healthy tissues around the targeted tumour. This lateral spread is more acute at low energies and in heterogeneous tissues, such as the tissue of the chest.

Accelerators currently used in clinical practices generate electron beams with energies between 6 and 24 MeV. At beam energies greater than approximately 20 MeV, the depth-dose curves lose their sharp fall-off and begin to take on the characteristics of photon beams. Due to the bremsstrahlung energy loss, the fall-off region becomes flatter and the penumbra region broadens due to the increased multiple Coulomb scattering.

If the electron energy exceeds 150 MeV, the penetration depth becomes larger than 40 cm and scattering in air is sufficiently low to make pencil beam scanning possible. This suggests the scientific community should conduct theoretical studies of the potential application of very high energy electrons in radiotherapy.

However, such VHEE beams are only available at a few academic laboratories. For example, the Next Linear Collider Test Accelerator (NLCTA) located at the SLAC National Accelerator Laboratory is capable of producing high-brightness electron beams, with energy between 60 and 150 MeV, which supports the development of the VHEE therapy [133]. There are only few more such experimental facilities where VHEE beams can be produced for experimental studies. In order to make VHEE beams widely available, LWFA offers a potential alternative to conventional RF-based accelerators for the production of electron beams.

As far as the particle accelerator technology is concerned, there is a trend in using high-power laser beams and gaseous plasma (fully ionized gas) media to build compact electron accelerators. In 1979, Tajima and Dawson [35] proposed a scheme for electron acceleration to relativistic energies by ultraintense electrostatic plasma waves (called “laser wakefield”) driven by ultrashort focused laser pulses during their propagation in underdense gaseous plasma medium. This laser-plasma acceleration scheme is called “laser wakefield acceleration” (LWFA) and it has attracted significant interest in recent years [31, 90, 91] due to the availability of commercial, ultracompact, solid-state terawatt laser systems [92].

Generally, the use of optical mirrors instead of high-power magnets provides relative flexibility in beam delivery, and offers new possibilities in facility design, cost reduction, and in the development of new radiotherapy techniques. These advantages are not self-evident in experimental laser facilities which require sophisticated and delicate infras-

structure. However, the inherent strengths of such systems, and the rapid technological progress make laser-plasma acceleration in general and LWFA in particular a promising alternative to conventional RF-based accelerators.

Furthermore, LWFA electron beams have several unique properties which make them attractive for applications in radiobiology and radiotherapy. For example, the low divergence of the generated electron beams facilitates the formation of microbeams, which in the MeV energy range may be beneficial in cancer therapy [41] [42]. In general, an electron beam having a short bunch duration (ps at the sample position) leads to a very high instantaneous radiation dose rate. This can be useful for the state-of-the-art FLASH technique, which requires a high instantaneous dose rate. This novel radiotherapy technique seems to increase the therapeutic ratio by reducing both the acute side effects on normal tissues and late complications [43, 44]. However, recent experiments show that several factors such as instantaneous and mean dose rate, total dose and the pulsatile nature of the beam may influence the FLASH effect. So far, no clear consensus has been reached in this issue. A valuable review on this subject has been recently published by Wilson et al. [134].

In fact, LWFA electron bunches are extremely short; they are in the order of a few femtoseconds (fs) immediately after acceleration [135], which enables radiation chemists to conduct pulse radiolysis experiments at a time scale which has not been available until now [45]. Such ultrafast pulse radiolysis (also known as femtolysis) experiments significantly contribute to our understanding of the biological effects of radiation.

However, active research in LWFA has revealed some efficiency, stability and reliability issues that need to be resolved prior to its implementation. Efficiency in terms of pulse charge and repetition rate ensures the necessary dose rate, which must be at least 4 Gy/min for real radiotherapy applications. The moderate stability of LWFA accelerators in terms of energy and pulse charge is the primary task which requires immediate attention before such accelerators are introduced into real radiobiological or medical applications. Furthermore, the reliability and effectiveness of beam shaping must be enhanced. Fortunately, there is significant progress towards stable LWFA electron beams [65, 66].

In this study we investigate high repetition rate LWFA electron beams recently reported by Guénot et al. [127] and Ouillé et al. [128]. We analyze the potential of those beams for radiobiology and radiotherapy purposes. High repetition rate electron beams can be generated by commercially available 1 kHz laser systems (multi-TW power & few-cycle pulse duration); one such system is currently operational at ELI-ALPS Research Institute [92]. Using Monte Carlo simulations we demonstrate that this type of 1 kHz LWFA is capable of generating a sufficient dose rate for practical radiobiological or medical applications. The critical issues such as low radiation dose per electron bunch and the relatively low stability of such systems can, in principle, be compensated for if the LWFA operates at 1 kHz. Additionally, we outline some practical issues and pitfalls which need to be addressed before such systems are used in real applications.

2.2 The SYLOS laser system

This work has been inspired by one of the several laser-driven particle sources which will be available in the near future at ELI-ALPS [1]. This particle source will be powered by SYLOS, 1 kHz repetition-rate “single-cycle” laser, one of the main laser systems of the research facility.

The SYLOS system was developed by a consortium of EKSPLA, Light Conversion, Vilnius University and Northrop-Grumman in compliance with the requirements of ELI-ALPS. The SYLOS system has an Optical Parametric Chirped Pulse Amplification (OPCPA) architecture and generates > 4.5 TW peak power, few-cycle laser pulses (actually 2.2 cycles pulse duration) at a high repetition rate (1 kHz), with a central wavelength of 880 nm [92]. During the Factory Acceptance Test, the laser demonstrated 53.8 mJ pulse energy with 8.8 fs pulse duration at 1 kHz repetition rate combined with a remarkable long-term stability (250 mrad CEP and 1.5 % energy stability) [136]. The laser is currently being upgraded and is expected to be installed at ELI-ALPS with parameters of 35 mJ and < 7 fs, ultimately capable of 100 mJ and 5 fs.

The OPCPA architecture of the laser allows sub-10 fs laser pulses at much larger pulse energies than more common 1 kHz systems, i.e. Ti:Sa lasers combined with hollow-core-fibre post-compression (e.g. [137]), and also offers a higher repetition-rate than 10 Hz OPCPA systems like the Light Wave Synthesizer 20 [137].

While SYLOS is optimized for different purposes, the laser pulse energy is sufficient to accelerate electrons to VHEE-relevant energy levels, while the high repetition-rate (and thus the high average laser power) would allow for higher dose rates, and also reduce effects of shot-to-shot fluctuations.

At ELI-ALPS, the SYLOS-driven electron beamline is expected to provide electrons with 30-50 MeV mean electron energies and above, with bunch charges of a few tens of pC at 1 kHz repetition rate, corresponding to conversion efficiencies of a few percent and electron currents of tens of nA. The energy spread of these electron bunches is relatively large, 10-100% of the mean electron energy, and strongly depends on the laser beam parameters which will be investigated at a later stage.

2.3 Methods

To assess the dosimetric characteristics, Monte Carlo simulations were performed based on the Geant4 (version 10.3) Monte Carlo simulation framework [138, 139, 139] on a workstation with an Intel Xeon 16-core processor.

Geant4 is a very flexible development environment which offers great flexibility in all details of simulation scenario setup using object-oriented programming style and C++ programming language. It has an abundant set of physics models to handle the interactions of particles with matter across a very wide energy range and it offers the direct possibility to control all details of simulation and collect the desired information. There are a lot of predefined sets of tools which make the development of the simulation code relatively quick and easy and an important feature of Geant4 is that it offers tools for multi-threading and parallel programming [140]. Geant4 is also an open source and free

development toolkit, offered under *Geant4 Software License*, and maintained by CERN, with contributors from a variety of domains including medical and radiobiological applications.

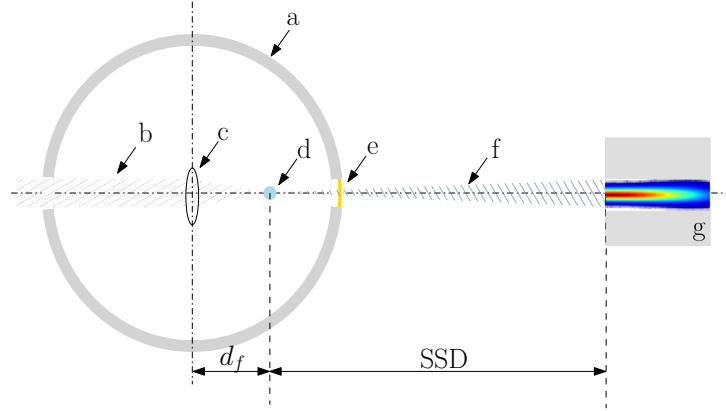


Figure 2.1: The semi-realistic model of irradiation geometry used in the MC simulations. The laser beam (b) enters the vacuum chamber (a) and is focused using optics (c) onto a gas jet target (d) where LWFA acceleration takes place. The accelerated electrons (f) exit the vacuum chamber through a Mylar window (e). The absorbed dose was calculated in the water phantom (g) placed at different source-to-surface distances (SSD).

Figure 2.1 shows the semi-realistic geometry used in the simulation scenarios. Electron acceleration takes place in the vacuum chamber (a) at the gas-jet target (d). The accelerated electron beam exits the vacuum chamber through a $300\ \mu\text{m}$ thick circular Mylar window (e). The absorbed dose is calculated in a water phantom (g), a box with 6 mm thick Plexiglas walls filled with liquid water and placed in front of the Mylar window at different source to surface distances (SSD). The materials for all geometric components of the simulation were set using the materials defined in the NIST materials database [141].

The electron beam source was simulated based on the electron beam characteristics obtained from 3D particle-in-cell (PIC) simulations, which were performed using the EPOCH open source code ([142]) with the parameters of the SYLOS II laser system available at ELI-ALPS.

The position, energy and direction of each electron in the beam were extracted from a data file generated by the 3D PIC simulation and were used to set up the initial electron parameters in the MC simulation.

The position, energy and direction of each electron in the beam were derived from a data file generated by the 3D PIC simulation, taking into account the correct weighting factor, as well as the position and momentum of each pseudo-electron. These parameters were then used to set up the initial electron parameters in the MC simulations.

The PIC simulations used the following laser parameters: pulse duration 8 fs (FWHM), peak power 4 TW (corresponding to 30 mJ total energy per pulse) and 1 kHz repetition rate. The laser beam was focused to a $2.2\ \mu\text{m}$ focal spot diameter (FWHM), resulting in $2 \cdot 10^{19}\ \text{W}/\text{cm}^2$ peak intensity. The Rayleigh length of such a tightly focused laser pulse is around $100\ \mu\text{m}$, wherefore we use a very narrow He (helium) gas jet as a target, where

the maximum electron density after ionization is $n_0 = 4 \cdot 10^{19} \text{ cm}^{-3}$. The spatial density profile is described by a super Gaussian function:

$$n_e = n_0 e^{-\frac{(z-z_0)^4}{2\sigma^4}}, \quad (2.1)$$

where $z_0 = 70 \mu\text{m}$ and $\sigma = 38 \mu\text{m}$. In the radial direction the plasma density is assumed to be uniform. The laser pulse is focused at $z = 50 \mu\text{m}$, $20 \mu\text{m}$ before the centre of the gas jet. Due to tight focusing, the laser intensity increases quickly along the propagation axis, which results in electron self-injection into the wakefield. The injected electrons are accelerated over a distance of $50 \mu\text{m}$ reaching an average energy above 30 MeV with a small energy-spread, as shown below.

The simulation grid was 35 nm in the z direction and 50 nm in the lateral directions, which means that each macroparticle (pseudo-electron) contains 875 real electrons. The plasma electrons are represented by 4 particles per cell. For the field solver we use a special method presented by Lehe et al. [143], in order to compensate for the grid dispersion, which can generate errors in laser propagation.

The depth dose was scored in several ways. The first approach was a 3D ROOT histogram, with numbers of bins in all directions chosen in a way to form a 1 mm^3 voxel size. Another, more realistic approach was simulating a water equivalent detector, with the same dimensions as the sensitive volume of a Marcus ionization chamber [144] and using a simulated sheet of radiochromic film, both placed in the water phantom. The radiochromic film was simulated as Gafchromic EBT2 film with $5 \times 5 \text{ cm}$ dimensions with the same structure and composition as published by the manufacturer. The absorbed dose was scored in an active layer of simulated Gafchromic films with a 2D histogram. The bin number of the histogram was selected in a way that the 2D histogram would have the same 75 dpi resolution as the resolution of the film scans used in film dosimetry.

The physics of the simulations were set up using the physics-list mechanism of the Geant4 toolkit and the QGSP_BIC_HP_EMZ physics models, recommended for medical uses [145]. This physics-list includes the hadronic models from which the photo-nuclear and electro-nuclear interactions are useful for these purposes. The EMZ option contains the electromagnetic physics models, including the photoelectric effect, Compton and Rayleigh scattering for gamma particles and for charged particles ionization and Bremsstrahlung. The range cut was set to $30 \mu\text{m}$, which is converted at initialization time into the energy threshold for secondary gamma, electron, positron and proton production.

For statistically meaningful results, 10^7 primary electrons were generated in all simulations. The simulation code, including the geometry, physics and the scoring mechanism was validated using data published in [146] and [147].

2.4 Results and discussion

As stated in the Introduction, our main aim is to assess the possibility of using a 1 kHz laser driven electron beam for radiotherapy and radiobiology applications. Recently Guénot et al. [127] reported high-quality 6 MeV relativistic electron beams having an energy spread of 3 MeV and a charge of ~ 0.5 pC with 30 % fluctuation using 1 kHz repetition rate, single-cycle 2.1 mJ laser pulses with 3.4 fs pulse duration in nitrogen gas jet.

However, reliable radiotherapy applications require 6 MeV or greater electron energies. Based on our PIC simulation, such beams can be produced with the parameters of the SYLOS II laser system available at ELI-ALPS.

Figure 2.2a shows the energy spectra of the accelerated electrons right after the acceleration (solid line) and at the phantom surface (dashed line). The slight difference between the two spectra is the results of electron scattering during propagation from the plasma point to the phantom surface. Because the electrons are light particles, they undergo considerable scatter during propagation. During this, their energy and propagation direction change and some electrons leave the beams resulting in energy spectra with less intensity and shifted toward lower energies and with broadened energy peaks. This effect is more evident at low than at high energies. Therefore, at high relativistic energies this scattering effect is negligible, which is also confirmed by the mean kinetic energies: the initial mean energy of the beam is 35.97 MeV, while at the phantom surface the mean energy is 35.73 MeV.

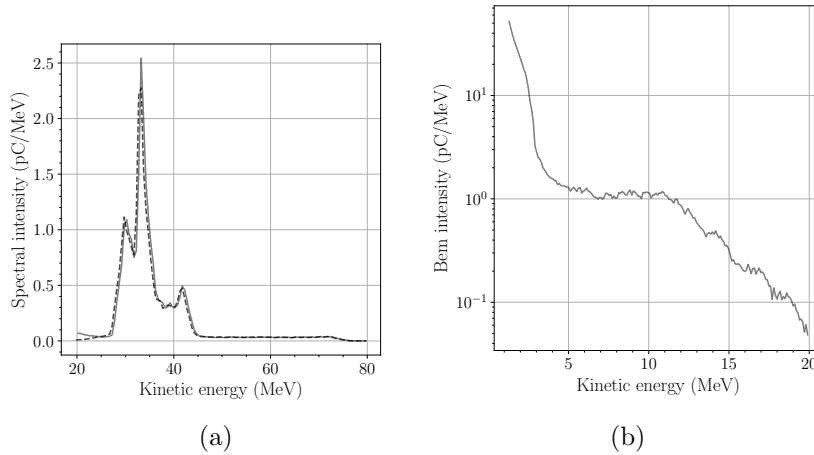


Figure 2.2: (a) The energy spectra of the simulated electron beam at the acceleration site (solid line) and at the phantom surface situated at an SSD of 100 cm. The long high-energy tail of the energy spectrum is a specific feature of the self-injection mechanism. (b) The energy spectra of electrons with low energy (up to 20 MeV). They are excluded from simulations due to their large divergence.

Based on the simulated spectra, the average kinetic energy of the accelerated electrons equals 35.7 MeV with FWHM of around 6 MeV. The spectra presented in Fig. 2.2a contain electrons with kinetic energies above 20 MeV, however, there is a non-negligible, low-

energy background (Fig. 2.2b). These low energy electrons are usually generated with a large divergence angle, therefore they do not contribute to the absorbed dose and were omitted from the simulations. On the other hand, such electrons produce considerable Bremsstrahlung radiation when dumped, which must be considered in terms of radiation protection.

The long high-energy tail of the energy spectrum is a specific feature of the self-injection mechanism in LWFA. Here, electrons are accelerated during the initial phase of the injection, when all electrons are located at the peak electric field of the ion cavity. This process is very sensitive to the laser and plasma parameters. Consequently, the amount of electrons is so low in this energy domain that they are ignored in experiments.

The multi-peak nature of the energy spectra is believed to be a natural outcome of the LWFA acceleration process in high-density plasma due to the extremely high-field gradient of the plasma wave. In other words, since the electron bunch size in 3D is around $1 \mu\text{m}^3$, it means that some electrons get slightly out of the extremely narrow acceleration phase during the propagation in the wake behind the laser pulse, which results in minor peaks around the main high-energy peak. It is also a result of the slightly different velocity of the accelerated electrons in comparison to the wakefield phase velocity. This phenomenon, which is known as the “dephasing effect”, can be mitigated by a careful control of plasma density or by some plasma density profiling [148, 149, 150].

Such a multi-peak spectrum may produce some inhomogeneity in the depth dose distribution, however this effect can be neglected as long as the energy peaks are close to one another. This means that the spectrum can be approximated with a single, broadened energy peak. This wide energy peak produces a depth dose distribution with a broader and flatter plateau around the depth of dose maximum than a narrower energy peak, which can be useful when large volumes of interest need to be irradiated homogeneously.

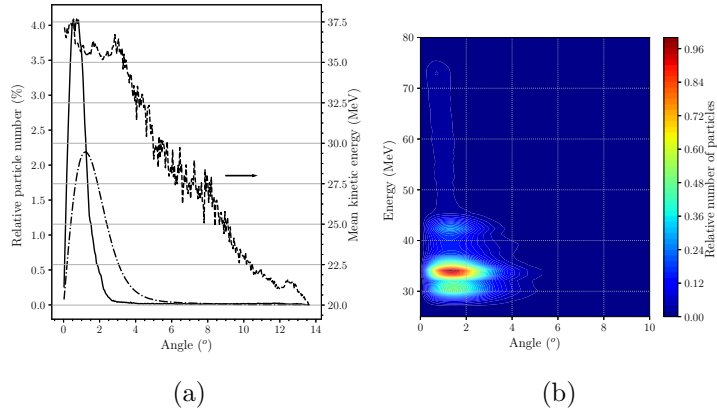


Figure 2.3: (a) The electron beam divergence (defined as the angle between the electrons’ direction and z axis): the solid line represents the initial angular distribution while the dashed line represents the angular mean energy distribution. The dash-dotted line represents the angular distribution at the phantom surface. (b) The angular distribution – energy map of the accelerated electrons.

However, as can be seen in Fig. 2.3a, the change in the initial angular distribution of accelerated electrons, defined in terms of the angle between the electron propagation direction and the z axis, is evident. As illustrated in Fig. 2.3a, the angular distribution at the phantom surface (dash-dotted line) is wider than the initial angular distribution (solid line). The former has a mean value of 1.83° , while at the source position this is 1.13° . This broadening affects the depth dose distribution, resulting in a smaller depth of dose maximum and a larger dose profile.

From the angular distribution of energy fluence presented in Fig. 2.2a (dashed line) we can conclude that electrons with kinetic energies around the mean kinetic energy propagate in the forward direction. The low energy component of the beam (Fig. 2.3a) is predominantly accelerated away from the propagation direction and have no direct contribution to the depth dose distribution. However, because the initial angular distribution has a direct effect upon the dose distribution, the shot-to-shot reproducibility of angular distribution is mandatory.

It is important to note that this result refers to unconditioned electron beams. The concrete energy and angular distribution can be significantly altered by the scattering conditions. Scatter from collimators and other structures in the experimental setup has a significant effect on these characteristics, and influence dose distribution at least to the depth of dose maximum.

The 35.7 MeV mean electron energy combined with the quasi-monoenergetic nature of the spectrum makes this electron beam suitable for radiotherapy applications.

It is agreed that at least 4 Gy/min dose rate is necessary for successful practical applications. As a first step towards determining the capability of the electron beam in question, the total dose rate at the target surface can be estimated by integrating the following formula (Equation 2.2) over the whole energy spectrum of the incident electron beam:

$$\dot{D}(E) = 1.602 \cdot 10^{-10} \Psi(E) \cdot \left(\frac{dE}{\rho dx} \right)_{T,w}, \quad (2.2)$$

where $\Psi(E)$ is the energy fluence at the target surface, $(dE/\rho dx)_{T,w}$ is the total mass stopping power in water and $1.602 \cdot 10^{-10}$ represents the unit conversion factor between MeV/g and Gy. Using the beam spectra (Fig. 2.2a) and the NIST data of total mass stopping power[141], the total dose rate at a distance of 100 cm is 2.901 Gy/pC/s. Since in practice we expect a higher pulse charge than 1 pC, this value is sufficient for real applications.

However, Eq. 2.2 gives us a rough estimate of the absorbed dose in a water phantom. For a more accurate estimate, we must consider the radiation yield produced by Bremsstrahlung, and the variation of beam spectra with depth and the build-up effect, which jointly determine the particular form of the electron depth dose curve. Therefore, we performed Monte Carlo simulations using the electron beam parameters (electron position, direction and kinetic energy) obtained with the PIC simulations.

The dose rate for different SSD was calculated at the depth of dose maximum. The obtained results are summarized in Table 2.1. Because the standard SSD used in radiotherapy is 100 cm, in the following we will refer to this SSD value. For this distance, the depth of dose maximum is 1.9 cm and the amount of dose delivered by a single electron bunch with 1 pC charge is $97.1 \mu\text{Gy}$. From the 3D PIC simulations we can conclude that

Laser beam pulse length (FWHM)	8 fs
Peak power	4 TW
Repetition rate	1 kHz
Focal spot diameter (FWHM)	2.2 μm
Peak intensity	$2 \cdot 10^{19} \text{ Wcm}^{-2}$
Target	He gas jet
Max. e- density	$4 \cdot 10^{19} \text{ cm}^{-3}$
Expected e- pulse charge	3–10 pC
Mean kinetic energy	35.97 MeV
Angular distribution (FWHM)	1.13 $^{\circ}$
Expected dose rate for 100 cm SSD	6 Gy/min/pC
Instantaneous dose rate	$3.9 \cdot 10^6 \text{ Gy/s/pC}$
Depth of dose maximum in water	1.9 cm

Table 2.1: Key parameters and results of the simulations.

the electron bunch charge is 3 pC and the amount of dose delivered by a single electron bunch totals $\sim 0.3 \text{ mGy}$. This very small amount of dose can be enhanced dramatically by operating the LWFA at 1 kHz repetition rate, which results in a mean dose rate of 0.3 Gy/s or 18 Gy/min which is comparable with the achievements of medical LINACs.

However, through the adjustment of laser and gas target parameters, the electron bunch charge can be increased, and is expected to reach charges exceeding 10 pC. This means that the above calculated dose rate can be increased by a factor of ten. With this high dose rate the LWFA acceleration technique becomes the rival of today's LINAC systems.

On the other hand, it is well known that the LWFA electron acceleration process is particularly sensitive to laser system stability in terms of energy, focus point position and other optical parameters, as well as plasma generation from gas jets. The major uncertainty comes from fluctuation in the beam pulse charge. For example, Guénot et al. [127] reported a 30% shot-to-shot fluctuation in charge. This fluctuation has a direct effect on the achievable absorbed dose and represents the key condition for radiotherapy applications. It is known that a 7% uncertainty in absorbed dose can modify biological outcomes. For this reason, in radiotherapy practice the maximum permissible cumulative uncertainty in dose delivery is 5%, including uncertainties in treatment planning, patient positioning, dose measurements etc.

In the following we prove that operating the LWFA at 1 kHz repetition rate provides precise control over dose delivery. Assuming a normal distribution of pulse to pulse charge fluctuation with a FWHW of 30% as reported by Guénot et al. [127], the total

dose delivered by n shots of 1 pC can be written as:

$$D = \sum_{i=1}^n D_{1pC} q_i, \quad (2.3)$$

where D_{1pC} is the dose delivered by a single shot with 1 pC charge and q_i is the charge of each shot. The shot-to-shot charge fluctuation follows a normal distribution, which can be described with the probability distribution:

$$p(q_i) = \frac{q_{mean}}{\sigma \cdot \sqrt{2 \cdot \pi}} \cdot e^{-\frac{(q_i - 1)^2}{2 \cdot \sigma^2}}. \quad (2.4)$$

With a constant pulse charge of 1 pC and with a standard deviation of $\sigma = 30\%$, for a dose of 1 Gy, we need approximately $n = 10^4$ shots. Sampling n number of shots with a normal distribution of charge and applying Eq. 2.4, n shots deliver 1 Gy with an uncertainty of 0.30%.

This means that our results fit with this condition very well. Moreover, higher laser beam instability is also acceptable (not the case of SYLOS II laser system at ELI-ALPS, which is an ultra-stable system), on the basis of which we can confidently state that 1 kHz LWFA-based electron beams are suitable for radiobiological and/or radiotherapy applications.

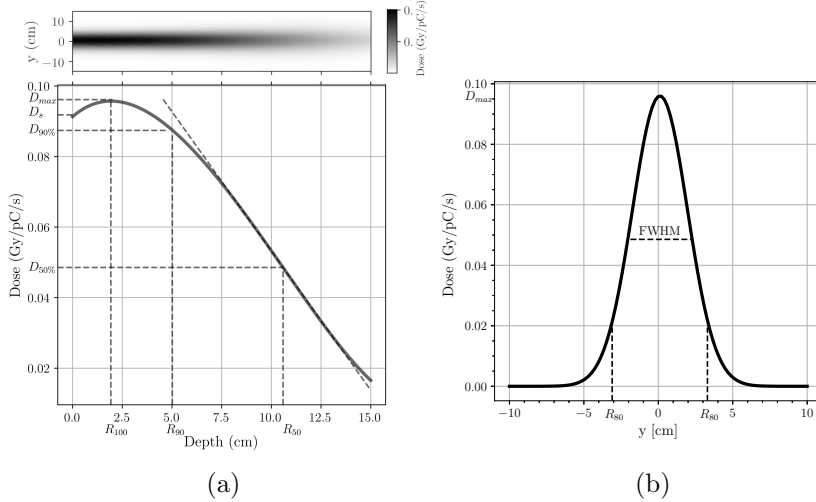


Figure 2.4: The absorbed dose characteristics of the unconditioned electron beam; 2.4a the dose distribution map and depth dose curve with its key characteristics: the dose maximum $D_{max} = 9.7$ cGy/pC/s at a depth of 1.93 cm; the therapeutic range $R_{90} = 5$ cm defined as the depth where the absorbed dose equals 90% of D_{max} . 2.4b the depth dose profile at the depth of the dose maximum with the full width at half maximum $FWHM = 4$ cm.

Fig. 2.4a presents the absorbed dose map and the corresponding central depth dose curve, which has a shape typical of electron beams. The entrance dose or surface dose

(D_s) is stated at 0.5 mm depth and is 0.091 Gy/pC/s, which represents 94 % of D_{max} (which is generally is between 90 % and 100 % for electron energies above 10 MeV). The rise of the curve is due to the increasing mean incident angles as a result of electron scattering, which leads to an increase in electron fluence with depth. Because the absorbed dose is proportional to electron fluence, the absorbed dose in successive depths increases until the mean scattering angle no longer increases. When this condition is fulfilled, the outgoing electrons from an elementary volume are compensated with the electrons leaving that volume (i.e. electronic equilibrium is assured) and the depth dose curve becomes relatively flat until electrons leave the beam. From this point the curve begins to fall at a rate depending on the initial beam energy. Our simulated depth dose curve reaches a dose maximum of $D_{max} = 0.097$ Gy/pC/s at a depth of $R_{100} = 1.93$ cm. The depth of dose maximum and the shape of the depth dose curve around this depth is determined by the balance of scatter effects with a loss of electrons from the beam, therefore it depends on beam energy and scattering conditions (irradiation geometry, field size and shape, accelerator head design etc.). The therapeutic range, defined as the depth where the absorbed dose equals 90 % of D_{max} ($D_{90\%}$) represents a relatively uniform dose region which can be used effectively for practical applications. In our case the therapeutic range is around 5 cm, which can also change depending on irradiation geometry.

The distal part of the curve is described by the dose gradient, which is steeper for low energies and becomes less steep as the energy increases. In practice, this distal part of the depth dose curve can also be described by the depth (R_{50}) where the depth dose becomes half of the maximum ($D_{50\%}$). However, this characteristic is significantly affected by the components of accelerators as well as by the medium in which the electrons propagate.

The simulated electron beam at the focal point has a diameter of $0.3 \mu\text{m}$ in the transverse plane and has a bunch length of $20 \mu\text{m}$. The divergence angle is 0.9° , which results in a beam size of 3.14 cm at 100 cm source to surface distance at FWHM (Fig. 2.4a), which grows to 4.1 cm at the depth of dose maximum (Fig. 2.4b). This electron beam produces a dose distribution having a transverse profile with a high central dose, which rapidly falls forming a non-uniform transverse dose distribution. This significantly affects the usability of the beam.

The above results were obtained using the electron beam parameters taken from PIC simulations, which describe the electron bunch right after it exits the plasma medium. However, the electron beam suffers considerable changes during propagation towards the irradiation target. These changes strongly correlate with the design and components of the accelerator and affect both dose distribution and the usability of the beam. In this raw form this electron beam presents favorable properties for radiotherapy, but further beam preparations are needed for real applications. The geometrical properties (field shape and dimensions) are too large for irradiation techniques which use pencil beams and too small for conventional techniques that usually require square fields measuring 25 cm. Furthermore, the mean free path of such energetic electrons is too small to form the electronic equilibrium, which leads to difficulties in dose measurements. Therefore, for real applications rectangular fields up to $25 \text{ cm} \times 25 \text{ cm}$ are needed. Such fields can be achieved using either a dual scattering foil system or the spot scanning technique. The former is the most common technique used in LINAC based radiotherapy systems due to its reliability.

A dual scattering foil consists of a scatterer foil and a second flattening foil. The former is made from a material with a high atomic number, and it has an optimal thickness which produces the desired scattering effect. The second foil is made from a material with a low atomic number, it has a conical shape and is designed to flatten the scattered beam. When designing such a system one needs to consider the size and flatness of the obtained beam as well as the decrease in the number of electrons, the degradation of the energy spectrum (broadening and shifting toward the lower energies) and the Bremsstrahlung photon contamination. However, even a carefully designed system may suffer from beam degradation, which can be compensated by the adjustment of the incoming beam parameters (particle number, energy, etc.)

We performed a few simulations to estimate the feasibility of this solution, although the development of a dual scattering foil system is beyond the scope of this paper. Using Au foil as the scattering foil and a conical Al foil as the flattening foil, together with a rectangular diaphragm to collimate the beam to the desired shape we obtained a rough dose rate estimate. The dose rate obtained for two beams with fields of $15\text{ cm} \times 15\text{ cm}$ and $20\text{ cm} \times 20\text{ cm}$ is 1.1 mGy/pC/s at a depth of 1.8 cm and 0.9 mGy/pC/s at a depth of 2.2 cm , respectively. From these preliminary results we can conclude that, without a significant increase in the pulse charge, this solution is not applicable in this case.

In contrast, the scanning beam technique seems to be a viable alternative to produce larger field sizes. Based on our MC simulations, we can demonstrate that with the available dose rate obtained with 1 pC pulse charge, the spot scanning system can produce a beam size of $20\text{ cm} \times 20\text{ cm}$ in a few tens of milliseconds, with a central axis depth dose of about 0.275 mGy at the depth of dose maximum. This means that the dose rate which can be achieved with the spot scanning method is 1.65 Gy/min/pC . Considering the pulse charge of 3 pC , obtained from PIC simulations, the dose rate improves to a modest but usable value of 4.95 Gy/min . These results were obtained by simulating the spot scanning technique using the previously generated depth dose data. Fig. 2.5 presents the dose maps, the depth dose curve and profile at the depth of dose maximum for a beam field of $20\text{ cm} \times 20\text{ cm}$.

This result was obtained by simulating the spot scanning technique using the previously generated depth dose data. As it can be seen, both the beam width, and the therapeutic range are enlarged, and dose profile homogeneity also improves due to the increased field size, which ensures an electron equilibrium in the central part of dose distribution.

Our results suggest that this LWFA acceleration technique can be a promising alternative for RF-based conventional LINAC electron accelerators. The beam energy and charge can be changed by modifying the target length and plasma density via changing the gas jet pressure, even during the operation. This will enable researchers to perform intensity and energy modulated irradiation.

Moreover, theoretical studies suggest several possible novel applications of the presented LWFA system. Due to the small divergence of the beam, it is relatively easy to further narrow the beam and produce pencil beams for spot scanning techniques. Furthermore, we see the possibility of producing so called micro-beams whose enhanced biological effects are extensively researched.

The bunch length (pulse duration) of an electron shot is comparable to that of the laser

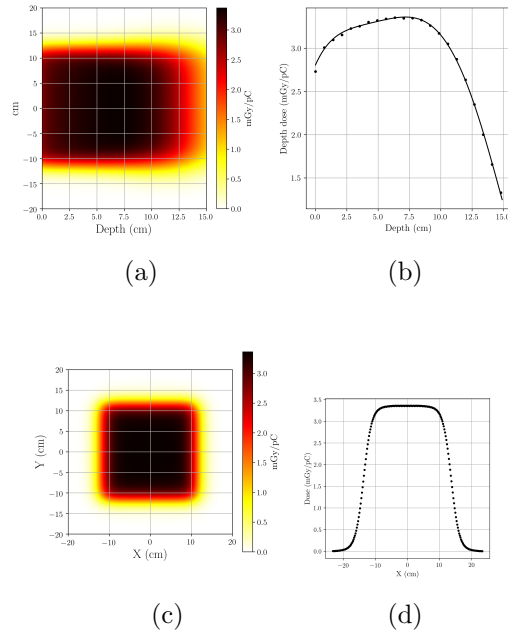


Figure 2.5: Dose map, depth dose curve and dose profile at maximum dose depth, obtained with the spot scanning technique. The dose distribution was obtained by summing as many beams as necessary to produce a 20 cm \times 20 cm square beam. In Fig. 2.5a it can be observed that the therapeutic range is enlarged, due to the electronic equilibrium, which is only partially realized in case of original beam.

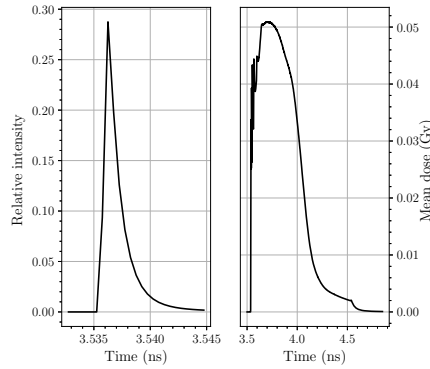


Figure 2.6: The time structure of the electron bunch at 100 cm from the acceleration site and the time structure of the dose deposition events.

pulse, which is 8 fs. At 100 cm from the source, the electron pulse duration stretches to a mean time length of 2 ps at FWHM of electron time distribution (with a full time duration of 160 ps, Fig. 2.6). As a consequence, the instantaneous dose rate of an electron shot with 1 pC charge is 6×10^5 Gy/s, which can be higher if we consider a higher pulse charge.

However, the time interval in which the beam energy is imparted to the matter is larger (300 ps mean time), and is less sharp than the pulse time itself (1.46 ns full time length of dose deposition events). This can be attributed to the considerable scattering of electrons. Nonetheless, the instantaneous dose rate remains relatively high, 0.7×10^5 Gy/s at a pulse charge of 1 pC. This very high instantaneous dose rate can open a new way to studying the so-called FLASH effects where the ultrahigh instantaneous dose rate can substantially enhance the therapeutic window ([43, 134, 44]). However, it is important to note that the conditions to produce the FLASH effect are not clearly defined in the literature. It seems that the instantaneous dose rate may be one of the conditions, however, the repetition rate must be not too high to mitigate the oxygen scavenging effect of a high dose rate (see Wilson et al. [134]).

As we can see, there are many possibilities as well as issues to be solved prior to real applications. Our *in silico* study represents a promising start for further scientific work on laser-driven electron source development. As soon as the experimental facility is assured, intensive work is planned to find the best beam steering solution, to develop the suitable beam monitoring and dosimetry system and to realize the necessary technical conditions for the first radiobiological experiments.

Chapter 3

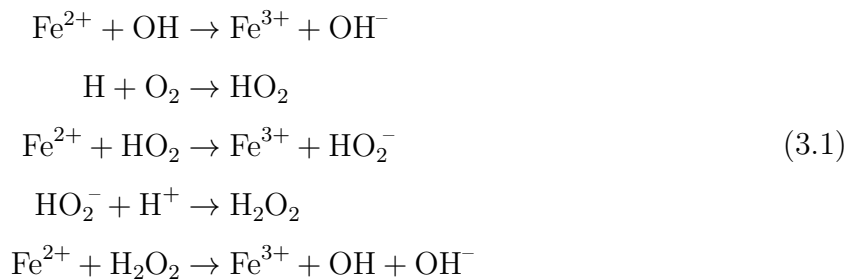
Enhanced FBX dosimeter system for reference dosimetry in radiobiology

3.1 Introduction

3.1.1 The Fricke chemical dosimeter

Ferrous ammonium sulphate based chemical dosimeters are well known in dosimetry. Their most common form, known as the Fricke dosimeter system, is made from 1 mM ferrous ammonium sulphate, 1 mM sodium chloride and 0.4 M sulphuric acid, which can be used in the absorbed dose range from 20 Gy to 400 Gy. The ISO/ASTM51026-15 [2] international standards recommend that the Fricke dosimetry system can be used as a reference standard dosimeter. However, due to time and technical constraints, it is not used in routine radiotherapy practice or radiobiological experiment dosimetry. These applications require a lower detection window with an upper dose limit of 20 Gy.

In the Fricke solution Fe^{2+} ion is oxidized by the radicals formed during the radiolysis of solution. The primary species formed by radiolysis in acid aqueous solutions are the H, OH, H_2O_2 and H_2 radicals. A simplified reaction mechanism of the process can be written as [131]:



In this reaction chain the modifications caused by NaCl are not considered. The presence of NaCl desensitizes the system against organic impurities but simultaneously introduces a dose rate dependence, which becomes considerable in the high dose rate domain.

Ferrous ammonium sulphate based dosimetry can be considered as a precise method to measure Fe^{3+} concentration produced by ionizing radiation. This can be performed measuring the absorbance at a certain wavelength, and the dose can be calculated from this value with the following equation:

$$D = \frac{A - A_0}{\epsilon \rho d G(\text{Fe}^{3+})}, \quad (3.2)$$

where A and A_0 are the absorbance of irradiated and non-irradiated reference solutions, respectively, ϵ is the molar absorption coefficient, ρ is the density of the solution, d is the optical path length used in spectrophotometric determination and $G(\text{Fe}^{3+})$ is the radiochemical yield of the Fe^{3+} ions. The ferric ion radiochemical yield represents the number of ferric ions formed in the solution per unit of absorbed dose to the solution. It can be determined spectrophotometrically with high accuracy.

However, the Fricke solution usually is used in industrial applications, due to its relatively low radiochemical yield of ferric ions. Several attempts have been made to sensitize the conventional Fricke solution. The addition of organic compounds usually increases the sensitivity of the solution, but the response becomes nonlinear with dose.

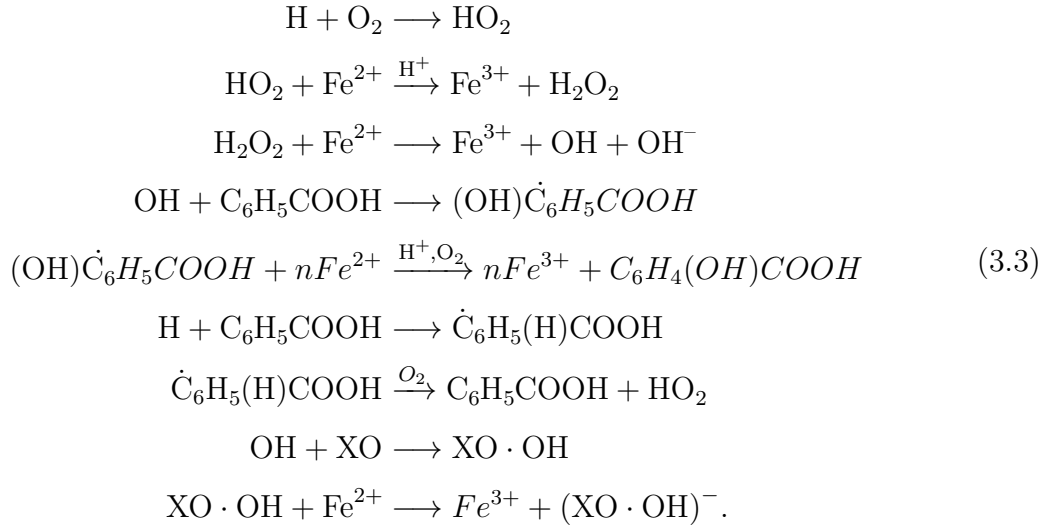
The nonlinear response to absorbed dose may be due to the reduction of ferric ions by some of the radicals formed by radiolysis. However, in light of the evidence, this behaviour can be explained qualitatively as well as by the spur theory of water radiolysis, which states that the initial radiolysis species of water exist in a spur. These species then diffuse in the medium and react forming intermediates and the final product, Fe^{3+} ions. The probability of interaction with Fe^{2+} ions is determined on the basis of the concentration of Fe^{2+} ions and the initial radiolysis species, as well as the spatial distribution of these spurs. The spatial distribution of spurs is strongly related to the linear energy transfer (LET) value of radiation. At high LET, spurs are superposed, whilst at low LET the spatial distribution of spurs is scattered. This means that the radiochemical yield of ferric ions is lower at high than at low LET radiations, because the probability of a reaction with a Fe^{2+} ion is higher when the spatial distribution of spurs is scattered, and the probability of a reaction with a Fe^{2+} ion at the same LET radiation level is higher in case of higher Fe^{2+} ion concentrations.

3.1.2 The ferrous ammonium sulphate – benzoic acid – xylenol orange dosimeter

Ferrous ammonium sulphate – benzoic acid – xylenol orange (FBX) dosimeters belong to the group of ferrous sulphate based chemical dosimeters which can be used for low dose applications, up to 20 Gy. The original FBX chemical dosimeter was developed by Gupta, B.L. [151] and is made from 0.2 mM ferrous ammonium sulphate, 5.0 mM benzoic acid and 0.2 mM xylenol orange in 25 mM sulphuric acid. In this system benzoic acid increases the radiolytical oxidation of Fe^{2+} ions, which subsequently bind to the xylenol orange dye molecules and form a complex with an absorption line around 540 nm. This line can be subsequently detected and measured.

The radiation chemistry of this system has been studied in detail by Geisselsoder et al. [152], Gupta et al. [153], [154], [155], [156], [157] and Jia-Shan et al. [158]. In FBX solution, each H_2O_2 and HO_2 radicals oxidizes one ferrous ion, respectively, while one OH radical is generated. This radical further reacts with benzoic acid and leads to the oxidation of ferrous ions through a chain reaction [153] producing hydroxycyclohexadiemyl radicals, which may also oxidize the ferrous ions to ferric ions by a chain reaction and change to hydroxy-benzoic acids [158]. Furthermore, benzoic acid can effectively compete with oxygen for a hydrogen atom [153].

The xylenol orange may react with OH radicals and produce $(XO \cdot OH)$ radical, which can oxidize one ferrous ion [156]. The overall chemical change can be summarized in the following reaction scheme:



Its chemical yield has been determined for different beam qualities. For example, Gupta et al. [159] measured the chemical yield for $^{10}B(n, \alpha)^7Li$ neutron beam, while Bhat et al. [160] and Semwal et al. [161] measured the response to ^{12}C and 7Li ions. Low dose rate and dose fractionation FBX dosimeter responses were also studied by Gupta and Madhvanath [162], [163].

Thanks to its high sensitivity, the FBX dosimeter can be used for a variety of applications. Gupta et al. [164] studied the possibilities of using the FBX dosimeter for ^{60}Co therapy unit calibration and quality assurance [164], [165]. Moussous et al. [166] used the FBX dosimeter for measuring dosimetric parameters, and Gupta et al. [167] studied the usability of chemical dosimetry techniques, including the FBX solution, for various applications under different geometries.

To date, several attempts have been made to further enhance the FBX dosimeter. For example, Brindha et al. [168] introduced the stock solution techniques in the preparation process to increase the shelf-life of prepared solutions, while Upadhyay et al. [169] modified the FBX composition to obtain a more tissue-equivalent composition, resulting in its use for neutron dosimetry.

Moreover, xylenol orange (XO) is used as an analytical tool in chemistry for the determination of iron ion concentration. The protocol established by Gay et al. [170] to measure Fe^{3+} concentration differs slightly from the FBX method. The measured

wavelength is stated as 560 nm, and the amount of the xylenol orange is increased to ensure that the absorbance of the XO-Fe complex is independent of the concentration of XO. This occurs when the XO:Fe³⁺ ratio is above 3. Xylenol orange dye is added to the Fe³⁺ ion solution before the spectrophotometric measurements using pre-prepared stock solutions. The method described by Gay et al. [170] is recommended to measure the Fe³⁺ ions in concentrations between 5 μ M and 50 μ M. We started out from this study to improve the sensitivity of our FBX dosimeter.

3.1.3 The sources of uncertainties

All quantities in Equation (3.2) are subject to some uncertainties. Density can be measured with relatively high precision, and its variation in the prepared solutions is negligible. The cuvette optical path length is well defined by the manufacturer, and in most cases it has a 0.5% error. Both the molar absorption coefficient and the radiochemical yield depend on the accuracy of the measurements of the optical absorbance of solutions with different Fe³⁺ concentrations.

The relation between the relative uncertainty of the measured absorbance can be derived using the Lambert-Beer law of optical absorption. It has a minimum at $A = 0.43$, where the theoretical relative uncertainty is 0.2% [171]. Below $A = 0.2$, relative uncertainty increases considerably, and for very low absorbance, this tends to infinity. The concentration of Fe³⁺ ions in a freshly prepared FBX solution is around 1.36 μ M, depending on the purity, storage time and conditions of the Fe²⁺ salt. This concentration corresponds to an absorption of $A = 0.02$ and a theoretical relative uncertainty of 1.6% in spectrophotometric measurements.

It is well known that a more than 5% difference in absorbed dose can lead to considerable differences in the outcomes of radiobiological experiments or radiotherapy procedures. Therefore, the reproducibility of radiobiological experiments or the replicability of treatment results depend on the precision and accuracy of dosimetric measurements. The main objective of this work was to develop an FBX formula based, enhanced chemical dosimetry system to be used in radiobiological research as a routine reference dosimetry method in various irradiation arrangements where common dosimetry tools are not suitable or are difficult to use. To achieve this, a standard operational procedure has been established and validated to guarantee the necessary accuracy and precision. Related to this, we have developed a custom designed multipurpose PMMA slab phantom to ensure reference irradiation conditions.

3.2 Methods

Dosimetric solutions were prepared from analytical grade reagents and HPLC grade water using suitably cleaned glassware. A high level of laboratory cleanliness was established and maintained through an in-house practice protocol. Reagents were weighed with the help of a calibrated analytical balance, precision pipettes, class A cylinders and volumetric flasks. Apart from the ferrous ammonium sulphate stock solution all prepared solutions were stored in dark media bottles with screw caps at room temperature.

3.2.1 Dosimeter preparation

The dosimetric solutions were prepared from pre-prepared stock solutions, based on the following preparation procedure:

- Sulphuric acid stock solution – All stock solutions were made with 25 mM H_2SO_4 , which was prepared before use from 0.5 M analytical grade sulphuric acid solution (5 ml 0.5 M H_2SO_4 dissolved in 100 ml HPLC water). The latter was obtained from concentrated H_2SO_4 solution (an ampoule contains 49.04 g H_2SO_4 , Firma Chempure) and stored in dark screw-cap bottles at room temperature.
- The ferrous ammonium sulphate stock solution (FS) – ammonium Fe^{2+} sulphate hexahydrate ($(\text{NH}_4)_2\text{Fe}(\text{SO}_4)_2 \times 6\text{H}_2\text{O}$, 3.921 g, Sigma-Aldrich) was dissolved in sulphuric acid (H_2SO_4 , 25 mM, 50 mL). This was further diluted with 25 mM H_2SO_4 (100 mL). The resulting solution of ferrous ammonium sulphate (100 mM) was stored in a refrigerator to prevent the thermal oxidation of iron ions.
- The benzoic acid stock solution (BA) – benzoic acid ($\text{C}_7\text{H}_6\text{O}_2$, 1.974 g, Sigma-Aldrich) was dissolved in sulphuric acid (H_2SO_4 , 25 mM, 900 mL). This was further diluted with 25 mM H_2SO_4 (100 mL). The final solution was 16.16 mM benzoic acid. (Dissolution can be accelerated by heating.)
- The xylenol orange stock solution (XO) – xylenol orange disodium salt ($\text{C}_{31}\text{H}_{30}\text{N}_2\text{Na}_2\text{O}_{13}\text{S}$, 179.16 mg, Sigma-Aldrich) was dissolved in sulphuric acid (H_2SO_4 , 25 mM, 50 mL) and was then further diluted with 25 mM H_2SO_4 (100 mL).

The dosimetric solution was prepared in a 100 mL volumetric flask using 1 mL FS stock solution diluted with the BA stock solution, which resulted in a 1 mM ferrous ammonium sulphate, 16 mM benzoic acid solution in 25 mM sulphuric acid. This solution was stored, until use, in dark screw-cap bottles or in sterile Eppendorf tubes in a refrigerator.

3.2.2 Reference irradiation

All irradiation was performed in reference conditions using an in-house made PMMA slab phantom and different beam qualities. A conventional LINAC ($SSD = 100$ cm, field size 15 cm \times 15 cm) was used for 6 MV and 15 MV photon beams and for 6 MeV, 9 MeV and 12 MeV electron beams, respectively. A cell and small animal irradiator facility was used (Xstrahl, RS320 type self-contained X-Ray irradiator) for 250 kVp X-ray beams ($HVL = 1.53$ mm Cu equivalent).

Figure 3.1 shows the PMMA slab phantom which measures 30 cm \times 30 cm and has variable heights which can be changed using slabs with different thicknesses. The 2.5 cm thick sheet has a 15 cm \times 15 cm square hollow in the middle with a depth of 1.5 cm, in which different inserts with the same dimensions can be placed. These inserts are prepared to hold different sample vials: 0.5, 1.5, 2 mL Eppendorf tubes, well plates and cell culture dishes. This slab phantom can be used for the reference irradiation of dosimetric solutions, dosimetric films or both at the same time, and for the irradiation of different radiobiological samples (cell cultures, Zebrafish embryos etc.).

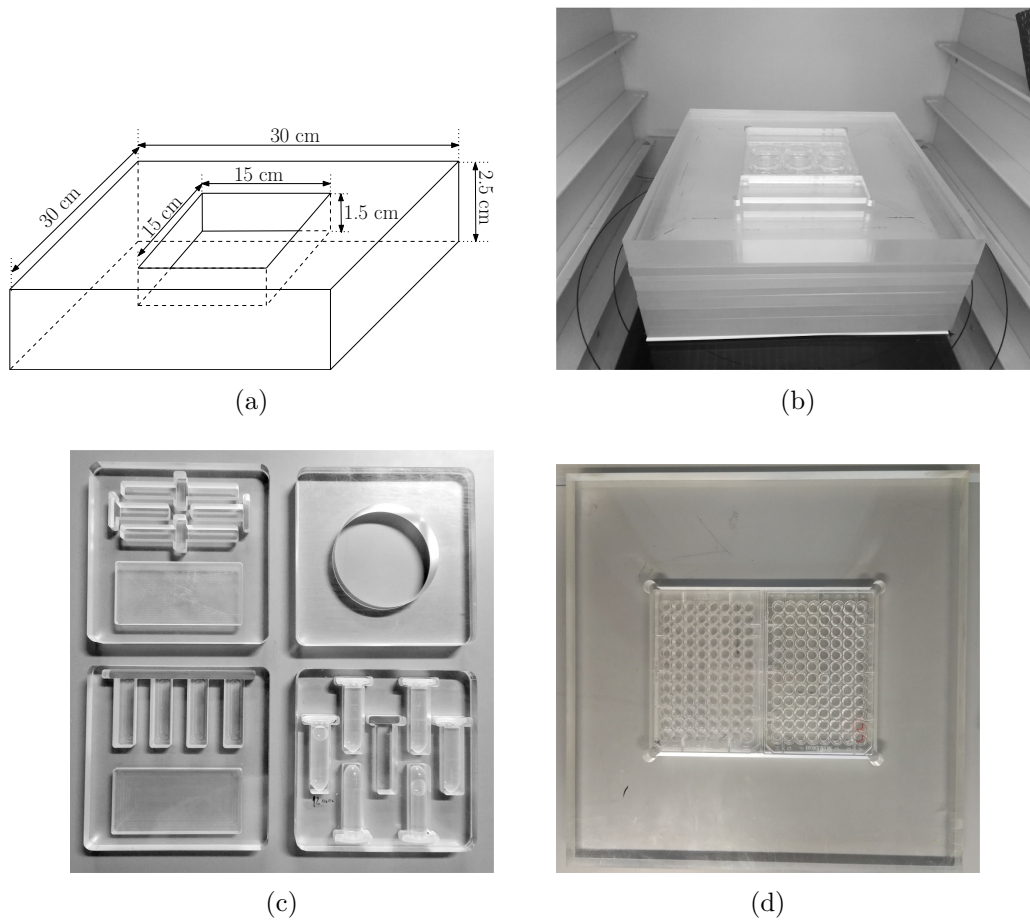


Figure 3.1: Acrylic slab phantom for reference irradiation. The phantom has two functional parts: a 30 cm \times 30 cm PMMA sheet with different thicknesses for variable PMMA phantom heights (3.1b) and a PMMA sheet with thickness of 2.5 cm with a 15 cm \times 15 cm and 1.5 cm deep hollow in the middle which can accept inserts with the same dimensions (3.1a). These inserts are designed to accept different types of sample holders (3.1c). Another piece of 2.5 cm thick PMMA sheet is designed to house one or two multi-well plates with dosimetric solutions or biological samples (3.1d).

Samples for conventional LINAC irradiation were placed at an equivalent depth chosen so that 1 MU would yield the same dose as in water. This was determined by a series of measurements made with a PTW Unidose universal dosimeter and a Farmer type ionization chamber calibrated with a secondary standard in terms of absorbed dose to water.

In the cell and small animal irradiator, a beam hardening filter (consisting of a 1.06 mm aluminium foil and a 0.51 mm copper foil) was used to obtain an X-ray beam quality equivalent to $HVL = 1.53$ mm Cu. The correction factor of $k_{Q_0} = 0.9978$ was determined through the interpolation of the beam quality factors provided by the calibration labora-

tory. The reference dose measurements were carried out in a PTW RW3 type solid slab phantom with a PTW Farmer Chamber type 30013, and a PTW Unidos^{webline} dosimeter calibrated relative to water.

The absorbed dose was measured in a RW3 solid slab phantom used for daily calibrations. The measured dose was converted into absorbed dose to water using the manufacturer's conversion factors. Data were available neither for the 250 kVp X-ray RW3 solid slab phantom, nor for the plexi slab phantom. Consequently, a phantom dose conversion factor was determined using the procedure published by Seuntjens et al. [172]. The depth dose was measured in water at different depths (z_{ref}) and in the RW3 and PMMA slab phantoms at an equivalent depth (z_{eq}). The phantom dose conversion factor was calculated with the following equation:

$$k_{s,w}^Q = \frac{M_w^Q}{M_s^Q}, \quad (3.4)$$

where $k_{s,w}^Q$ is the phantom dose conversion factor, M_w^Q is the ionization chamber readings in water at reference depth z_{ref} and M_s^Q are the ionization chamber readings in the slab phantom at equivalent depth z_{eq} with the same Q beam quality and corrected for influence quantities.

The equivalent depth is the inverse ratio of the relative electron densities (ρ_e) in the two phantom materials using the following equation[172]:

$$\frac{z_{eq}}{z_{ref}} = \frac{\rho_e^w}{\rho_e^s}. \quad (3.5)$$

Equation (3.5) should be used in conjunction with a similar equation for the ratio of the reference and equivalent field size. However, for the lack of an appropriate collimator, these conditions were not reproducible and because it does not significantly affect the final results, we neglected this condition.

Table 3.1 shows the equivalent depth and the phantom dose conversion factor for RW3 and PMMA, and for the 250 kVp X-ray ($HVL = 1.53$ mm).

3.2.3 Spectrophotometric measurements

After irradiation, 0.1 mL xylenol orange stock solution (XO) was added to each 0.9 mL of irradiated dosimetric solution. The final solution contained 0.25 mM xylenol orange disodium salt. After waiting at least ten minutes for the xylenol orange to form complexes with the Fe^{3+} ions [170], we measured the solution's absorbance at 560 nm against the xylenol orange blank solution. The blank sample was prepared in a sample vial from the XO stock solution (0.1 mL) and sulphuric acid (0.9 mL 25 mM), in the same manner as the dosimetric samples.

Absorption measurements were performed using an UV-VIS spectrophotometer (Lambda 35, Perkin Elmer, double light path) and a quartz cuvette with a 1 cm path length. The recommendation of the ISO/ASTM 51026:2014 standard was followed to ensure the reproducibility and accuracy of the measurements.

Water $z_{ref}(\text{cm})$	RW3		PMMA	
	$z_{eq}(\text{cm})$	$k_{s,w}^Q$	$z_{eq}(\text{cm})$	$k_{s,w}^Q$
0.5	0.5	0.9539	0.4	0.9329
1.0	1.0	0.9492	0.9	0.9262
1.5	1.5	0.9421	1.3	0.9128
2.0	2.0	0.9241	1.7	0.8874
2.5	2.5	0.9158	2.2	0.8762
3.0	3.0	0.9122	2.6	0.8633
3.5	3.5	0.9083	3.0	0.8490
4.0	4.0	0.8893	3.5	0.8270
4.5	4.4	0.8837	3.9	0.8183
5.0	4.9	0.8785	4.3	0.8011

Table 3.1: Phantom dose conversion factor for RW3 and PMMA materials

3.2.4 Density measurements

The density of the eFBX solution was measured with an Anton Paar DMA 35 portable density meter (accuracy, 0.001 g/cm^3) and the classical gravimetric method. The results of the two methods were compared and a mean value was generated.

3.2.5 Determination of the molar mass absorption coefficient

A simplified version of the recommendations of ISO/ASTM 5106:2014 were followed to determine the molar absorption coefficient. An Fe^{3+} stock solution was prepared by dissolving ammonium iron(III) sulphate dodecahydrate (Sigma Aldrich, 4.82 mg) in sulphuric acid (25 mM, 50 mL), and was then diluted down to 100 mL. From this stock solution and the BA stock solution a series of samples were prepared with Fe^{3+} ion concentrations between $10 \mu\text{M}$ and $60 \mu\text{M}$, and 0.1 mL XO stock solution was added to each 0.9 mL solution.

The concentration of Fe^{3+} ions for each sample was determined by measuring absorption at 560 nm. The molar linear absorption coefficient was obtained from the gradient of the plot of the absorbance/path length versus concentration.

3.2.6 Determining the radiochemical yield of ferric ions

The radiochemical yield of ferric ions $G(\text{Fe}^{3+})$ was determined using a freshly prepared eFBX solution that was irradiated with different doses in 2 ml Eppendorf tubes using the PMMA slab phantom and the reference irradiation geometry. Optical absorption was measured for irradiated and nonirradiated samples and $\Delta A_i = A_i - A_0$ were calculated, where A_i is the absorption of the irradiated sample and A_0 is the absorption of the nonirradiated sample.

Plotting $\Delta A/\epsilon\rho$ values as a function of dose results in a linear correlation where the gradient corresponds to the radiochemical yield of ferric ions ($G(\text{Fe}^{3+})$).

3.2.7 Dose determination

Whenever possible, we irradiated at least three FBX samples, together or separately, with the same dose. After irradiation we performed spectrophotometric measurements, and using Equation (3.2) we calculated the absorbed dose from the obtained absorption value.

The absorbed dose to water, D_w , can be determined from the mean absorbed dose using the relation:

$$D_{\text{water}}^{z_{ref}} = k_{w,\text{PMMA}} \cdot D_{\text{PMMA}}^{z_{eq}}, \quad (3.6)$$

where $k_{w,\text{PMMA}}$ is the PMMA to water conversion factor, calculated as the ratio of the measured dose in water at reference depth ($D_{\text{water}}^{z_{ref}}$) and the dose in PMMA at equivalent depth ($D_{\text{PMMA}}^{z_{eq}}$).

3.2.8 Diluted eFBX solution measurements

For the measurement of doses with volumes less than 1 ml, the irradiated eFBX solution was diluted with a well defined amount of nonirradiated eFBX solution. XO stock solution was added to these diluted eFBX solutions. Based on the degree of dilution, the change in absorbance induced by the absorbed dose can be calculated with the following formula:

$$\Delta A = \frac{A_m - (1 - \frac{1}{9}\beta)A_0}{0.9 - \beta}, \quad (3.7)$$

where ΔA is the change in absorbance, A_m is the measured absorbance of samples without correction, A_0 is the absorbance of the nonirradiated solution and β is equal to the ratio of the solvent volume and the total volume of samples $\beta = V_0/V_T$.

3.3 Results and discussion

3.3.1 Sensitivity

To improve the sensitivity of the FBX dosimeter, attempts have been made to increase the chemical yield of ferric ions and to enhance the photometric measurement techniques by applying Gay et al.'s [170] recommendation. We performed a series of experiments varying the chemical composition to increase the sensitivity of the FBX dosimetric solution.

It is well known that the radiochemical yield of Fe^{3+} ions is higher in the ferrous sulphate – benzoic acid system (FB) than in the ferrous sulphate – benzoic acid – xylenol orange system (FBX)[153].

Studying the relation between the response of the FB system and the concentration of benzoic acid has revealed that the chemical yield of Fe^{3+} ions can improve if the amount of benzoic acid is increased in the system. The variation of absorbance as a function of BA

concentration is shown in Figure 3.2. When the FB samples with increased benzoic acid concentration were irradiated with 4 Gy, the response showed saturation effects, which became significant above 7.5 mM of benzoic acid. However, the response curve was not completely saturated in the measured concentration range. The extrapolation of the data revealed that complete saturation occurs above 16 mM.

On the other hand, variations in benzoic acid concentrations, due to poor measurement or improper dilution do not significantly influence the dosimetric response of the solution. Figure 3.2 shows that a change in the BA concentration from the standard 5 mM to 16 mM results in an 8% increase in absorbance, which corresponds to an 8% growth in radiochemical yield. At the same time, there is a 0.3% difference in absorbance at 14 mM and 16 mM. Therefore, at higher benzoic acid concentrations the error which may occur in the solution preparation process is negligible.

A further increase in benzoic acid concentration is hindered by its poor solubility in water (21.9 mM at 18 °C). No further improvements in absorbance are expected above 16 mM, so there is no point in experimenting with even higher concentrations.

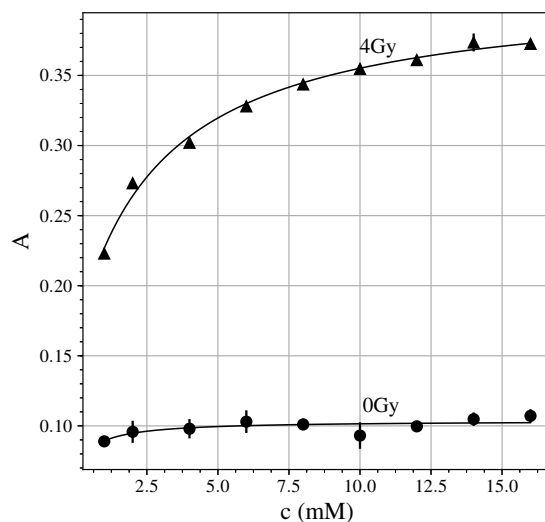


Figure 3.2: Optical absorbance as a function of benzoic acid concentration for irradiated solution and for nonirradiated solution.

3.3.2 The problem of nonlinearity

As already mentioned in the introduction, the main drawback of the FB system is that there is a nonlinear response to dose. This behaviour was reported by Gupta et al. [153] and shown in Figure 3.3, where the dose response of the Fricke and FBX dosimeters is nonlinear above 5 Gy in the FB system.

Based on the spoor theory, the nonlinearity of the FB solution suggests that the solution becomes saturated at high doses, which means that there is a reduced probability of

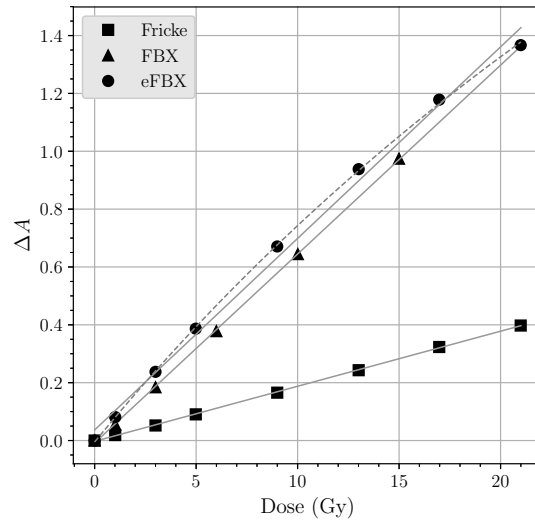


Figure 3.3: Dose response curve of different dosimetric solutions for a standard Fricke solution, measured with xylenol orange techniques; an FBX solution and an FB solution.

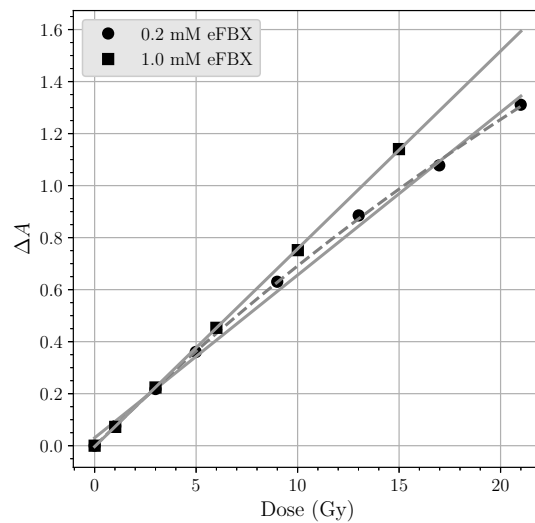
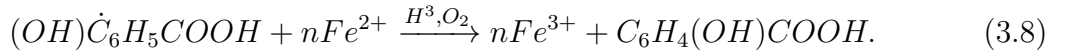


Figure 3.4: The effects of increased ferrous sulphate concentrations. The lower line is the graph of linear fitting of the measurement points (marked with circles) in case of eFBX solutions with 0.2 mM ferrous sulphate concentration. The dashed line is the graph of fitting with a rational function of the same measurements points. The upper line represents the graph of linear fitting of the measurements points (marked with squares) obtained with 1 mM ferrous sulphate concentration.

a reaction with a Fe^{2+} . This in turn leads to a decreasing chemical yield, which prompted us to remove the nonlinearity of the system by increasing the Fe^{2+} concentration. Figure 3.4 shows the effects of increasing the ferrous ammonium sulphate concentration from 0.2 mM to 1 mM, which corresponds to the ferrous ammonium sulphate concentration of the classical Fricke dosimeter.

3.3.3 Radiochemical yield of ferric ions

In the FB system each hydrogen atom oxidizes two ferrous ions, and each hydrogen-peroxide molecule oxidizes one ferrous ion, while one hydroxyl radical is produced. This secondary hydroxyl radical reacts with benzoic acid and forms hydroxycyclohex-adienyl radicals, which oxidize the ferrous ions in a chain reaction [158]:



Concurrently, benzoic acid can effectively compete with oxygen for H atom releasing HO_2 radicals [153]. Gupta et al. [153] showed that the radiochemical yield for the FB system can be written as:

$$G(\text{Fe}^{3+}) = 12 \cdot G_{\text{H}_2\text{O}_2} + 11 \cdot G_{\text{OH}} + 13 \cdot G_{\text{H}}, \quad (3.9)$$

where $G_{\text{H}_2\text{O}_2} = 0.79 \cdot 10^{-7}$ mol/J, $G_{\text{OH}} = 2.9 \cdot 10^{-7}$ mol/J and $G_{\text{H}} = 3.5 \cdot 10^{-7}$ mol/J are the radiochemical yield of hydrogen peroxide, hydroxyl radical and atomic hydrogen, respectively.

However, in the FBX system, H_2O_2 oxidizes 8 ferrous ions instead of 12, and the xylenol orange competes for OH radicals with benzoic acid, producing $\text{XO} \cdot \text{OH}$ radical, which can oxidize one ferrous ion. According to Jia-Shan et al. [158] and Gupta et al. [153] the reaction chain length of the oxidation of Fe^{2+} decreases and Equation (3.9) can be written as:

$$G(\text{Fe}^{3+}) = 8 \cdot G_{\text{H}_2\text{O}_2} + 7 \cdot G_{\text{OH}} + 11 \cdot G_{\text{H}}. \quad (3.10)$$

The radiochemical yield of Fe^{3+} ions in an FB solution with 5 mM benzoic acid concentration can be calculated using Equation (3.9) and is found to be $8.75 \cdot 10^{-6}$ mol/J. These measurements show that the radiochemical yield of dosimetric solutions with 16 mM is $9.08 \cdot 10^{-6}$ mol/J for a beam quality of 6 MV. This equals a 3.9% increase in yield, and is due to the higher benzoic acid concentration. Using the logic proposed by Jia-Shan et al. [158] we can conclude that in the presence of 16 mM benzoic acid, the OH radical oxidizes 12 rather than 11 Fe^{3+} ions, and Equation (3.9) becomes:

$$G(\text{Fe}^{3+}) = 12 \cdot G_{\text{H}_2\text{O}_2} + 12 \cdot G_{\text{OH}} + 13 \cdot G_{\text{H}}. \quad (3.11)$$

By using a concentration of 16 mM benzoic acid, and by irradiating an FB solution instead of an FBX solution, the radiochemical yield can be increased from a mean literature value of $6.89 \cdot 10^{-6}$ mol/J, to $9.08 \cdot 10^{-6}$ mol/J, which equals to a 24% enhancement. We named this system enhanced FBX (eFBX).

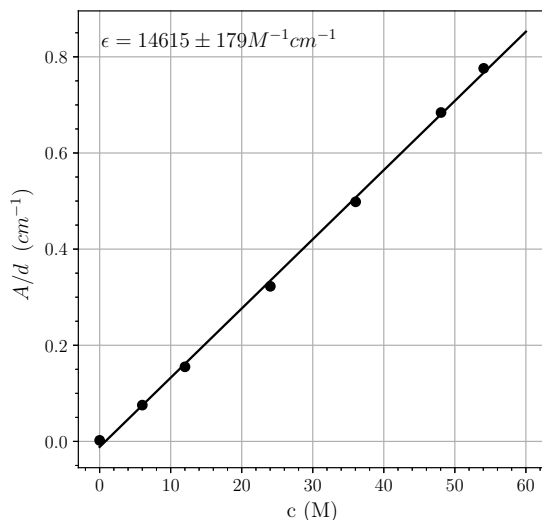


Figure 3.5: Graphical representation of absorbance variation as a function of Fe^{3+} ion concentrations. The gradient is the molar attenuation coefficient, $\epsilon = 14615 \pm 18 M^{-1} cm^{-1}$.

Our eFBX dosimetric solution has a density of $0.9978 g/cm^3$, and the measured molar attenuation coefficient is $14615 \pm 18 M^{-1} cm^{-1}$, which was obtained by fitting the measured absorbance at different Fe^{3+} concentrations (Figure 3.5). This value is in agreement with literature values, and any difference may be attributed to the degree of purity of xylenol orange dyes, which varies from manufacturer to manufacturer. This is a common problem, and it is always recommended to measure the molar attenuation coefficient when a new lot of xylenol orange is used. A summary of different molar absorption coefficient values was published by Moussous et al. [173].

The radiochemical yields of ferric ions resulting from different beam qualities are presented in Table 3.2. All values are in terms of dose to water, and were determined by applying the appropriate conversion factors.

The effects of the dilution of the irradiated solution were investigated to perform measurements with dosimetric solutions of less than 1 mL, for example solutions from single wells of a 96-well plate, $250 \mu l$. Table 3.3 shows $G(Fe^{3+})$ values for various diluted eFBX solutions, and it can be seen that to some extent the radiochemical yield values differ for diluted and nondiluted solutions. This can be attributed to some matrix effects the origins of which have not yet been identified.

We established a standardized measurement protocol to ensure that eFBX is an easy-to-handle chemical dosimeter. For this purpose, we started out from the ISO standard on the practice for using the Fricke reference standard dosimetry system. Our protocol describes the preparation, handling and storage of the solution; irradiation in reference conditions; the photometric measurements and subsequent data processing.

Stock solutions were introduced similarly to Brindha et al. [168] with some modifications for the preparation of dosimetric solutions. All but one of the stock solutions were stored at room temperature. The 1 mM FS stock solution was stored in a refrigerator due

Beam	$G(\text{Fe}^{3+})$ molJ^{-1}
6 MV photon	$9.08 \pm 0.17 \cdot 10^{-6}$
15 MV photon	$9.10 \pm 0.17 \cdot 10^{-6}$
6 MeV e^-	$8.98 \pm 0.15 \cdot 10^{-6}$
9 MeV e^-	$9.03 \pm 0.08 \cdot 10^{-6}$
12 MeV e^-	$8.97 \pm 0.26 \cdot 10^{-6}$
250 kVp X-ray	$6.46 \pm 0.08 \cdot 10^{-6}$

Table 3.2: The radiochemical yield of the eFBX dosimetric solution for different beam qualities.

Dilution	Sample ml	Solvent ml	$G(\text{Fe}^{3+})$ molJ^{-1}
4/0.9	0.9	2.6	$6.07 \pm 0.18 \cdot 10^{-6}$
4/0.5	0.5	3.1	$5.86 \pm 0.23 \cdot 10^{-6}$
4/0.25	0.25	3.35	$5.88 \pm 0.23 \cdot 10^{-6}$

Table 3.3: The radiochemical yield of diluted eFBX dosimetric solution for different dilutions grades. All values refer to 250 kVp X-ray beam quality.

to its short, two-week shelf-life (caused by the relatively high thermal oxidation rate of ferrous ammonium sulphate, which is a function of Fe^{2+} ion concentration and temperature). The BA and XO stock solutions can be stored at room temperature for a long time without any observable degradation.

The initial ferric ion concentration depends on the thermal oxidation of the dosimetric solution, which reduces the measurable dose range. The freshly prepared eFBX solution has an optical absorption of 0.1, which can increase to 0.3 with a change in ferric ion concentration over time. For this reason it is always recommended to use freshly prepared FS stock solutions to avoid any uncontrolled change in dosimetric solution consistency, and to ensure complete control over the quality of dosimetric solutions.

Figure 3.6 shows that the blank solution has considerable absorption at the maximum absorption wavelength (525 nm) of the eFBX system. This means that the Beer-Lambert law cannot be used here. A convenient method is to measure absorption at a different wavelength where there is no considerable xylenol orange absorption [170]. Hence, all photometric measurements were conducted at 560 nm, in accordance with the observations of Gay et al. [170].

It is also interesting to note that the xylenol orange technique can be successfully applied to standard Fricke solutions in the low dose domain. The initial concentration of ferric ions is the same as in the case of the eFBX solution, and the chemical yield of the Fricke solution is 1.6 mol/J [2]. The concentration change induced by irradiation

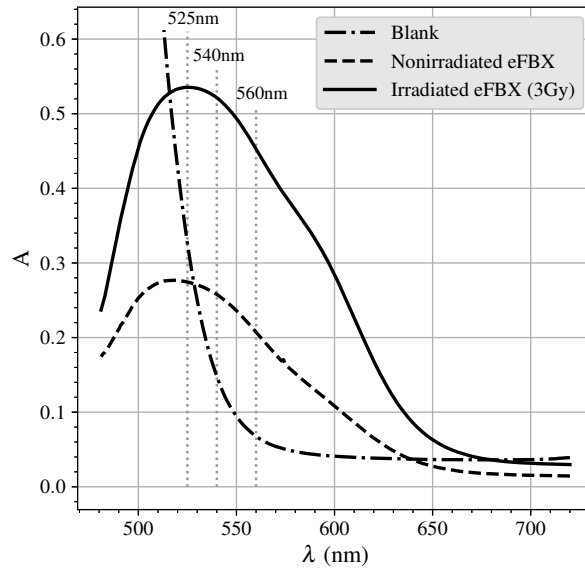


Figure 3.6: The absorption spectra of the blank solution and of the irradiated eFBX solution. The dotted vertical lines represent the wavelengths for maximum absorptions and for the actual measurement wavelength.

can be measured with the xylenol orange technique. If we apply this technique to the Fricke solution, the chemical yield is $1.62 \cdot 10^{-6}$ mol/J for a 6 MV photon beam and $1.44 \cdot 10^{-6}$ mol/J for a 250 kVp X-ray beam, respectively.

3.3.4 Uncertainty budget

Table 3.4 summarizes the uncertainty budget for eFBX dosimeter calibration, made using the recommendations of IAEA[94]. In this phase we encountered two major problems: the uncertainty of spectrophotometric measurements and that introduced by pipetting.

Theoretically, the most precise value for absorbance is $A = 0.434$, which is the minimum of function:

$$\frac{dA}{A} = -\frac{0.434}{10^{-A}A} dT, \quad (3.12)$$

where A is the absorbance and dT is the standard deviation of transmittance. Equation (3.12) can be obtained using the Lambert-Beer law [171] (Figure 3.7). The graph shows that the uncertainty of measurements at low absorbance is relatively high. In a freshly prepared eFBX dosimeter solution, absorbance is usually between 0.01 and 0.02, and increases with storage time. The relative uncertainty of absorption is between 3.12 % and 1.6 %. However, a rise in the concentration of ferrous sulphate to 1 mM in the eFBX dosimetric solution increases the absorbance of the freshly prepared solution to 0.1 with a theoretical relative uncertainty of 0.38 %.

The final ferric ion concentration of the eFBX solution is determined both by the absorbed dose and by the pipetting of the solution after irradiation. Section 2.3 states that for sample preparation 0.9 ml eFBX solution was extracted from the irradiated sample and 0.1 ml XO stock solution was added. Therefore, the final concentration of the solution was $0.9 \text{ ml} \cdot c_0 / (0.9 + 0.1) \text{ ml}$, where c_0 is the initial ferric ion concentration. If we apply the rule of propagation of uncertainty we obtain:

$$\left(\frac{\delta A_B}{A_B}\right)^2 = n \cdot \left(\frac{\delta V}{V}\right)^2 + \left(\frac{\delta A_m}{A_m}\right)^2 + \left(\frac{\delta A_0}{A_0}\right)^2, \quad (3.13)$$

where $\delta A_B/A_B$ is the total uncertainty of absorbance of the irradiated solution; $\delta A_m/A_m$ is the uncertainty of absorbance of the irradiated solution; $\delta A_0/A_0$ is the uncertainty of absorbance of the nonirradiated solution, which is discussed here separately, because low absorbance results in higher uncertainty, and $\delta V/V$ is the uncertainty associated with pipetting. Parameter n represents the volumes which were measured with a pipette. For example, two samples of 0.9 ml can be extracted with a 1 mL pipette from a single 2 ml Eppendorf tube. With the addition of the XO stock solution parameter n increases to 3. In an ideal situation, the uncertainty attributed to volume determination with a precise pipette is 0.2%. Equations 3.12 and 3.13 provide the combined uncertainties for absorbance measurements represented in Figure 3.7 (dotted line).

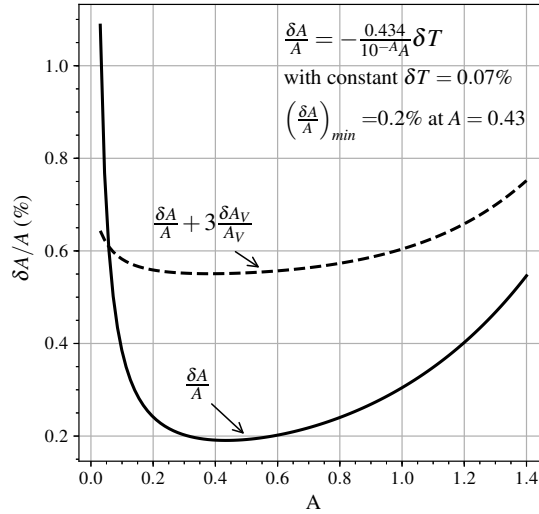


Figure 3.7: The relative uncertainties for the eFBX dosimeter due to the photometric measurements (solid curve) and due to the combination of photometric and volume measurements (dashed line).

Figure 3.7 shows that the uncertainty introduced by pipetting resulted in a greater but flatter relative uncertainty in absorbance measurements. In the 0.1 to 1.2 absorbance interval, the relative uncertainty is between 0.64% and 0.65% with a minimum of 0.55%.

This absorption interval corresponds to an absorbed dose range up to 9 Gy for 6 MV photon beams and up to 12 Gy for 250 kVp X-ray (with a $HVL = 1.53$ mm Cu equivalent).

Source of uncertainty	Relative standard uncertainty (%)	
	Type A	Type B
<i>Reference dose rate</i>		
N_k secondary standard	—	0.20
Positioning	—	0.02
Temperature and pressure correction	0.03	0.10
Measurement of current	0.05	0.10
<i>Calibration of OFBX solution</i>		
Positioning of dosimeter	—	0.02
N_{pw} plexi-water conversion	0.20	—
Photometric and volumetric correction	0.35	0.61
G value determination	0.6	—
ϵ determination	0.2	—
Temperature correction	—	0.50
Quadratic summation	0.75	0.83
Combined standard uncertainty	1.12	
Extended uncertainty (k=2)	2.24	

Table 3.4: Uncertainty budget of the eFBX solution. Temperature correction was calculated based on the relations used for the Fricke dosimeter[2] as the temperature dependence measurement has not yet been performed. The combined standard uncertainty without this term becomes 1.0%.

Table 3.4 summarizes these calculations and considers other sources of errors. The combined standard uncertainty can be considerably improved by eliminating uncertainty type B assigned to temperature correction. Temperature correction was not considered in this study, but on the basis of the spur theory and the increased amount of ferrous

sulphate in the final composition, a similar relation can be assumed between temperature and radiochemical yield as in case of the Fricke dosimeter [2]. The same connection is true for the temperature correction of absorbance measurements, which is related to the associated volume change with temperature. Correction for this variation means that the combined standard uncertainty becomes 1.0 %.

Chapter 4

Conclusion and new scientific results

Laser-driven particle acceleration represents a long-awaited breakthrough in the development of novel radiotherapy facilities. The feasibility and suitability of real particle beam parameters can be investigated using currently available high power laser systems. One of the main objective of this work was to theoretically investigate the potential application of high repetition rate LWFA electron beams for radiotherapy.

Electron beams produced in plasma by 1 kHz high repetition rate laser system may provide a promising alternative for conventional accelerators. In this study I have demonstrated that this laser system can produce electron beams with high energies (35.97 MeV mean kinetic energy) and acceptable dose rates (18 Gy/min considering the electron bunch charge of 3 pC obtained by PIC simulations) and dose delivered with very high precision, due to the high repetition rate of the system.

This results suggest that this LWFA acceleration technique can be a promising alternative for RF-based conventional LINAC electron accelerators. The beam energy and charge can be controlled by modifying the target length and plasma density via changing the gas jet pressure, even during the operation. This will enable researchers to perform intensity and energy modulated irradiation. The energy modulation and the spot scanning technique together could open extremely important application spectra for electron irradiation of superficial targets with uneven thickness, providing significant normal tissue protection.

Further efforts are needed to choose the best beam steering solution as well as to develop the suitable beam monitoring and dosimetry system. Taking advantage of their particular future (very short pulse length, high instantaneous dose rate, narrow beam size etc.) we may be able to develop novel radiotherapy techniques such as microbeams, FLASH techniques etc. The results of this *in silico* study represent a promising start for further scientific work on laser-driven electron source development.

In this work I have also studied some of the properties of the well-known FBX dosimetric solution in terms of sensitivity and dose range. The main motivation was the fact that the success of radiation therapy crucially depends on the accuracy of dose measurements. However, to date, no dosimetric methods have been established for the absolute dosimetry of radiation beams with very high instantaneous dose rates. My effort was to prepare the necessary methodology for future dosimetric measurements in such radiation

fields using a modified version of the Fricke type chemical dosimeter, as an alternative to ionization chambers.

The photometric determination of ferric ions is one of the major obstacle to obtaining good results with low uncertainties. This problem can be eliminated by improving the sensitivity of the solution, which I achieved by increasing the benzoic acid concentration and by adding xylenol orange dye after irradiation. Nonlinearity, a hallmark of an FB system, was eliminated by increasing the ferrous sulphate concentration from the original 0.2 mM value to 1 mM.

For reference irradiation, I constructed a special, multipurpose PMMA slab phantom to hold Eppendorf tubes filled with dosimetric solutions. This phantom can also be used for irradiation under the same conditions as those used for biological and/or chemical samples kept in cell culture dishes or multi-well plates. Moreover, one can perform the cross-calibration of the eFBX dosimeter with other dosimeters, such as films, ionization chambers etc.

Further improvements to the system can be made by studying the influence of temperature on chemical yield and absorbance measurements. If there is indeed a relation between chemical yield and temperature, and between absorbance and temperature, the obtained 1.12 % combined standard uncertainty can be further reduced to 1.0 %.

I am planning to conduct further experiments to make our reference dosimetry system more widely accepted. Our aim is to further optimize and refine the dosimetric characteristics and measurement practices and to ensure the reliability of this system as a reference dosimeter. It is also crucial to prove its suitability in various practical situations, especially in the dosimetry of radiobiological experiments, as well as in radiotherapy measurements. Furthermore, its suitability for measurements of beams with high instantaneous dose rate is still an open question.

New scientific results

1. With PIC simulations I have demonstrated that this laser system can produce quasi-monoenergetic electron beam with high mean kinetic energies (35.97 MeV) at 1 kHz repetition rate which may provide a promising alternative for conventional accelerators;
2. Using Monte Carlo simulations I have demonstrated that this type of 1 kHz LWFA system is capable of generating a sufficient dose rate for practical radiobiological or medical applications (18 Gy/min or even higher);
3. I proved that the operation of LWFA at 1 kHz repetition rate provides precise control over dose delivery (with an estimated uncertainties of 0.3 %);
4. With further developments it is possible to obtain electron beams with depth dose characteristics suitable for real radiotherapy applications (active scanning, microbeams etc.);

5. With proper control of laser and gas target parameters we may be able to perform energy and intensity modulated irradiation, as well as the combination of them even in real time;
6. I have outlined some practical issues and pitfalls which need to be addressed before such systems are used in real applications;
7. I have conducted detailed investigations on the dosimetric properties of the FBX dosimetric solution in terms of sensitivity and dose range;
8. I have improved the precision and accuracy of the dosimeter by increasing the benzoic acid concentration and by adding xylenol orange dye after irradiation;
9. Nonlinearity, a hallmark of an FB system, was eliminated by increasing the ferrous sulphate concentration;
10. I adapt the classical radiochemical model to the new chemical formula which qualitatively explains the enhanced radiochemical yield;
11. For reference irradiation, I constructed a special, multipurpose PMMA slab phantom. This phantom can be used for irradiation under the reference conditions of the dosimetric solution as well as biological or chemical samples in Eppendorf tubes, or for the cross-calibration of our chemical dosimeter with other dosimeters;
12. A standard operational procedure has been established and validated to guarantee the necessary accuracy and precision.

Bibliography

- [1] S. Kühn, M. Dumergue, S. Kahaly, S. Mondal, M. Füle, T. Csizmadia, B. Farkas, B. Major, Z. Várallyay, E. Cormier, M. Kalashnikov, F. Calegari, M. Devetta, F. Frassetto, E. Månsson, L. Poletto, S. Stagira, C. Vozzi, M. Nisoli, P. Rudawski, S. Maclot, F. Campi, H. Wikmark, C. L. Arnold, C. M. Heyl, P. Johnsson, A. L'Huillier, R. Lopez-Martens, S. Haessler, M. Bocoum, F. Boehle, A. Vernier, G. Iaquaniello, E. Skantzakis, N. Papadakis, C. Kalpouzos, P. Tzallas, F. Lépine, D. Charalambidis, K. Varjú, K. Osvay, G. Sansone, The ELI-ALPS facility: the next generation of attosecond sources, *Journal of Physics B: Atomic, Molecular and Optical Physics* 50 (2017) 132002. doi:10.1088/1361-6455/aa6ee8.
- [2] ISO/ASTM51026-15, Standard practice for using the Fricke dosimetry system, ASTM International, 2015. West Conshohocken.
- [3] R. Ramaswami, V. Harding, T. Newsom-Davis, Novel cancer therapies: Treatments driven by tumour biology, *Postgraduate Medical Journal* 89 (2013) 652–658. URL: <https://doi.org/10.1136/postgradmedj-2012-131533>. doi:10.1136/postgradmedj-2012-131533.
- [4] M. Joiner, Basic clinical radiobiology, Hodder Arnold, London, 2009.
- [5] M. Molls, P. Vaupel, C. Nieder, M. Anscher (Eds.), The Impact of Tumor Biology on Cancer Treatment and Multidisciplinary Strategies, Medical Radiology, Springer Berlin Heidelberg, 2009. URL: <https://doi.org/10.1007/978-3-540-74386-6>. doi:10.1007/978-3-540-74386-6.
- [6] P. Symonds, Walter and Miller's textbook of radiotherapy : radiation physics, therapy and oncology, Elsevier Churchill Livingstone, Edinburgh, 2012.
- [7] R. Baskar, K. A. Lee, R. Yeo, K.-W. Yeoh, Cancer and radiation therapy: Current advances and future directions, *International Journal of Medical Sciences* 9 (2012) 193–199. URL: <https://doi.org/10.7150/ijms.3635>. doi:10.7150/ijms.3635.
- [8] Mayles, P. (Ed.), Nahum A. (Ed.), Rosenwald, J. (Ed.). Handbook of Radiotherapy Physics, CRC Press, 2007. doi:10.1201/9781420012026.
- [9] W. J. Meredith, 40 years of development in radiotherapy, *Physics in Medicine and Biology* 29 (1984) 115–120. URL: <https://doi.org/10.1088/0031-9155/29/2/003>. doi:10.1088/0031-9155/29/2/003.

- [10] B. Larsson, B. Larsson, Radiological properties of beams of high-energy protons, *Radiation Research Supplement* 7 (1967) 304. URL: <https://doi.org/10.2307/3583724>. doi:10.2307/3583724.
- [11] C. A. Tobias, J. H. Lawrence, J. L. Born, R. K. McCombs, J. E. Roberts, H. O. Anger, B. V. A. Low-Beer, C. B. Huggins, Pituitary irradiation with high-energy proton beams a preliminary report, *Cancer Research* 18 (1958) 121–134. URL: <https://cancerres.aacrjournals.org/content/18/2/121>. arXiv:<https://cancerres.aacrjournals.org/content/18/2/121.full.pdf>.
- [12] M. Goitein, A. J. Lomax, E. S. Pedroni, Weighing proton therapy’s clinical readiness and costs, *Physics Today* 56 (2003) 13–14. URL: <https://doi.org/10.1063/1.4797049>. doi:10.1063/1.4797049.
- [13] A. M. Allen, T. Pawlicki, L. Dong, E. Fourkal, M. Buyyounouski, K. Cengel, J. Plastaras, M. K. Bucci, T. I. Yock, L. Bonilla, R. Price, E. E. Harris, A. A. Kanski, An evidence based review of proton beam therapy: the report of astro’s emerging technology committee, *Radiotherapy and Oncology* 103 (2012) 8–11. URL: <https://doi.org/10.1016/j.radonc.2012.02.001>. doi:10.1016/j.radonc.2012.02.001.
- [14] Y. Nakagawa, H. Yoshihara, T. Kageji, R. Matsuoka, Y. Nakagawa, Cost analysis of radiotherapy, carbon ion therapy, proton therapy and bncT in Japan, *Applied Radiation and Isotopes* 67 (2009) S80–S83. URL: <https://doi.org/10.1016/j.apradiso.2009.03.055>. doi:10.1016/j.apradiso.2009.03.055.
- [15] K. Ando, Y. Kase, Biological characteristics of carbon-ion therapy, *International Journal of Radiation Biology* 85 (2009) 715–728. URL: <https://doi.org/10.1080/09553000903072470>. doi:10.1080/09553000903072470.
- [16] D. Schardt, Tumor therapy with high-energy carbon ion beams, *Nuclear Physics A* 787 (2007) 633–641. URL: <https://doi.org/10.1016/j.nuclphysa.2006.12.097>. doi:10.1016/j.nuclphysa.2006.12.097.
- [17] M. Durante, S. Yamada, K. Ando, Y. Furusawa, T. Kawata, H. Majima, T. Nakano, H. Tsujii, X-rays vs. carbon-ion tumor therapy: Cytogenetic damage in lymphocytes, *International Journal of Radiation Oncology*Biophysics* 47 (2000) 793–798. URL: [https://doi.org/10.1016/s0360-3016\(00\)00455-7](https://doi.org/10.1016/s0360-3016(00)00455-7). doi:10.1016/s0360-3016(00)00455-7.
- [18] R. R. Wilson, Radiological use of fast protons, *Radiology* 47 (1946) 487–491. URL: <https://doi.org/10.1148/47.5.487>. doi:10.1148/47.5.487.
- [19] R. K. McCombs, Proton irradiation of the pituitary and its metabolic effects, *Radiology* 68 (1957) 797–811. URL: <https://doi.org/10.1148/68.6.797>. doi:10.1148/68.6.797.
- [20] J. Naeslund, S. Sténson, B. Larsson, Results of proton irradiation of VX2 carcinoma in the uterus of rabbits, *Acta Obstetrica et Gynecologica Scandinavica* 38 (1959) 563–585. URL: <https://www.tandfonline.com/>

- doi/abs/10.3109/00016345909153954. doi:10.3109/00016345909153954.
arXiv:<https://www.tandfonline.com/doi/pdf/10.3109/00016345909153954>.
- [21] D. W. Miller, A review of proton beam radiation therapy, *Medical Physics* 22 (1995) 1943–1954. URL: <https://doi.org/10.1118/1.597435>. doi:10.1118/1.597435.
- [22] J. M. Slater, J. O. Archambeau, D. W. Miller, M. I. Notarus, W. Preston, J. D. Slater, The proton treatment center at loma linda university medical center: Rationale for and description of its development, *International Journal of Radiation Oncology*Biophysics* 22 (1992) 383–389. URL: [https://doi.org/10.1016/0360-3016\(92\)90058-p](https://doi.org/10.1016/0360-3016(92)90058-p). doi:10.1016/0360-3016(92)90058-p.
- [23] S. Sawada, J-parc facility, *Nuclear Physics A* 834 (2010) 701c–706c. URL: <https://doi.org/10.1016/j.nuclphysa.2010.01.127>. doi:10.1016/j.nuclphysa.2010.01.127.
- [24] J. M. Schippers, Beam delivery systems for particle radiation therapy: Current status and recent developments, *Reviews of Accelerator Science and Technology* 02 (2009) 179–200. URL: <https://doi.org/10.1142/s1793626809000211>. doi:10.1142/s1793626809000211.
- [25] L. A. Gizzi, C. A. Cecchetti, A. Giulietti, D. Giulietti, P. Koester, L. Labate, T. Levato, N. Pathak, Thomson scattering imaging from ultrashort ultraintense laser interaction with gas, *IEEE Transactions on Plasma Science* 39 (2011) 2954–2955. URL: <https://doi.org/10.1109/tps.2011.2164622>. doi:10.1109/tps.2011.2164622.
- [26] R. H. Milburn, Electron scattering by an intense polarized photon field, *Physical Review Letters* 10 (1963) 75–77. URL: <https://doi.org/10.1103/physrevlett.10.75>. doi:10.1103/physrevlett.10.75.
- [27] C. Bemporad, R. H. Milburn, N. Tanaka, M. Fotino, High-energy photons from compton scattering of light on 6.0-GeV electrons, *Physical Review* 138 (1965) B1546–B1549. URL: <https://doi.org/10.1103/physrev.138.b1546>. doi:10.1103/physrev.138.b1546.
- [28] G. Sarri, D. J. Corvan, W. Schumaker, J. M. Cole, A. D. Piazza, H. Ahmed, C. Harvey, C. H. Keitel, K. Krushelnick, S. P. D. Mangles, Z. Najmudin, D. Symes, A. G. R. Thomas, M. Yeung, Z. Zhao, M. Zepf, Ultrahigh brilliance multi-MeV γ -ray beams from nonlinear relativistic thomson scattering, *Physical Review Letters* 113 (2014) 224801. URL: <https://doi.org/10.1103/physrevlett.113.224801>. doi:10.1103/physrevlett.113.224801.
- [29] C. Liu, G. Golovin, S. Chen, J. Zhang, B. Zhao, D. Haden, S. Banerjee, J. Silano, H. Karwowski, D. Umstadter, Generation of 9 MeV γ -rays by all-laser-driven compton scattering with second-harmonic laser light, *Optics Letters* 39 (2014) 4132. URL: <https://doi.org/10.1364/ol.39.004132>. doi:10.1364/ol.39.004132.

- [30] A. Giulietti, N. Bourgeois, T. Ceccotti, X. Davoine, S. Dobosz, P. D'Oliveira, M. Galimberti, J. Galy, A. Gamucci, D. Giulietti, L. A. Gizzi, D. J. Hamilton, E. Lefebvre, L. Labate, J. R. Marquès, P. Monot, H. Popescu, F. Réau, G. Sarri, P. Tomassini, P. Martin, Intense γ -ray source in the giant-dipole-resonance range driven by 10-TW laser pulses, *Physical Review Letters* 101 (2008) 105002. URL: <https://doi.org/10.1103/physrevlett.101.105002>. doi:10.1103/physrevlett.101.105002.
- [31] A. J. Gonsalves, K. Nakamura, J. Daniels, C. Benedetti, C. Pieronek, T. C. H. de Raadt, S. Steinke, J. H. Bin, S. S. Bulanov, J. van Tilborg, C. G. R. Geddes, C. B. Schroeder, C. Tóth, E. Esarey, K. Swanson, L. Fan-Chiang, G. Bagdasarov, N. Bobrova, V. Gasilov, G. Korn, P. Sasorov, W. P. Leemans, Petawatt laser guiding and electron beam acceleration to 8 GeV in a laser-heated capillary discharge waveguide, *Physical Review Letters* 122 (2019) 084801. URL: <https://doi.org/10.1103/physrevlett.122.084801>. doi:10.1103/physrevlett.122.084801.
- [32] J. B. Rosenzweig, D. B. Cline, B. Cole, H. Figueroa, W. Gai, R. Konecny, J. Norem, P. Schoessow, J. Simpson, Experimental observation of plasma wake-field acceleration, *Physical Review Letters* 61 (1988) 98–101. URL: <https://doi.org/10.1103/physrevlett.61.98>. doi:10.1103/physrevlett.61.98.
- [33] Y. B. Fainberg, V. Balakirev, I. Onishchenko, Wake field excitation in plasma by a train of relativistic electron bunches, *Plasma Physics Reports* 20 (1994) 606–612.
- [34] E. Esarey, P. Sprangle, J. Krall, A. Ting, Overview of plasma-based accelerator concepts, *IEEE Transactions on Plasma Science* 24 (1996) 252–288. URL: <https://doi.org/10.1109/27.509991>. doi:10.1109/27.509991.
- [35] T. Tajima, J. M. Dawson, Laser electron accelerator, *Physical Review Letters* 43 (1979) 267–270. URL: <https://doi.org/10.1103/physrevlett.43.267>. doi:10.1103/physrevlett.43.267.
- [36] Y. Kitagawa, T. Matsumoto, T. Minamihata, K. Sawai, K. Matsuo, K. Mima, K. Nishihara, H. Azechi, K. A. Tanaka, H. Takabe, S. Nakai, Beat-wave excitation of plasma wave and observation of accelerated electrons, *Physical Review Letters* 68 (1992) 48–51. URL: <https://doi.org/10.1103/physrevlett.68.48>. doi:10.1103/physrevlett.68.48.
- [37] M. Everett, A. Lal, D. Gordon, C. E. Clayton, K. A. Marsh, C. Joshi, Trapped electron acceleration by a laser-driven relativistic plasma wave, *Nature* 368 (1994) 527–529. URL: <https://doi.org/10.1038/368527a0>. doi:10.1038/368527a0.
- [38] K. Nakajima, T. Kawakubo, H. Nakanishi, A. Ogata, Y. Kitagawa, R. Kodama, K. Mima, H. Shiraga, K. Suzuki, K. Yamakawa, T. Zhang, Y. Kato, D. Fisher, M. Downer, T. Tajima, Y. Sakawa, T. Shoji, N. Yugami, Y. Nishida, Proof-of-principle experiments of laser wakefield acceleration using a 1ps 10TW Nd:glass laser, in: *AIP Conference Proceedings*, 1995, p. nil. URL: <https://doi.org/10.1063/1.48237>. doi:10.1063/1.48237.

- [39] J. R. Marquès, J. P. Geindre, F. Amiranoff, P. Audebert, J. C. Gauthier, A. Antonetti, G. Grillon, Temporal and spatial measurements of the electron density perturbation produced in the wake of an ultrashort laser pulse, *Physical Review Letters* 76 (1996) 3566–3569. URL: <https://doi.org/10.1103/physrevlett.76.3566>. doi:10.1103/physrevlett.76.3566.
- [40] P. Sprangle, E. Esarey, A. Ting, Nonlinear interaction of intense laser pulses in plasmas, *Physical Review A* 41 (1990) 4463–4469. URL: <https://doi.org/10.1103/physreva.41.4463>. doi:10.1103/physreva.41.4463.
- [41] A. Giulietti (Ed.), *Laser-Driven Particle Acceleration Towards Radiobiology and Medicine*, Biological and Medical Physics, Biomedical Engineering, Springer International Publishing, 2016. URL: <https://doi.org/10.1007/978-3-319-31563-8>. doi:10.1007/978-3-319-31563-8.
- [42] A. Giulietti, G. Bussolino, L. Fulgentini, P. Koester, L. Labate, L. A. Gizzi, *Laser-Plasma Particle Sources for Biology and Medicine*, Progress in Ultrafast Intense Laser Science XII, Springer International Publishing, 2015, pp. 151–178. URL: https://doi.org/10.1007/978-3-319-23657-5_8. doi:10.1007/978-3-319-23657-5_8.
- [43] M. Durante, E. Brauer-Krisch, M. Hill, Faster and safer? FLASH ultra-high dose rate in radiotherapy, *The British Journal of Radiology* 91 (2017) 20170628. URL: <https://doi.org/10.1259/bjr.20170628>. doi:10.1259/bjr.20170628.
- [44] M.-C. Vozenin, J. Hendry, C. Limoli, Biological benefits of ultra-high dose rate FLASH radiotherapy: Sleeping beauty awoken, *Clinical Oncology* 31 (2019) 407–415. URL: <https://doi.org/10.1016/j.clon.2019.04.001>. doi:10.1016/j.clon.2019.04.001.
- [45] A. OGATA, T. KONDOH, J. YANG, A. YOSHIDA, Y. YOSHIDA, LWFA of atto-second and femto-second bunches for pulse radiolysis, *International Journal of Modern Physics B* 21 (2007) 447–458. URL: <https://doi.org/10.1142/s0217979207042239>. doi:10.1142/s0217979207042239.
- [46] M. Bazalova-Carter, B. Qu, B. Palma, B. Hårdemark, E. Hynning, C. Jensen, P. G. Maxim, B. W. Loo, Treatment planning for radiotherapy with very high-energy electron beams and comparison of VHEE and VMAT plans: Treatment planning for VHEE radiotherapy, *Medical Physics* 42 (2015) 2615–2625. doi:10.1118/1.4918923.
- [47] C. DesRosiers, V. Moskvina, M. Cao, C. J. Joshi, M. Langer, Laser-plasma generated very high energy electrons in radiation therapy of the prostate, *Proc. of SPIE* 6881 (2008) 688109. doi:10.1117/12.761663.
- [48] E. Schueler, K. Eriksson, E. Hynning, B. Loo, P. Maxim, TU-H-BRC-03: Evaluation of Very High-Energy Electron (VHEE) Beams in Comparison to VMAT and PBS Treatment Plans, *Medical Physics* 43 (2016) 3766–3766. doi:10.1118/1.4957610.

- [49] B. Palma, M. Bazalova-Carter, B. Hårdemark, E. Hynning, B. Qu, B. W. Loo, P. G. Maxim, Assessment of the quality of very high-energy electron radiotherapy planning, *Radiotherapy and Oncology* 119 (2016) 154–158. doi:10.1016/j.radonc.2016.01.017.
- [50] C. DesRosiers, V. Moskvina, A. F. Bielajew, L. Papiez, 150-250 MeV electron beams in radiation therapy, *Physics in Medicine and Biology* 45 (2000) 1781–1805. URL: <https://doi.org/10.1088/0031-9155/45/7/306>. doi:10.1088/0031-9155/45/7/306.
- [51] M. Bazalova-Carter, M. Liu, B. Palma, M. Dunning, D. McCormick, E. Hemsing, J. Nelson, K. Jobe, E. Colby, A. C. Koong, S. Tantawi, V. Dolgashev, P. G. Maxim, B. W. Loo, Comparison of film measurements and monte carlo simulations of dose delivered with very high-energy electron beams in a polystyrene phantom, *Medical Physics* 42 (2015) 1606–1613. URL: <https://doi.org/10.1118/1.4914371>. doi:10.1118/1.4914371.
- [52] K. Kokurewicz, E. Brunetti, G. H. Welsh, S. M. Wiggins, M. Boyd, A. Sorensen, A. J. Chalmers, G. Schettino, A. Subiel, C. DesRosiers, D. A. Jaroszynski, Focused very high-energy electron beams as a novel radiotherapy modality for producing high-dose volumetric elements, *Scientific Reports* 9 (2019) 10837. URL: <https://doi.org/10.1038/s41598-019-46630-w>. doi:10.1038/s41598-019-46630-w.
- [53] B. W. Loo, P. G. Maxim, V. A. Dolgashev, *Pluridirectional very high electron energy radiation therapy systems and processes*, 2013.
- [54] V. Malka, J. Faure, Y. Glinec, C. Rechatin, Principle and applications of electron beams produced with laser plasma accelerators, in: *Journal of Physics: Conference Series*, volume 112, IOP Publishing, 2008, p. 042029. doi:10.1088/1742-6596/112/4/042029.
- [55] K. Schmid, *Laser Wakefield Electron Acceleration*, 1 ed., Springer-Verlag Berlin Heidelberg, 2011. doi:10.1007/978-3-642-19950-9.
- [56] J. Faure, Y. Glinec, A. Pukhov, S. Kiselev, S. Gordienko, E. Lefebvre, J.-P. Rousseau, F. Burgy, V. Malka, A laser-plasma accelerator producing monoenergetic electron beams, *Nature* 431 (2004) 541–544. doi:10.1038/nature02963.
- [57] C. G. R. Geddes, C. Toth, J. v. Tilborg, E. Esarey, C. B. Schroeder, D. Bruhwiler, C. Nieter, J. Cary, W. P. Leemans, High-quality electron beams from a laser wakefield accelerator using plasma-channel guiding, *Nature* 431 (2004) 538. doi:10.1038/nature02900.
- [58] S. P. D. Mangles, C. D. Murphy, Z. Najmudin, A. G. R. Thomas, J. L. Collier, A. E. Dangor, E. J. Divall, P. S. Foster, J. G. Gallacher, C. J. Hooker, D. A. Jaroszynski, A. J. Langley, W. B. Mori, P. A. Norreys, F. S. Tsung, R. Viskup, B. R. Walton, K. Krushelnick, Monoenergetic beams of relativistic electrons from intense laser-plasma interactions, *Nature* 431 (2004) 535–538. doi:10.1038/nature02939.

- [59] W. P. Leemans, A. J. Gonsalves, H.-S. Mao, K. Nakamura, C. Benedetti, C. B. Schroeder, C. Tóth, J. Daniels, D. E. Mittelberger, S. S. Bulanov, J.-L. Vay, C. G. R. Geddes, E. Esarey, Multi-GeV electron beams from capillary-discharge-guided sub-petawatt laser pulses in the self-trapping regime, *Physical Review Letters* 113 (2014) 245002. doi:10.1103/PhysRevLett.113.245002.
- [60] E. Beyreuther, W. Enghardt, M. Kaluza, L. Karsch, L. Laschinsky, E. Lessmann, M. Nicolai, J. Pawelke, C. Richter, R. Sauerbrey, H.-P. Schlenvoigt, M. Baumann, Establishment of technical prerequisites for cell irradiation experiments with laser-accelerated electrons: Laser-accelerated electrons for cell irradiation experiments, *Medical Physics* 37 (2010) 1392–1400. doi:10.1118/1.3301598.
- [61] L. Laschinsky, M. Baumann, E. Beyreuther, W. Enghardt, M. Kaluza, L. Karsch, E. Lessmann, D. Naumburger, M. Nicolai, C. Richter, R. Sauerbrey, H.-P. Schlenvoigt, J. Pawelke, Radiobiological Effectiveness of Laser Accelerated Electrons in Comparison to Electron Beams from a Conventional Linear Accelerator, *Journal of Radiation Research* 53 (2012) 395–403. doi:10.1269/jrr.11080.
- [62] A. Subiel, V. Moskvin, G. H. Welsh, S. Cipiccia, D. Reboredo, C. DesRosiers, D. A. Jaroszynski, Challenges of dosimetry of ultra-short pulsed very high energy electron beams, *Physica Medica* 42 (2017) 327–331. URL: <https://doi.org/10.1016/j.ejmp.2017.04.029>. doi:10.1016/j.ejmp.2017.04.029.
- [63] D. Alesini, S. Bertolucci, M. Biagini, C. Biscari, R. Boni, M. Boscolo, M. Castellano, A. Clozza, G. D. Pirro, A. Drago, A. Esposito, M. Ferrario, V. Fusco, A. Gallo, A. Ghigo, S. Guiducci, M. Incurvati, P. Laurelli, C. Ligi, F. Marcellini, M. Migliorati, C. Milardi, L. Palumbo, L. Pellegrino, M. Preger, P. Raimondi, R. Ricci, C. Sanelli, F. Sgamma, B. Spataro, M. Serio, A. Stecchi, A. Stella, F. Tazzioli, C. Vaccarezza, M. Vescovi, C. Vicario, M. Zobov, E. Acerbi, F. Alessandria, D. Barni, G. Bellomo, I. Boscolo, F. Broggi, S. Cialdi, C. DeMartinis, D. Giove, C. Maroli, V. Petrillo, M. Rome', L. Serafini, E. Chiadroni, G. Felici, D. Levi, M. Mastrucci, M. Mattioli, G. Medici, G. Petrarca, L. Catani, A. Cianchi, A. D'Angelo, R. D. Salvo, A. Fantini, D. Moricciani, C. Schaerf, R. Bartolini, F. Ciocci, G. Dattoli, A. Doria, F. Flora, G. Gallerano, L. Giannessi, E. Giovenale, G. Messina, L. Mezi, P. Ottaviani, L. Picardi, M. Quattromini, A. Renieri, C. Ronsivalle, L. Avaldi, C. Carbone, A. Cricenti, A. Pifferi, P. Perfetti, T. Prospero, V. Albertini, C. Quaresima, N. Zema, The sparco project: a high-brightness electron beam source at LNF to drive a SASE-FEL experiment, *Nuclear Instruments and Methods in Physics Research Section A: Accelerators, Spectrometers, Detectors and Associated Equipment* 507 (2003) 345–349. URL: [https://doi.org/10.1016/s0168-9002\(03\)00943-4](https://doi.org/10.1016/s0168-9002(03)00943-4). doi:10.1016/s0168-9002(03)00943-4.
- [64] M. McManus, F. Romano, N. D. Lee, W. Farabolini, A. Gilardi, G. Royle, H. Palmans, A. Subiel, The challenge of ionisation chamber dosimetry in ultra-short pulsed high dose-rate very high energy electron beams, *Scientific Reports* 10 (2020) 9089. URL: <https://doi.org/10.1038/s41598-020-65819-y>. doi:10.1038/s41598-020-65819-y.

- [65] A. R. Maier, N. M. Delbos, T. Eichner, L. Hübner, S. Jalas, L. Jeppe, S. W. Jolly, M. Kirchen, V. Leroux, P. Messner, M. Schnepf, M. Trunk, P. A. Walker, C. Werle, P. Winkler, Decoding sources of energy variability in a laser-plasma accelerator, *Physical Review X* in press (2020).
- [66] N. A. M. Hafz, T. M. Jeong, I. W. Choi, S. K. Lee, K. H. Pae, V. V. Kulagin, J. H. Sung, T. J. Yu, K.-H. Hong, T. Hosokai, J. R. Cary, D.-K. Ko, J. Lee, Stable generation of GeV-class electron beams from self-guided laser-plasma channels, *Nature Photonics* 2 (2008) 571–577. URL: <https://doi.org/10.1038/nphoton.2008.155>. doi:10.1038/nphoton.2008.155.
- [67] S. S. Bulanov, A. Brantov, V. Y. Bychenkov, V. Chvykov, G. Kalinchenko, T. Mat-suoka, P. Rousseau, S. Reed, V. Yanovsky, K. Krushelnick, D. W. Litzenberg, A. Maksimchuk, Accelerating protons to therapeutic energies with ultraintense, ultraclean, and ultrashort laser pulses, *Medical Physics* 35 (2008) 1770–1776. URL: <https://doi.org/10.1118/1.2900112>. doi:10.1118/1.2900112.
- [68] K. Zeil, M. Baumann, E. Beyreuther, T. Burris-Mog, T. E. Cowan, W. Enghardt, L. Karsch, S. D. Kraft, L. Laschinsky, J. Metzkes, D. Naumburger, M. Oppelt, C. Richter, R. Sauerbrey, M. Schürer, U. Schramm, J. Pawelke, Dose-controlled irradiation of cancer cells with laser-accelerated proton pulses, *Applied Physics B* 110 (2012) 437–444. URL: <https://doi.org/10.1007/s00340-012-5275-3>. doi:10.1007/s00340-012-5275-3.
- [69] E. Beyreuther, W. Enghardt, M. Kaluza, L. Karsch, L. Laschinsky, E. Lessmann, M. Nicolai, J. Pawelke, C. Richter, R. Sauerbrey, H.-P. Schlenvoigt, M. Baumann, Establishment of technical prerequisites for cell irradiation experiments with laser-accelerated electrons, *Medical Physics* 37 (2010) 1392–1400. URL: <https://doi.org/10.1118/1.3301598>. doi:10.1118/1.3301598.
- [70] S. D. Kraft, C. Richter, K. Zeil, M. Baumann, E. Beyreuther, S. Bock, M. Bussmann, T. E. Cowan, Y. Dammene, W. Enghardt, U. Helbig, L. Karsch, T. Kluge, L. Laschinsky, E. Lessmann, J. Metzkes, D. Naumburger, R. Sauerbrey, M. Schürer, M. Sobiella, J. Woithe, U. Schramm, J. Pawelke, Dose-dependent biological damage of tumour cells by laser-accelerated proton beams, *New Journal of Physics* 12 (2010) 085003. URL: <https://doi.org/10.1088/1367-2630/12/8/085003>. doi:10.1088/1367-2630/12/8/085003.
- [71] A. Yogo, T. Maeda, T. Hori, H. Sakaki, K. Ogura, M. Nishiuchi, A. Sagisaka, H. Kiriya, H. Okada, S. Kanazawa, T. Shimomura, Y. Nakai, M. Tanoue, F. Sasao, P. R. Bolton, M. Murakami, T. Nomura, S. Kawanishi, K. Kondo, Measurement of relative biological effectiveness of protons in human cancer cells using a laser-driven quasimonoenergetic proton beamline, *Applied Physics Letters* 98 (2011) 053701. URL: <https://doi.org/10.1063/1.3551623>. doi:10.1063/1.3551623.
- [72] L. Laschinsky, M. Baumann, E. Beyreuther, W. Enghardt, M. Kaluza, L. Karsch, E. Lessmann, D. Naumburger, M. Nicolai, C. Richter, R. Sauerbrey, H.-P. Schlenvoigt, J. Pawelke, Radiobiological effectiveness of laser accelerated electrons in

- comparison to electron beams from a conventional linear accelerator, *Journal of Radiation Research* 53 (2012) 395–403. URL: <https://doi.org/10.1269/jrr.11080>. doi:10.1269/jrr.11080.
- [73] D. Doria, K. F. Kakolee, S. Kar, S. K. Litt, F. Fiorini, H. Ahmed, S. Green, J. C. G. Jeynes, J. Kavanagh, D. Kirby, K. J. Kirkby, C. L. Lewis, M. J. Merchant, G. Nersisyan, R. Prasad, K. M. Prise, G. Schettino, M. Zepf, M. Borghesi, Biological effectiveness on live cells of laser driven protons at dose rates exceeding 109Gy/s, *AIP Advances* 2 (2012) 011209. URL: <https://doi.org/10.1063/1.3699063>. doi:10.1063/1.3699063.
- [74] Y. A. Gauduel, S. Fritzler, A. Hallou, Y. Glinec, V. Malka, Femtosecond relativistic electron beam triggered early bioradical events, in: *Femtosecond Laser Applications in Biology*, 2004, p. nil. URL: <https://doi.org/10.1117/12.545408>. doi:10.1117/12.545408.
- [75] V. Malka, J. Faure, Y. A. Gauduel, Ultra-short electron beams based spatiotemporal radiation biology and radiotherapy, *Mutation Research/Reviews in Mutation Research* 704 (2010) 142–151. URL: <https://doi.org/10.1016/j.mrrev.2010.01.006>. doi:10.1016/j.mrrev.2010.01.006.
- [76] A. Giulietti, M. G. Andreassi, C. Greco, Pulsed radiobiology with laser-driven plasma accelerators, in: *Laser Acceleration of Electrons, Protons, and Ions; and Medical Applications of Laser-Generated Secondary Sources of Radiation and Particles*, 2011, p. nil. URL: <https://doi.org/10.1117/12.888736>. doi:10.1117/12.888736.
- [77] M. Kawaguchi, K. Ushida, S. Kashiwagi, R. Kuroda, T. Kuribayashi, M. Kobayashi, Y. Hama, M. Washio, Development of compact picosecond pulse radiolysis system, *Nuclear Instruments and Methods in Physics Research Section B: Beam Interactions with Materials and Atoms* 236 (2005) 425–431. URL: <https://doi.org/10.1016/j.nimb.2005.04.012>. doi:10.1016/j.nimb.2005.04.012.
- [78] W. C. Röntgen, Ueber eine neue art von strahlen, *Annalen der Physik* 300 (1898) 12–17. URL: <https://doi.org/10.1002/andp.18983000103>. doi:10.1002/andp.18983000103.
- [79] E. H. Grubbé, Priority in the therapeutic use of x-rays, *Radiology* 21 (1933) 156–162. URL: <https://doi.org/10.1148/21.2.156>. doi:10.1148/21.2.156.
- [80] R. Mould, Pierre curie 1859-1906, *Current Oncology* 14 (2007) 74–82. URL: <https://doi.org/10.3747/co.2007.110>. doi:10.3747/co.2007.110.
- [81] M. Lederman, The early history of radiotherapy: 1895-1939, *International Journal of Radiation Oncology*Biophysics* 7 (1981) 639–648. URL: [https://doi.org/10.1016/0360-3016\(81\)90379-5](https://doi.org/10.1016/0360-3016(81)90379-5). doi:10.1016/0360-3016(81)90379-5.

- [82] H. Coutard, Principles of x ray therapy of malignant diseases, *The Lancet* 224 (1934) 1–8. URL: [https://doi.org/10.1016/s0140-6736\(00\)90085-0](https://doi.org/10.1016/s0140-6736(00)90085-0). doi:10.1016/s0140-6736(00)90085-0.
- [83] R. Wideröe, Über ein neues prinzip zur herstellung hoher spannungen, *Archiv für Elektrotechnik* 21 (1928) 387–406. URL: <https://doi.org/10.1007/bf01656341>. doi:10.1007/bf01656341.
- [84] C. J. Karzmark, N. C. Pering, Electron linear accelerators for radiation therapy: History, principles and contemporary developments, *Physics in Medicine and Biology* 18 (1973) 321–354. URL: <https://doi.org/10.1088/0031-9155/18/3/001>. doi:10.1088/0031-9155/18/3/001.
- [85] P. Howard-Flanders, The development of the linear accelerator as a clinical instrument, *Acta Radiologica* 41 (1954) 649–655. URL: <https://doi.org/10.3109/00016925409177244>. doi:10.3109/00016925409177244.
- [86] D. I. Thwaites, J. B. Tuohy, Back to the future: the history and development of the clinical linear accelerator, *Physics in Medicine and Biology* 51 (2006) R343–R362. URL: <https://doi.org/10.1088/0031-9155/51/13/r20>. doi:10.1088/0031-9155/51/13/r20.
- [87] F. Ellis, E. J. Hall, R. Oliver, A compensator for variations in tissue thickness for high energy beams, *The British Journal of Radiology* 32 (1959) 421–422. URL: <https://doi.org/10.1259/0007-1285-32-378-421>. doi:10.1259/0007-1285-32-378-421.
- [88] V. Veksler, Proceedings of the CERN symposium on high-energy accelerators and pion physics, 1956.
- [89] H. Hamster, A. Sullivan, S. Gordon, W. White, R. W. Falcone, Subpicosecond, electromagnetic pulses from intense laser-plasma interaction, *Physical Review Letters* 71 (1993) 2725–2728. URL: <https://doi.org/10.1103/physrevlett.71.2725>. doi:10.1103/physrevlett.71.2725.
- [90] J. Wenz, A. Döpp, K. Khrennikov, S. Schindler, M. F. Gilljohann, H. Ding, J. Götzfried, A. Buck, J. Xu, M. Heigoldt, W. Helml, L. Veisz, S. Karsch, Dual-energy electron beams from a compact laser-driven accelerator, *Nature Photonics* 13 (2019) 263–269. URL: <https://doi.org/10.1038/s41566-019-0356-z>. doi:10.1038/s41566-019-0356-z.
- [91] S. Li, G. Li, Q. Ain, M. S. Hur, A. C. Ting, V. V. Kulagin, C. Kamperidis, N. A. M. Hafz, A laser-plasma accelerator driven by two-color relativistic femtosecond laser pulses, *Science Advances* 5 (2019) eaav7940. URL: <https://doi.org/10.1126/sciadv.aav7940>. doi:10.1126/sciadv.aav7940.
- [92] R. Budriūnas, T. Stanislauskas, J. Adamonis, A. Aleknavičius, G. Veitas, D. Gadonas, S. Balickas, A. Michailovas, A. Varanavičius, 53 W average power cep-stabilized opcpa system delivering 55 TW few cycle pulses at 1 khz repetition rate,

- Optics Express 25 (2017) 5797. URL: <https://doi.org/10.1364/oe.25.005797>. doi:10.1364/oe.25.005797.
- [93] Report 24, Journal of the International Commission on Radiation Units and Measurements os13 (2016) NP–NP. URL: <https://doi.org/10.1093/jicru/os13.1.Report24>. doi:10.1093/jicru/os13.1.Report24.
- [94] International Atomic Energy Agency, Calibration of Reference Dosimeters for External Beam Radiotherapy., International Atomic Energy Agency, 2009. OCLC: 463338844.
- [95] Absorbed Dose Determination in External Beam Radiotherapy, Technical Reports Series number 398, International Atomic Energy Agency, Vienna, 2001. URL: <https://www.iaea.org/publications/5954/absorbed-dose-determination-in-external-beam-radiotherapy>.
- [96] J. G. P. Peixoto, P. Andreo, Determination of absorbed dose to water in reference conditions for radiotherapy kilovoltage x-rays between 10 and 300 kV: a comparison of the data in the iaea, ipemb, din and ncs dosimetry protocols, Physics in Medicine and Biology 45 (2000) 563–575. URL: <https://doi.org/10.1088/0031-9155/45/3/301>. doi:10.1088/0031-9155/45/3/301.
- [97] P. R. Almond, P. J. Biggs, B. M. Coursey, W. Hanson, M. S. Huq, R. Nath, D. Rogers, Aapm’s TG-51 protocol for clinical reference dosimetry of high-energy photon and electron beams, Medical physics 26 (1999) 1847–1870.
- [98] F. Attix, Introduction to radiological physics and radiation dosimetry, Wiley, New York, 1986.
- [99] L. H. Gray, The absorption of penetrating radiation, Proceedings of the Royal Society of London. Series A, Containing Papers of a Mathematical and Physical Character 122 (1929) 647–668. URL: <https://doi.org/10.1098/rspa.1929.0050>. doi:10.1098/rspa.1929.0050.
- [100] L. H. Gray, An ionization method for the absolute measurement of γ -ray energy, Health Physics 38 (1980) 907–918. URL: <https://doi.org/10.1097/00004032-198006000-00004>. doi:10.1097/00004032-198006000-00004.
- [101] L. V. Spencer, F. H. Attix, A theory of cavity ionization, Radiation Research 3 (1955) 239. URL: <https://doi.org/10.2307/3570326>. doi:10.2307/3570326.
- [102] T. E. Burlin, A general theory of cavity ionisation, The British Journal of Radiology 39 (1966) 727–734. URL: <https://doi.org/10.1259/0007-1285-39-466-727>. doi:10.1259/0007-1285-39-466-727.
- [103] A. Montelius, B. Jung, ICRU report 64. dosimetry of high-energy photon beams based on standards of absorbed dose to water J. ICRU vol. 1, 1 (2001)., Acta Radiologica 43 (2002) 631–631. URL: <https://doi.org/10.1034/j.1600-0455.2002.4306211.x>. doi:10.1034/j.1600-0455.2002.4306211.x.

- [104] M. Boutillon, A. M. Perroche, Ionometric determination of absorbed dose to water for Cobalt-60 gamma rays, *Physics in Medicine and Biology* 38 (1993) 439–454. URL: <https://doi.org/10.1088/0031-9155/38/3/010>. doi:10.1088/0031-9155/38/3/010.
- [105] H. Feist, Determination of the absorbed dose to water for high-energy photons and electrons by total absorption of electrons in ferrous sulphate solution, *Physics in Medicine and Biology* 27 (1982) 1435–1447. URL: <https://doi.org/10.1088/0031-9155/27/12/002>. doi:10.1088/0031-9155/27/12/002.
- [106] S. R. Domen, A sealed water calorimeter for measuring absorbed dose, *Journal Of Research-National Institute Of Standards And Technology* 99 (1994) 121–121.
- [107] N. V. Klassen, C. K. Ross, Water calorimetry: the heat defect, *Journal of research of the National Institute of Standards and Technology* 102 (1997) 63.
- [108] K. Shortt, N. Klassen, C. Ross, G. Smith, Ferrous sulphate dosimetry and its role in establishing an absorbed dose to water standard for the national research council of canada, in: *Workshop on Water Calorimetry (Report NRC-29637)*(Ross, CK, Klassen, NV, ed.), NRC, Ottawa, Canada, 1988, pp. 121–126.
- [109] M. Boutillon, B. M. Coursey, K. Hohlfeld, B. Owen, D. Rogers, Comparison of primary water absorbed dose standards, in: *Measurement assurance in dosimetry*, 1994.
- [110] M. Boutillon, P. Andreo, Some thoughts on the dissemination of $N_{d,w}$ calibration factors in Co-60 gamma radiation, *Report CCEMRI (I)/97-1*, BIPM, Pavillon de Breteuil, F-92312 Sevres (1997).
- [111] K. Hohlfeld, P. Andreo, O. Mattsson, J. P. Simoen, Comparison of primary absorbed-dose standards, *Journal of the International Commission on Radiation Units and Measurements* 1 (2001) 51–55. URL: <https://doi.org/10.1093/jicru/1.1.51>. doi:10.1093/jicru/1.1.51.
- [112] J. Boag, E. Hochhäuser, O. Balk, The effect of free-electron collection on the recombination correction to ionization measurements of pulsed radiation, *Physics in Medicine & Biology* 41 (1996) 885.
- [113] M. Nicolai, A. Sävert, M. Reuter, M. Schnell, J. Polz, O. Jäckel, L. Karsch, M. Schürer, M. Oppelt, J. Pawelke, M. C. Kaluza, Realizing a laser-driven electron source applicable for radiobiological tumor irradiation, *Applied Physics B* 116 (2013) 643–651. URL: <https://doi.org/10.1007/s00340-013-5747-0>. doi:10.1007/s00340-013-5747-0.
- [114] C. E. Sosolik, A. C. Lavery, E. B. Dahl, B. H. Cooper, A technique for accurate measurements of ion beam current density using a faraday cup, *Review of Scientific Instruments* 71 (2000) 3326–3330. URL: <https://doi.org/10.1063/1.1287635>. doi:10.1063/1.1287635.

- [115] S. Neff, S. Wright, J. Ford, R. Royle, R. Presura, Faraday cup measurements of the energy spectrum of laser-accelerated protons, *IEEE Transactions on Plasma Science* 36 (2008) 2775–2779. URL: <https://doi.org/10.1109/tps.2008.2002204>. doi:10.1109/tps.2008.2002204.
- [116] M. GHERGHEREHCHI, H. AFARIDEH, M. GHANNADI, A. MOHAMMADZADEH, G. R. ASLANI, B. BOGHRATI, Proton beam dosimetry: a comparison between a plastic scintillator, ionization chamber and faraday cup, *Journal of Radiation Research* 51 (2010) 423–430. URL: <https://doi.org/10.1269/jrr.09121>. doi:10.1269/jrr.09121.
- [117] D. Margarone, J. Krása, L. Giuffrida, A. Picciotto, L. Torrisi, T. Nowak, P. Musumeci, A. Velyhan, J. Prokůpek, L. Láska, T. Mocek, J. Ullschmied, B. Rus, Full characterization of laser-accelerated ion beams using faraday cup, silicon carbide, and single-crystal diamond detectors, *Journal of Applied Physics* 109 (2011) 103302. URL: <https://doi.org/10.1063/1.3585871>. doi:10.1063/1.3585871.
- [118] L. Karsch, E. Beyreuther, T. Burris-Mog, S. Kraft, C. Richter, K. Zeil, J. Pawelke, Dose rate dependence for different dosimeters and detectors: Tld, osl, ebt films, and diamond detectors, *Medical Physics* 39 (2012) 2447–2455. URL: <https://doi.org/10.1118/1.3700400>. doi:10.1118/1.3700400.
- [119] C. Fiandra, U. Ricardi, R. Ragona, S. Anglesio, F. R. Giglioli, E. Calamia, F. Lucio, Clinical use of ebt model gafchromic™ film in radiotherapy, *Medical Physics* 33 (2006) 4314–4319. URL: <https://doi.org/10.1118/1.2362876>. doi:10.1118/1.2362876.
- [120] C. Fiandra, R. Ragona, U. Ricardi, S. Anglesio, F. R. Giglioli, Absolute and relative dose measurements with gafchromic™ ebt film for high energy electron beams with different doses per pulse, *Medical Physics* 35 (2008) 5463–5470. URL: <https://doi.org/10.1118/1.3005975>. doi:10.1118/1.3005975.
- [121] S. Park, J. Kwak, M. Yoon, D. Shin, S. Lee, K. Cho, S. Kang, K. Kim, H. Bae, S. Park, Dose verification of proton beam therapy using the gafchromic ebt film, *Radiation Measurements* 46 (2011) 717–721. URL: <https://doi.org/10.1016/j.radmeas.2011.06.027>. doi:10.1016/j.radmeas.2011.06.027.
- [122] A. L. Palmer, P. D. Pietro, S. Alobaidli, F. Issa, S. Doran, D. Bradley, A. Nisbet, Comparison of methods for the measurement of radiation dose distributions in high dose rate (HDR) brachytherapy: Ge-doped optical fiber, ebt3 gafchromic film, and presage® radiochromic plastic, *Medical Physics* 40 (2013) 061707. URL: <https://doi.org/10.1118/1.4805100>. doi:10.1118/1.4805100.
- [123] M. Jaccard, K. Petersson, T. Buchillier, J.-F. Germond, M. T. Durán, M.-C. Vozenin, J. Bourhis, F. O. Bochud, C. Bailat, High dose-per-pulse electron beam dosimetry: Usability and dose-rate independence of ebt3 gafchromic films, *Medical Physics* 44 (2017) 725–735. URL: <https://doi.org/10.1002/mp.12066>. doi:10.1002/mp.12066.

- [124] B. Arjomandy, R. Taylor, A. Anand, N. Sahoo, M. Gillin, K. Prado, M. Vivic, Energy dependence and dose response of gafchromic EBT2 film over a wide range of photon, electron, and proton beam energies, *Medical Physics* 37 (2010) 1942–1947. URL: <https://doi.org/10.1118/1.3373523>. doi:10.1118/1.3373523.
- [125] G. Massillon-JL, S.-T. Chiu-Tsao, I. Domingo-Munoz, M. F. Chan, Energy dependence of the new gafchromic EBT3 film:dose response curves for 50 Kv, 6 and 15 MV x-ray beams, *International Journal of Medical Physics, Clinical Engineering and Radiation Oncology* 01 (2012) 60–65. URL: <https://doi.org/10.4236/ijmpcero.2012.12008>. doi:10.4236/ijmpcero.2012.12008.
- [126] T. Cheung, M. J. Butson, P. K. Yu, Independence of calibration curves for EBT gafchromic films of the size of high-energy x-ray fields, *Applied Radiation and Isotopes* 64 (2006) 1027–1030. URL: <https://doi.org/10.1016/j.apradiso.2006.04.006>. doi:10.1016/j.apradiso.2006.04.006.
- [127] D. Guénot, D. Gustas, A. Vernier, B. Beaurepaire, F. Böhle, M. Bocoum, M. Lozano, A. Jullien, R. Lopez-Martens, A. Lifschitz, J. Faure, Relativistic electron beams driven by kHz single-cycle light pulses, *Nature Photonics* 11 (2017) 293–296. URL: <https://doi.org/10.1038/nphoton.2017.46>. doi:10.1038/nphoton.2017.46.
- [128] M. Ouillé, A. Vernier, F. Böhle, M. Bocoum, A. Jullien, M. Lozano, J.-P. Rousseau, Z. Cheng, D. Gustas, A. Blumenstein, P. Simon, S. Haessler, J. Faure, T. Nagy, R. Lopez-Martens, Relativistic-intensity near-single-cycle light waveforms at kHz repetition rate, *Light: Science & Applications* 9 (2020) 47. URL: <https://doi.org/10.1038/s41377-020-0280-5>. doi:10.1038/s41377-020-0280-5.
- [129] K. R. Hogstrom, P. R. Almond, Review of electron beam therapy physics, *Physics in Medicine and Biology* 51 (2006) R455–R489. URL: <https://doi.org/10.1088/0031-9155/51/13/r25>. doi:10.1088/0031-9155/51/13/r25.
- [130] K. R. Hogstrom, M. D. Mills, P. R. Almond, Electron beam dose calculations, *Physics in Medicine and Biology* 26 (1981) 445–459. URL: <https://doi.org/10.1088/0031-9155/26/3/008>. doi:10.1088/0031-9155/26/3/008.
- [131] H. Svensson, P. Almond, A. Brahme, A. Dutreix, H. K. Leetz, Report 35, *Journal of the International Commission on Radiation Units and Measurements* OS18 (1984) NP–NP. URL: <http://dx.doi.org/10.1093/jicru/os18.2.Report35>. doi:10.1093/jicru/os18.2.report35.
- [132] P. Mayles, A. Nahum, J. Rosenwald, *Handbook of Radiotherapy Physics: Theory and Practice*, CRC Press, 2007.
- [133] S. N. A. Laboratory, Next linear collider test accelerator, URL: https://portal.slac.stanford.edu/sites/ard_public/facet/newnav/Pages/tf/nlcta/whatis.aspx.

- [134] J. D. Wilson, E. M. Hammond, G. S. Higgins, K. Petersson, Ultra-high dose rate (FLASH) radiotherapy: Silver bullet or fool's gold?, *Frontiers in Oncology* 9 (2020) nil. URL: <https://doi.org/10.3389/fonc.2019.01563>. doi:10.3389/fonc.2019.01563.
- [135] O. Lundh, J. Lim, C. Rechatin, L. Ammoura, A. Ben-Ismaïl, X. Davoine, G. Gallot, J.-P. Goddet, E. Lefebvre, V. Malka, J. Faure, Few femtosecond, few kiloampere electron bunch produced by a laser-plasma accelerator, *Nature Physics* 7 (2011) 219–222. URL: <https://doi.org/10.1038/nphys1872>. doi:10.1038/nphys1872.
- [136] R. Budriūnas, T. Stanislauskas, J. Adamonis, A. Aleknavičius, G. Veitas, D. Gadonas, S. Balickas, A. Michailovas, A. Varanavičius, 53 W average power CEP-stabilized OPCPA system delivering 55 TW few cycle pulses at 1 kHz repetition rate, *Optics Express* 25 (2017) 5797. doi:10.1364/OE.25.005797.
- [137] F. Böhle, M. Kretschmar, A. Jullien, M. Kovacs, M. Miranda, R. Romero, H. Crespo, U. Morgner, P. Simon, R. Lopez-Martens, T. Nagy, Compression of CEP-stable multi-mJ laser pulses down to 4fs in long hollow fibers, *Laser Physics Letters* 11 (2014) 095401. doi:0.1088/1612-2011/11/9/095401.
- [138] S. Agostinelli, J. Allison, K. Amako, J. Apostolakis, H. Araujo, P. Arce, M. Asai, D. Axen, S. Banerjee, G. Barrand, F. Behner, L. Bellagamba, J. Boudreau, L. Broglia, A. Brunengo, H. Burkhardt, S. Chauvie, J. Chuma, R. Chytraccek, G. Cooperman, G. Cosmo, P. Degtyarenko, A. Dell'Acqua, G. Depaola, D. Dietrich, R. Enami, A. Feliciello, C. Ferguson, H. Fesefeldt, G. Folger, F. Foppiano, A. Forti, S. Garelli, S. Giani, R. Giannitrapani, D. Gibin, J. G. Cadenas, I. González, G. G. Abril, G. Greeniaus, W. Greiner, V. Grichine, A. Grossheim, S. Guatelli, P. Gumplinger, R. Hamatsu, K. Hashimoto, H. Hasui, A. Heikkinen, A. Howard, V. Ivanchenko, A. Johnson, F. Jones, J. Kallenbach, N. Kanaya, M. Kawabata, Y. Kawabata, M. Kawaguti, S. Kelner, P. Kent, A. Kimura, T. Kodama, R. Kokoulin, M. Kossov, H. Kurashige, E. Lamanna, T. Lampén, V. Lara, V. Lefebure, F. Lei, M. Liendl, W. Lockman, F. Longo, S. Magni, M. Maire, E. Medernach, K. Minamimoto, P. M. de Freitas, Y. Morita, K. Murakami, M. Nagamatu, R. Nartallo, P. Nieminen, T. Nishimura, K. Ohtsubo, M. Okamura, S. O'Neale, Y. Oohata, K. Paech, J. Perl, A. Pfeiffer, M. Pia, F. Ranjard, A. Rybin, S. Sadilov, E. D. Salvo, G. Santin, T. Sasaki, N. Savvas, Y. Sawada, S. Scherer, S. Sei, V. Sirotenko, D. Smith, N. Starkov, H. Stoecker, J. Sulkimo, M. Takahata, S. Tanaka, E. Tcherniaev, E. S. Tehrani, M. Tropeano, P. Truscott, H. Uno, L. Urban, P. Urban, M. Verderi, A. Walkden, W. Wander, H. Weber, J. Wellisch, T. Wenaus, D. Williams, D. Wright, T. Yamada, H. Yoshida, D. Zschiesche, Geant4-a simulation toolkit, *Nuclear Instruments and Methods in Physics Research Section A: Accelerators, Spectrometers, Detectors and Associated Equipment* 506 (2003) 250–303. URL: [https://doi.org/10.1016/s0168-9002\(03\)01368-8](https://doi.org/10.1016/s0168-9002(03)01368-8). doi:10.1016/s0168-9002(03)01368-8.
- [139] J. Allison, K. Amako, J. Apostolakis, H. Araujo, P. A. Dubois, M. Asai, G. Barrand, R. Capra, S. Chauvie, R. Chytraccek, G. Cirrone, G. Cooperman, G. Cosmo,

- G. Cuttone, G. Daquino, M. Donszelmann, M. Dressel, G. Folger, F. Foppiano, J. Generowicz, V. Grichine, S. Guatelli, P. Gumplinger, A. Heikkinen, I. Hrivnacova, A. Howard, S. Incerti, V. Ivanchenko, T. Johnson, F. Jones, T. Koi, R. Kokoulin, M. Kossov, H. Kurashige, V. Lara, S. Larsson, F. Lei, O. Link, F. Longo, M. Maire, A. Mantero, B. Mascialino, I. McLaren, P. M. Lorenzo, K. Minamimoto, K. Murakami, P. Nieminen, L. Pandola, S. Parlati, L. Peralta, J. Perl, A. Pfeiffer, M. Pia, A. Ribon, P. Rodrigues, G. Russo, S. Sadilov, G. Santin, T. Sasaki, D. Smith, N. Starkov, S. Tanaka, E. Tcherniaev, B. Tome, A. Trindade, P. Truscott, L. Urban, M. Verderi, A. Walkden, J. Wellisch, D. Williams, D. Wright, H. Yoshida, Geant4 developments and applications, *IEEE Transactions on Nuclear Science* 53 (2006) 270–278. URL: <https://doi.org/10.1109/tns.2006.869826>. doi:10.1109/tns.2006.869826.
- [140] J. Allison, K. Amako, J. Apostolakis, P. Arce, M. Asai, T. Aso, E. Bagli, A. Bagulya, S. Banerjee, G. Barrand, B. R. Beck, A. G. Bogdanov, D. Brandt, J. M. C. Brown, H. Burkhardt, P. Canal, D. Cano-Ott, S. Chauvie, K. Cho, G. A. P. Cirrone, G. Cooperman, M. A. Cortés-Giraldo, G. Cosmo, G. Cuttone, G. Depaola, L. Desorgher, X. Dong, A. Dotti, V. D. Elvira, G. Folger, Z. Francis, A. Galoyan, L. Garnier, M. Gayer, K. L. Genser, V. M. Grichine, S. Guatelli, P. Guèye, P. Gumplinger, A. S. Howard, I. Hřivnáčová, S. Hwang, S. Incerti, A. Ivanchenko, V. N. Ivanchenko, F. W. Jones, S. Y. Jun, P. Kaitaniemi, N. Karakatsanis, M. Karamitros, M. Kelsey, A. Kimura, T. Koi, H. Kurashige, A. Lechner, S. B. Lee, F. Longo, M. Maire, D. Mancusi, A. Mantero, E. Mendoza, B. Morgan, K. Murakami, T. Nikitina, L. Pandola, P. Paprocki, J. Perl, I. Petrović, M. G. Pia, W. Pokorski, J. M. Quesada, M. Raine, M. A. Reis, A. Ribon, A. Ristić Fira, F. Romano, G. Russo, G. Santin, T. Sasaki, D. Sawkey, J. I. Shin, I. I. Strakovsky, A. Taborda, S. Tanaka, B. Tomé, T. Toshito, H. N. Tran, P. R. Truscott, L. Urban, V. Uzhinsky, J. M. Verbeke, M. Verderi, B. L. Wendt, H. Wenzel, D. H. Wright, D. M. Wright, T. Yamashita, J. Yarba, H. Yoshida, Recent developments in Geant4, *Nuclear Instruments and Methods in Physics Research Section A: Accelerators, Spectrometers, Detectors and Associated Equipment* 835 (2016) 186–225. doi:10.1016/j.nima.2016.06.125.
- [141] J. S. Coursey, D. J. Schwab, J. J. Tsai, R. A. Dragoset, Atomic weights and isotopic compositions with relative atomic masses, NIST Physical Measurement Laboratory Web Page, 2015. URL: <https://www.nist.gov/pml/atomic-weights-and-isotopic-compositions-relative-atomic-masses>.
- [142] T. D. Arber, K. Bennett, C. S. Brady, A. Lawrence-Douglas, M. G. Ramsay, N. J. Sircombe, P. Gillies, R. G. Evans, H. Schmitz, A. R. Bell, C. P. Ridgers, Contemporary particle-in-cell approach to laser-plasma modelling, *Plasma Physics and Controlled Fusion* 57 (2015) 113001. URL: <https://doi.org/10.1088/0741-3335/57/11/113001>. doi:10.1088/0741-3335/57/11/113001.
- [143] R. Lehe, A. Lifschitz, C. Thaury, V. Malka, X. Davoine, Numerical growth of emittance in simulations of laser-wakefield acceleration, *Phys. Rev. ST Accel. Beams* 16 (2013) 021301. URL: <https://link.aps.org/doi/10.1103/PhysRevSTAB.16.021301>. doi:10.1103/PhysRevSTAB.16.021301.

- [144] J. A. D. Pearce, Characterisation of two new ionisation chamber types for use in reference electron dosimetry in the UK, NPL REPORT DQL-RD001, National Physical Laboratory, 2004.
- [145] Geant4 book for application developers, Online book, 2019. URL: <http://geant4-userdoc.web.cern.ch/geant4-userdoc/UsersGuides/ForApplicationDeveloper/html/index.html>.
- [146] A. Subiel, V. Moskvina, G. H. Welsh, S. Cipiccia, D. Reboredo, P. Evans, M. Partridge, C. Desrosiers, M. P. Anania, A. Cianchi, others, Dosimetry of very high energy electrons (VHEE) for radiotherapy applications: using radiochromic film measurements and Monte Carlo simulations, *Physics in medicine and biology* 59 (2014) 5811. doi:10.1088/0031-9155/59/19/5811.
- [147] O. Lundh, C. Rechatin, J. Faure, A. Ben-Ismaïl, J. Lim, C. De Wagter, W. De Neve, V. Malka, Comparison of measured with calculated dose distribution from a 120-MeV electron beam from a laser-plasma accelerator: Laser-plasma accelerated high-energy electron beams for radiotherapy, *Medical Physics* 39 (2012) 3501–3508. doi:10.1118/1.4719962.
- [148] S. P. D. Mangles, C. D. Murphy, Z. Najmudin, A. G. R. Thomas, J. L. Collier, A. E. Dangor, E. J. Divall, P. S. Foster, J. G. Gallacher, C. J. Hooker, D. A. Jaroszynski, A. J. Langley, W. B. Mori, P. A. Norreys, F. S. Tsung, R. Viskup, B. R. Walton, K. Krushelnick, Monoenergetic beams of relativistic electrons from intense laser-plasma interactions, *Nature* 431 (2004) 535–538. URL: <https://doi.org/10.1038/nature02939>. doi:10.1038/nature02939.
- [149] J. Faure, Y. Glinec, A. Pukhov, S. Kiselev, S. Gordienko, E. Lefebvre, J.-P. Rousseau, F. Burgy, V. Malka, A laser-plasma accelerator producing monoenergetic electron beams, *Nature* 431 (2004) 541–544. URL: <https://doi.org/10.1038/nature02963>. doi:10.1038/nature02963.
- [150] C. G. R. Geddes, C. Toth, J. van Tilborg, E. Esarey, C. B. Schroeder, D. Bruhwiler, C. Nieter, J. Cary, W. P. Leemans, High-quality electron beams from a laser wake-field accelerator using plasma-channel guiding, *Nature* 431 (2004) 538–541. URL: <https://doi.org/10.1038/nature02900>. doi:10.1038/nature02900.
- [151] Gupta, B.L., A Low-Level Chemical Dosimetry System, Technical Report INIS-MF-209, Department of Atomic Energy, Bombay (India). Chemistry and Metallurgy Committee, India, 1970.
- [152] J. Geisselsoder, M. J. Kingkade, J. S. Laughlin, The radiation chemistry of aqueous ferrous sulfate-benzoic acid solutions, *Radiation Research* 20 (1963) 263. URL: <https://doi.org/10.2307/3571532>. doi:10.2307/3571532.
- [153] B. L. Gupta, R. M. Bhat, K. R. Gomathy, B. Susheela, Radiation chemistry of the ferrous sulfate-benzoic acid-xylene orange system, *Radiation Research* 75 (1978) 269. URL: <https://doi.org/10.2307/3574902>. doi:10.2307/3574902.

- [154] B. Gupta, S. Nilekani, Ferrous ion oxidations by H, OH and H₂O₂ in aerated FBX dosimetry system, *Radiation Physics and Chemistry* 53 (1998) 643–650. URL: [https://doi.org/10.1016/s0969-806x\(97\)00283-1](https://doi.org/10.1016/s0969-806x(97)00283-1). doi:10.1016/s0969-806x(97)00283-1.
- [155] B. Gupta, S. Nilekani, R. Bhat, G. Narayan, Free radical reactions in the FBX dosimetric system at low doses and dose-rates, *Radiation Physics and Chemistry* 49 (1997) 67–70. URL: [https://doi.org/10.1016/s0969-806x\(96\)00108-9](https://doi.org/10.1016/s0969-806x(96)00108-9). doi:10.1016/s0969-806x(96)00108-9.
- [156] B. Gupta, Radiation chemistry of xylenol orange in aqueous solutions at different acidities, *International Journal of Radiation Applications and Instrumentation. Part C. Radiation Physics and Chemistry* 33 (1989) 75–80. URL: [https://doi.org/10.1016/1359-0197\(89\)90097-0](https://doi.org/10.1016/1359-0197(89)90097-0). doi:10.1016/1359-0197(89)90097-0.
- [157] B. Gupta, R. Bhat, G. Narayan, B. Susheela, Acid and xylenol orange effects in the FBX dosimeter, *The International Journal of Applied Radiation and Isotopes* 34 (1983) 887–890. URL: [https://doi.org/10.1016/0020-708x\(83\)90148-5](https://doi.org/10.1016/0020-708x(83)90148-5). doi:10.1016/0020-708x(83)90148-5.
- [158] Z. Jia-Shan, W. Zhi-Li, C. Xin-Wei, Studies on the reaction mechanism in the irradiation of solutions containing ferrous ions, benzoic acid and xylenol orange, *Radiation Physics and Chemistry* (1977) 19 (1982) 439–441. URL: [https://doi.org/10.1016/0146-5724\(82\)90134-0](https://doi.org/10.1016/0146-5724(82)90134-0). doi:10.1016/0146-5724(82)90134-0.
- [159] B. Gupta, U. Kini, R. Bhat, Sensitivity of ferrous sulphate-benzoic acid-xylenol orange dosimeter (FBX system) to ¹⁰B(n, α)⁷Li recoils, *The International Journal of Applied Radiation and Isotopes* 27 (1976) 31–34. URL: [https://doi.org/10.1016/0020-708x\(76\)90165-4](https://doi.org/10.1016/0020-708x(76)90165-4). doi:10.1016/0020-708x(76)90165-4.
- [160] N. Bhat, D. Choudhary, A. Sarma, B. Gupta, K. Siddappa, Response of an FBX dosimeter to high LET ⁷Li and ¹²C ions, *Radiation Physics and Chemistry* 68 (2003) 909–916. URL: [https://doi.org/10.1016/s0969-806x\(03\)00112-9](https://doi.org/10.1016/s0969-806x(03)00112-9). doi:10.1016/s0969-806x(03)00112-9.
- [161] M. K. Semwal, M. Banerjee, A. Sarma, P. B. Vidyasagar, Response of the FBX system to a carbon beam: Its potential as a dosimeter in heavy particle radiotherapy, *Physics in Medicine and Biology* 47 (2002) N179–N183. URL: <https://doi.org/10.1088/0031-9155/47/12/403>. doi:10.1088/0031-9155/47/12/403.
- [162] B. Gupta, U. Madhvanath, G(Fe³⁺) values in the FBX dosimeter at low dose-rates, *The International Journal of Applied Radiation and Isotopes* 36 (1985) 985–987. URL: [https://doi.org/10.1016/0020-708x\(85\)90261-3](https://doi.org/10.1016/0020-708x(85)90261-3). doi:10.1016/0020-708x(85)90261-3.
- [163] B. Gupta, U. Kini, R. Bhat, Dose-rate and fractionation studies with FBX dosimeter, *The International Journal of Applied Radiation and Isotopes* 32 (1981) 701–704. URL: [https://doi.org/10.1016/0020-708x\(81\)90017-x](https://doi.org/10.1016/0020-708x(81)90017-x). doi:10.1016/0020-708x(81)90017-x.

- [164] B. Gupta, G. Narayan, R. Bhat, U. Kini, R. Ramaswamy, B. Suseela, Use of the FBX dosimeter for the quality assurance of ^{60}Co and high energy teletherapy machines by mail, *Physics in Medicine and Biology* 37 (1992) 2095–2102. URL: <https://doi.org/10.1088/0031-9155/37/11/006>. doi:10.1088/0031-9155/37/11/006.
- [165] B. Gupta, U. Kini, R. Bhat, U. Madhvanath, Use of the FBX dosemeter for the calibration of Cobalt-60 and high-energy teletherapy machines, *Physics in Medicine and Biology* 27 (1982) 235–245. URL: <https://doi.org/10.1088/0031-9155/27/2/005>. doi:10.1088/0031-9155/27/2/005.
- [166] O. Moussous, T. Medjadj, M. Benguerba, FBX aqueous chemical dosimeter for measurement of dosimetric parameters, *Applied Radiation and Isotopes* 69 (2011) 399–402. URL: <https://doi.org/10.1016/j.apradiso.2010.10.001>. doi:10.1016/j.apradiso.2010.10.001.
- [167] B. Gupta, R. Bhat, G. Narayan, S. Nilekani, Chemical dosimetry techniques for various applications under different geometries, *Radiation Physics and Chemistry* 59 (2000) 81–90. URL: [https://doi.org/10.1016/s0969-806x\(00\)00187-0](https://doi.org/10.1016/s0969-806x(00)00187-0). doi:10.1016/s0969-806x(00)00187-0.
- [168] S. Brindha, J. Rose, S. Sathyan, I. R. R. Singh, B. P. Ravindran, Modified ferrous ammonium sulfate benzoic acid xylenol orange (MFBX) and thermoluminescent dosimeters – a comparative study, *Physics in Medicine and Biology* 47 (2002) N153–N158. URL: <https://doi.org/10.1088/0031-9155/47/11/403>. doi:10.1088/0031-9155/47/11/403.
- [169] S. Upadhyay, A. Reddy, M. Gupta, A. Nagaratnam, A tissue-equivalent modified FBX dosimetric system, *The International Journal of Applied Radiation and Isotopes* 33 (1982) 47–49. URL: [https://doi.org/10.1016/0020-708x\(82\)90205-8](https://doi.org/10.1016/0020-708x(82)90205-8). doi:10.1016/0020-708x(82)90205-8.
- [170] C. Gay, J. Collins, J. M. Gebicki, Determination of iron in solutions with the ferric-xylenol orange complex, *Analytical Biochemistry* 273 (1999) 143–148. URL: <https://doi.org/10.1006/abio.1999.4207>. doi:10.1006/abio.1999.4207.
- [171] L. Sommer, *Analytical absorption spectrophotometry in the visible and ultraviolet: the principles*, Elsevier, Amsterdam New York, 1989.
- [172] J. Seuntjens, M. Olivares, M. Evans, E. Podgorsak, Absorbed dose to water reference dosimetry using solid phantoms in the context of absorbed-dose protocols, *Medical Physics* 32 (2005) 2945–2953. URL: <https://doi.org/10.1118/1.2012807>. doi:10.1118/1.2012807.
- [173] O. Moussous, K. Yahiche, T. Medjadj, Study of the Metrological Characteristics of the FBX Dosimeter in the Photon Beam using a Secondary Standard, *Proceeding of the Sixth Nuclear and Particle Physics Conference* (2008) 477–484.



Contents lists available at ScienceDirect

Nuclear Inst. and Methods in Physics Research, A

journal homepage: www.elsevier.com/locate/nima

Technical Notes

1 kHz laser accelerated electron beam feasible for radiotherapy uses: A PIC–Monte Carlo based study

R. Polanek^{a,*}, Nasr A.M. Hafz^{a,b,c}, Zs. Léczi^a, D. Papp^a, C. Kamperidis^a, Sz. Brunner^a, E.R. Szabó^a, T. Tórkés^a, K. Hideghéty^{a,d}^a ELI-ALPS, ELI-HU Non-Profit Ltd. Wolfgang Sandner u. 3, H-6728 Szeged, Hungary^b National Laboratory on High Power Laser and Physics, SIOM, CAS, Shanghai 201800, China^c Department of Plasma and Nuclear Fusion, Nuclear Research Center, Atomic Energy Authority, Abu-Zabal 13759, Egypt^d University of Szeged, Faculty of Medicine, Department of Oncotherapy, Korányi fasor 12., H-6720, Szeged, Hungary

ARTICLE INFO

Keywords:

LWFA acceleration
Electron radiotherapy

ABSTRACT

Laser wakefield acceleration (LWFA) offers a promising compact solution for the production of high and very high energy electron (VHEE) beams, which have an ultrashort pulse duration with a high instantaneous dose rate and small source size. These unique properties are of radiobiological as well as clinical interest. In this paper we focus on the potential application of high repetition rate LWFA electron beams for radiobiology and radiotherapy. On the basis of particle-in-cell (PIC) and Monte Carlo simulations we propose that, using a commercially available 1 kHz laser system one can generate electron beams with 35.7 MeV mean energy and 3 pC electron bunch charge at 1 kHz repetition rate to deliver a dose rate of 18 Gy/min, which could be extremely useful for real radiotherapy applications. Thanks to the high repetition rate, dose delivery can be performed with high precision making this system a potential alternative to conventional clinical electron accelerators.

1. Introduction

It is now sixty-seven years since the first dedicated medical electron linear accelerator (LINAC) was used to treat cancers. This milestone opened new prospects in the development of radiotherapy techniques, which have remained indispensable in the fight against cancer. The main paradigm of radiotherapy has not changed essentially over the years. However, the underlying technology and the techniques have significantly improved. Intensity modulated radiation therapy (IMRT), image-guided radiotherapy (IGRT), stereotactic body radiation therapy (SBRT), stereotactic ablative radiotherapy (SABR) are just a few radiotherapy techniques which have significantly benefited from the technological enhancement of particle accelerators.

Electron beam therapy is a widely used radiotherapy technique for the irradiation of superficial target volumes. Accelerators currently used in clinical practices generate electron beams with energies between 6 and 24 MeV, which allows a relatively uniform dose delivery to a depth of 1 to 6 cm. These clinical electron beams are used in the treatment of skin, breast and chest wall cancers; peripheral lymphatic regions of head and neck cancers; and for the irradiation of other neoplastic diseases. Electron beams can also be used in intra-operative applications for selective dose delivery to the tumor bed after

the surgical removal of pancreatic, colorectal cancers and soft tissue sarcomas [1].

As far as the particle accelerator technology is concerned, there is a trend in using high-power laser beams and gaseous plasma (fully ionized gas) media to build compact electron accelerators. In 1979, Tajima and Dawson [2] proposed a scheme for electron acceleration to relativistic energies by ultraintense electrostatic plasma waves (called “laser wakefield”) driven by ultrashort focused laser pulses during their propagation in under-dense gaseous plasma medium. This laser–plasma acceleration scheme is called “laser wakefield acceleration” (LWFA) and it has attracted significant interest in recent years [3–5] due to the availability of commercial, ultracompact, solid-state terawatt laser systems [6].

Generally, the use of optical mirrors instead of high-power magnets provides relative flexibility in beam delivery, and offers new possibilities in facility design, cost reduction, and in the development of new radiotherapy techniques. These advantages are not self-evident in experimental laser facilities which require sophisticated and delicate infrastructure. However, the inherent strengths of such systems, and the rapid technological progress make laser–plasma acceleration in general and LWFA in particular a promising alternative to conventional RF-based accelerators.

* Corresponding author.

E-mail address: robert.polanek@eli-alps.hu (R. Polanek).

With LWFA techniques it is easy to produce very high energy electron beams (VHEE, electrons with energies above 50 MeV). VHEE beam therapy has recently emerged as a novel option for cancer radiotherapy. *In silico* studies have shown that VHEE beams have a more favorable dose distribution than advanced photon techniques and in some situations, the results approach the charged particle therapy values. Monte Carlo simulation based plans, using electron beams with energies above 100 MeV provided a very good dose conformation, while offering significantly improved dose sparing of healthy tissue when compared to intensity modulated and volumetric arc photon therapy [7–10]. VHEE plans were superior to IMRT plans but they could also be delivered orders of magnitude faster than photon plans mainly due the higher particle production efficiency and the ability to steer charged particles in a millisecond timescale [10].

However, such VHEE beams are only available at a few academic laboratories. For example, the Next Linear Collider Test Accelerator (NLCTA) located at the SLAC National Accelerator Laboratory is capable of producing high-brightness electron beams, with energy between 60 and 150 MeV which supports the development of the VHEE therapy [11]. There are only few more such experimental facilities where VHEE beams can be produced for experimental studies. In order to make VHEE beams widely available, LWFA offers a potential alternative to conventional RF-based accelerators for the production of electron beams.

Furthermore, LWFA electron beams have several unique properties which make them attractive for applications in radiobiology and radiotherapy. For example, the low divergence of the generated electron beams facilitates the formation of microbeams, which in the MeV energy range may be beneficial in cancer therapy [12,13]. In general, an electron beam having a short bunch duration (ps at the sample position) leads to a very high instantaneous radiation dose rate. This can be useful for the state-of-the-art FLASH technique, which requires a high instantaneous dose rate. This novel radiotherapy technique seems to increase the therapeutic ratio by reducing both the acute side effects on normal tissues and late complications [14,15]. However, recent experiments show that several factors such as instantaneous and mean dose rate, total dose and the pulsatile nature of the beam may influence the FLASH effect. So far, no clear consensus has been reached in this issue. A valuable review on this subject has been recently published by Wilson et al. [16].

In fact, LWFA electron bunches are extremely short; they are in the order of a few femtoseconds (fs) immediately after acceleration [17], which enables radiation chemists to conduct pulse radiolysis experiments at a time scale which has not been available until now [18]. Such ultrafast pulse radiolysis (also known as femtolysis) experiments significantly contribute to our understanding of the biological effects of radiation.

However, active research in LWFA has revealed some efficiency, stability and reliability issues that need to be resolved prior to its implementation. Efficiency in terms of pulse charge and repetition rate ensures the necessary dose rate, which must be at least 4 Gy/min for real radiotherapy applications. The moderate stability of LWFA accelerators in terms of energy and pulse charge is the primary task which requires immediate attention before such accelerators are introduced into real radiobiological or medical applications. Furthermore, the reliability and effectiveness of beam shaping must be enhanced. Fortunately, there is a significant progress toward stable LWFA electron beams [19,20].

In this study we investigate high repetition rate LWFA electron beams recently reported by Guénot et al. [21] and Ouilé et al. [22]. We analyze the potential of those beams for radiobiology and radiotherapy purposes. High repetition rate electron beams can be generated by commercially available 1 kHz laser systems (multi-TW power & few-cycle pulse duration); one such system is currently operational at ELI-ALPS Research Institute [6]. Using Monte Carlo simulations we demonstrate that this type of 1 kHz LWFA is capable of generating a sufficient dose

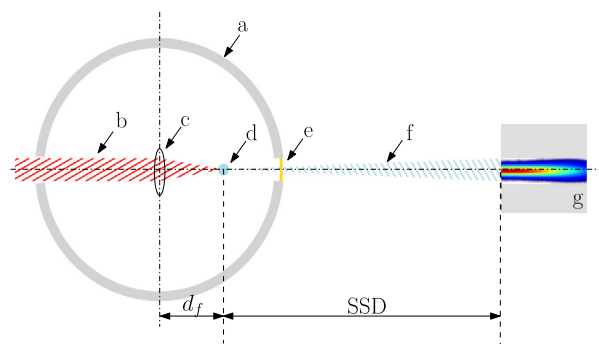


Fig. 1. The semi-realistic model of irradiation geometry used in the MC simulations. The laser beam (b) enters the vacuum chamber (a) and is focused using optics (c) onto a gas jet target (d) where LWFA acceleration takes place. The accelerated electrons (f) exit the vacuum chamber through a Mylar window (e). Absorbed dose is calculated in the water phantom (g) placed at different source-to-surface distances (SSD).

rate for practical radiobiological or medical applications. The critical issues such as low radiation dose per electron bunch and the relatively low stability of such systems can, in principle, be compensated for if the LWFA operates at 1 kHz. Additionally, we outline some practical issues and pitfalls which need to be addressed before such systems are used in real applications.

2. Methods

To assess the dosimetric characteristics, Monte Carlo simulations were performed based on the Geant4 (version 10.3) Monte Carlo simulation framework [23,24] on a workstation with an Intel Xeon 16-core processor.

Fig. 1 shows the semi-realistic geometry used in the simulation scenarios. Electron acceleration takes place in the vacuum chamber (a) at the gas-jet target (d). The accelerated electron beam exits the vacuum chamber through a 300 μm thick circular Mylar window (e). The absorbed dose is calculated in a water phantom (g), a box with 6 mm thick Plexiglas walls filled with liquid water and placed in front of the Mylar window at different source to surface distances (SSD). The materials for all geometric components of the simulation were set using the materials defined in the NIST materials database [25].

The electron beam source was simulated based on the electron beam characteristics obtained from 3D particle-in-cell (PIC) simulations, which were performed using the EPOCH open source code [26] with the parameters of the SYLOS II laser system available at ELI-ALPS.

The position, energy and direction of each electron in the beam were derived from a data file generated by the 3D PIC simulation, taking in account the correct weighting factor, as well as the position and momentum of each pseudo-electron. These parameters were then used to set up the initial electron parameters in the MC simulations.

The PIC simulations used the following laser parameters: pulse duration 8 fs (FWHM), peak power 4 TW (corresponding to 30 mJ total energy per pulse) and 1 kHz repetition rate. The laser beam was focused to a 2.2 μm focal spot diameter (FWHM), resulting in $2 \cdot 10^{19}$ W/cm² peak intensity. The Rayleigh length of such a tightly focused laser pulse is around 100 μm , wherefore we use a very narrow He (helium) gas jet as a target, where the maximum electron density after ionization is $n_0 = 4 \cdot 10^{19}$ cm⁻³. The spatial density profile is described by a super Gaussian function:

$$n_e = n_0 e^{-\frac{(z-z_0)^4}{2\sigma^4}}, \quad (1)$$

where $z_0 = 70$ μm and $\sigma = 38$ μm . In the radial direction the plasma density is assumed to be uniform. The laser pulse is focused at $z = 50$ μm , 20 μm before the center of the gas jet. Due to tight focusing, the laser intensity increases quickly along the propagation

axis, which results in electron self-injection into the wakefield. The injected electrons are accelerated over a distance of 50 μm reaching an average energy above 30 MeV with a small energy-spread, as shown below.

The simulation grid was 35 nm in the z direction and 50 nm in the lateral directions, which means that each macroparticle (pseudo-electron) contains 875 real electrons. The plasma electrons are represented by 4 particles per cell. For the field solver we use a special method presented by Lehe et al. [27], in order to compensate for the grid dispersion, which can generate errors in the laser propagation.

The depth dose was scored for different SSD distances by a 3D ROOT histogram. The number of bins in all directions were chosen to form a 1 mm^3 voxel size. The 100 cm reference SSD distance was chosen in our discussion, which is the standard SSD distance used in clinical dosimetry measurements.

The physics of the simulations were set up using the physics-list mechanism of the Geant4 toolkit and the QGSP_BIC_HP_EMZ physics models, recommended for medical uses [28]. This physics-list includes the hadronic models from which the photo-nuclear and electro-nuclear interactions are useful for our purposes. The EMZ option contains the electromagnetic physics models, including the photoelectric effect, Compton and Rayleigh scattering for gamma particles and for charged particles ionization and Bremsstrahlung. The range cut was set to 30 μm , which is converted at initialization time into energy threshold for secondary gamma, electron, positron and proton production.

3. Results and discussion

As stated in the Introduction, our main aim is to assess the potential of using a 1 kHz laser driven electron beam for radiotherapy and radiobiology applications. Recently Guénot et al. [21] reported high-quality 6 MeV relativistic electron beams having an energy spread of 3 MeV and a charge of ~ 0.5 pC with 30% fluctuation using 1 kHz repetition rate, single-cycle, 2.1 mJ laser pulses with 3.4 fs pulse duration in nitrogen gas jet.

However, reliable radiotherapy applications require 6 MeV or greater electron energies. Based on our PIC simulations, such beams can be produced with the parameters of the SYLOS II laser system available at ELI-ALPS. The SYLOS II laser is a 1 kHz repetition rate “few-cycle” laser with optical parametric chirped pulse amplification (OPCPA), which generates 5 TW, few-cycle laser pulses at a high repetition rate, with a central wavelength of 880 nm. The pulse energy is over 35 mJ with less than 8 fs pulse duration, combined with remarkable long-term stability. SYLOS II is the first laser system to have demonstrated multi-TW, few-cycle laser pulses at a high repetition rate [6].

Fig. 2a shows the energy spectra of the accelerated electrons right after the acceleration (solid line) and at the phantom surface (dashed line). The corresponding average kinetic energy of the accelerated electrons are 35.97 MeV and 35.73 MeV, respectively with an FWHM of ≈ 6 MeV. The slight difference between the two spectra is the result of electron scattering during propagation from the plasma point to the phantom surface. Because the electrons are light particles, they undergo considerable scatter during propagation. During this, their energy and propagation direction slightly change and some electrons are lost from the beam resulting in an energy spectrum with less intensity and shifted toward lower energies and with broadened energy peaks. This effect is more evident at low than at high energies. Therefore, at highly relativistic energies this scattering effect is negligible, which is also confirmed by the mean kinetic energies.

The spectra presented in Fig. 2a contain electrons with kinetic energies above 20 MeV, however, there is a non-negligible, low-energy background (Fig. 2b). These low energy electrons are usually generated with a large divergence angle, therefore they do not contribute to the absorbed dose and were omitted from the simulations. On the other hand, such electrons produce considerable Bremsstrahlung radiation

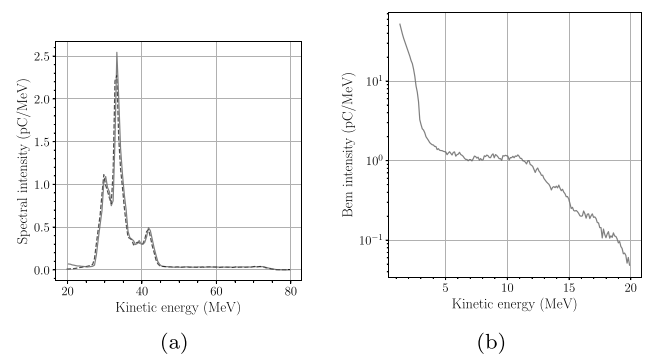


Fig. 2. (a) The energy spectra of the simulated electron beam at the acceleration site (solid line) and at the phantom surface situated at an SSD of 100 cm. The long high-energy tail of the energy spectrum is a specific feature of the self-injection mechanism. (b) The energy spectra of electrons with low energy (up to 20 MeV). They are excluded from simulations due to their large divergence.

when they are dumped, which must be considered in terms of radiation protection.

The long high-energy tail of the energy spectrum is a specific feature of the self-injection mechanism in LWFA. Here, electrons are accelerated during the initial phase of the injection, when all electrons are located at the peak electric field of the ion cavity. This process is very sensitive to the laser and plasma parameters. Consequently, the amount of electrons is so low that they are ignored in experiments.

The multi-peak nature of the energy spectra is believed to be a natural outcome of the LWFA acceleration process in high-density plasma due to the extremely high-field gradient of the plasma wave. In other words, since the electron bunch size in 3D is around $1 \mu\text{m}^3$, it means that some electrons get slightly out of the extremely-narrow acceleration phase during the propagation in the wake behind the laser pulse, which results in minor peaks around the main high-energy peak. It is also a result of the slightly different velocity of the accelerated electrons in comparison to the wakefield phase velocity. This phenomenon, which is known as the “dephasing effect” can be mitigated by a careful control of plasma density or by some plasma density profiling [29–31].

Such a multi-peak spectrum may produce some inhomogeneity in the depth dose distribution, however this effect can be neglected as long as the energy peaks are close to one another. This means that the spectrum can be approximated with a single, broadened-energy peak. This wide energy peak produces a depth dose distribution with a broader and flatter plateau around the depth of dose maximum than a narrower energy peak, which can be useful when large volumes of interest need to be irradiated homogeneously.

As can be seen in Fig. 3, the produced electron beam is slightly asymmetric in the transverse plane (Figs. 3a and 3b), and its propagation direction is – to some extent – different from the z direction. Both properties are due to the linear polarization of the laser pulse. Indeed, the electric field of the laser pulse oscillates along the x direction, thus the injected electrons will have slightly larger momentum in direction that. However, this beam asymmetry can be ignored because the scattering effects in the exit window and air smooth the electron distribution and lead to a Gaussian spatial distribution (Figs. 3c and 3d). Furthermore, the resulting deviation in the direction of propagation with respect to the z axis is well below 10 mrad, which can be considered about the same as the maximum shot-to-shot pointing angle instability of the electron beam, a common issue with LWFA electron beams. However, even this small but random pointing angle instability is compensated for by the 1 kHz repetition rate of the system. Consequently, in practice, we obtain a slightly enlarged, Gaussian shaped and centered electron distribution. Furthermore, this also means that the issue of shot-to-shot reproducibility in terms of the electrons’ spatial distribution and propagation direction can be neglected as long as the propagation angle is smaller than the pointing angle instability.

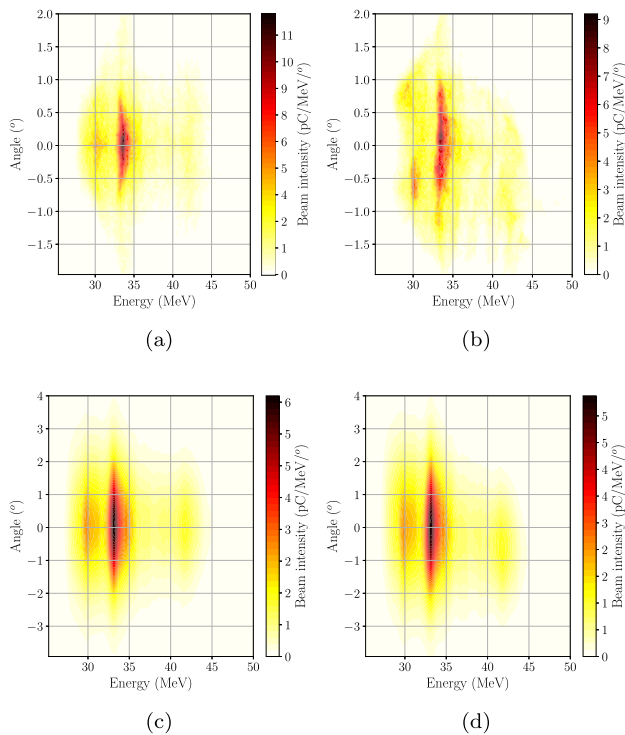


Fig. 3. The electrons angular distribution in function of their kinetic energy in x - z plane **3a** and in y - z plane **3b** immediately after acceleration and at the phantom surface (**3c** and **3d** respectively).

It is important to note that this result refers to unconditioned electron beams. The real energy and angular distribution can be significantly altered by the scattering conditions. Scatter from collimators and other structures in the experimental setup has a significant effect on these characteristics, and influences dose distribution at least to the depth of dose maximum.

So far we can conclude that the 35.7 MeV mean electron energy combined with the quasi monoenergetic nature of the spectrum makes this electron beam suitable for radiotherapy applications. The main objective is to achieve a dose rate suitable for such applications. It is agreed that at least 1 to 10 Gy/min dose rate is necessary for successful practical applications [12].

In a first approach, the total dose rate at the target surface can be estimated by integrating the following formula (Eq. (2)) over the whole energy spectrum of the incident electron beam:

$$\dot{D}(E) = 1.602 \cdot 10^{-10} \Psi(E) \cdot \left(\frac{dE}{\rho dx} \right)_{T,w}, \quad (2)$$

where $\Psi(E)$ is the energy fluence at the target surface, $(dE/\rho dx)_{T,w}$ is the total mass stopping power in water and $1.602 \cdot 10^{-10}$ represents the unit conversion factor between MeV/g and Gy. Using the beam spectra (Fig. 2) and the NIST data of total mass stopping power [25], the total dose rate at a distance of 100 cm is 2.901 Gy/pC/s. Since in practice we expect a higher pulse charge than 1 pC, this value is sufficient for real applications.

However, Eq. (2) gives us a rough estimate of the absorbed dose in a water phantom. For a more accurate estimate, we must consider the radiation yield produced by Bremsstrahlung, the variation of beam spectra with depth and the build-up effect, which jointly determine the particular form of the electron depth dose curve. Therefore, we performed Monte Carlo simulations using the electron beam parameters (electron position, direction and kinetic energy) obtained with the PIC simulations.

The dose rate for different SSDs was calculated at the depth of dose maximum. The obtained results are summarized in Table 1. Because the

Table 1

Key parameters and results of the simulations.

Laser beam pulse length (FWHM)	8 fs
Peak power	4 TW
Repetition rate	1 kHz
Focal spot diameter (FWHM)	2.2 μ m
Peak intensity	$2 \cdot 10^{19}$ W cm ⁻²
Target	He gas jet
Max. e- density	$4 \cdot 10^{19}$ cm ⁻³
Expected e- pulse charge	3–10 pC
Mean kinetic energy	35.97 MeV
Angular distribution (FWHM)	1.13 °
Expected dose rate for 100 cm SSD	6 Gy/min/pC
Instantaneous dose rate	$3.9 \cdot 10^6$ Gy/s/pC
Depth of dose maximum in water for SSD = 100 cm	1.9 cm
Therapeutic range	~5 cm

standard SSD used in radiotherapy is 100 cm, in the following we will refer to this SSD value. For this distance, the depth of dose maximum is 1.9 cm and the amount of dose delivered by a single electron bunch with 1 pC charge is 97.1 μ Gy. From the 3D PIC simulations we can conclude that the electron bunch charge is 3 pC and the amount of dose delivered by a single electron bunch totals ~ 0.3 mGy. This very small amount of dose can be enhanced dramatically by operating the LWFA at 1 kHz repetition rate, which results in a mean dose rate of 0.3 Gy/s or 18 Gy/min, which is comparable to the performance of medical LINACs.

However, through the careful optimization of laser and gas target parameters, the electron bunch charge can be increased, and is expected to reach charges exceeding 10 pC. This means that the above calculated dose rate can be higher by a factor of ten. With such a high dose rate, the LWFA acceleration technique becomes rival of today's LINAC systems.

On the other hand, it is well known that the LWFA electron acceleration process is particularly sensitive to laser system stability in terms of energy, focus point position and other optical parameters, as well as plasma generation from gas jets. The major uncertainty comes from fluctuation in the beam pulse charge. For example, Guénot et al. [21] reported a 30% shot to shot fluctuation in charge. This fluctuation has a direct effect on the achievable absorbed dose and represents the key condition for radiotherapy applications. It is known that 7% uncertainty in absorbed dose can modify biological outcomes. For this reason, in radiotherapy practice the maximum permissible cumulative uncertainty in dose delivery is 5%, including uncertainties in treatment planning, patient positioning, dose measurements etc. Fortunately, there has been an impressive progress in the stabilization of LWFA electron beams.

In the following we prove that operating the LWFA at 1 kHz repetition rate provides precise control over dose delivery. Assuming a normal distribution of pulse to pulse charge fluctuation with FWHW of 30% as reported by Guénot et al. [21], the total dose delivered by n shots of 1 pC can be written as:

$$D = \sum_{i=1}^n D_{1pC} q_i, \quad (3)$$

where D_{1pC} is the dose delivered by a single shot with 1 pC charge and q_i is the charge of each shot. The shot to shot charge fluctuation follows a normal distribution, which can be described with the probability distribution:

$$p(q_i) = \frac{q_{mean}}{\sigma \cdot \sqrt{2 \cdot \pi}} \cdot e^{-\frac{(q_i - 1)^2}{2 \cdot \sigma^2}}. \quad (4)$$

With a constant pulse charge of 1 pC and with a standard deviation of $\sigma = 30\%$, for a dose of 1 Gy, we need approximately $n = 10^4$ shots. Sampling n number of shots with a normal distribution of charge and applying Eq. (3), n shots deliver 1 Gy with an uncertainty of 0.30%.

This means that our results fit with this condition very well. Moreover, higher laser beam instability is also acceptable (not the case of

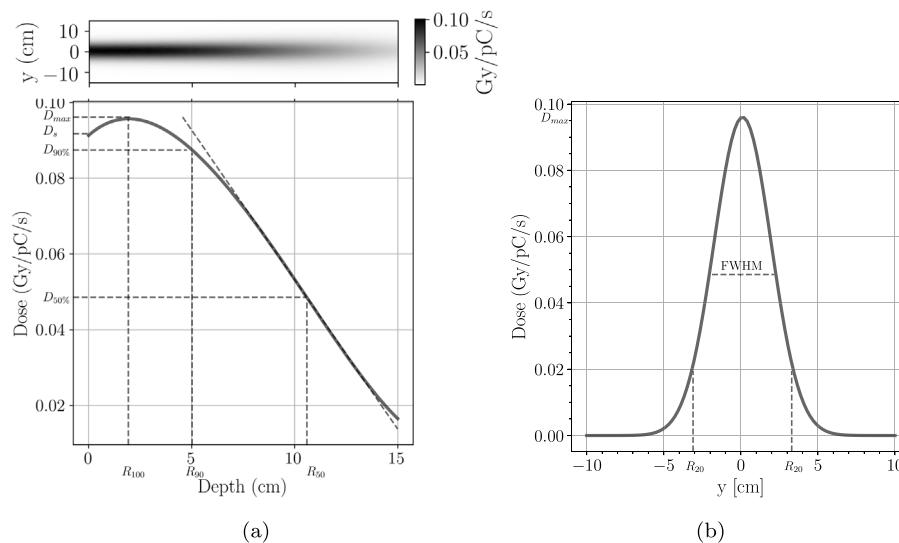


Fig. 4. The absorbed dose characteristics of the unconditioned electron beam; (a) the dose distribution map and depth dose curve with dosimetric characteristics: the dose maximum $D_{max} = 9.7$ cGy/pC/s at depth of 1.93 cm; the therapeutic range $R_{90} = 5$ cm defined as the depth where the absorbed dose equals 90% of D_{max} . (b) the transverse dose profile at the depth of dose maximum with the full width at half maximum FWHM = 4 cm.

the SYLOS II laser system at ELI-ALPS, which is an ultrastable system), on the basis of which we can confidently state that the 1 kHz LWFA-based electron beams have a high potential for radiobiological and/or radiotherapy applications.

Fig. 4a presents the absorbed dose map and the corresponding central depth dose curve, which has a shape typical of electron beams. The entrance dose or surface dose (D_s) is stated at 0.5 mm depth and is 0.091 Gy/pC/s, which represents 94% of D_{max} (which is generally between 90% and 100% for electron energies above 10 MeV) [32]. The initial rise of the curve is due to the increasing electron fluence with depth, determined by the increasing mean incident angles as a result of electron scattering. The absorbed dose continues to increase until the outgoing electrons from an elementary volume are compensated with the electrons leaving that volume (i.e. electronic equilibrium is assured). At this point the depth dose curve becomes relatively flat until electrons leave the beam and the curve begins to fall at a rate depending on the initial beam energy. Our simulated depth dose curve reaches a dose maximum of $D_{max} = 0.097$ Gy/pC/s at a depth of $R_{100} = 1.93$ cm. The depth of dose maximum and the shape of the curve around this depth are determined by the balance of scatter effects and electron loss, therefore it depends on beam energy and scattering conditions (irradiation geometry, field size and shape, accelerator head design etc.). The therapeutic range, defined as the depth where the absorbed dose equals 90% of D_{max} ($D_{90\%}$) represents a relatively uniform dose region which can be used effectively for practical applications. In our case the therapeutic range is around 5 cm.

The distal part of the curve is described by the dose gradient, which is steeper for low energies and becomes less steep as the energy increases. In practice, this distal part of the depth dose curve can also be described by the depth (R_{50}) where the depth dose becomes half of the maximum ($D_{50\%}$). However, this characteristic is significantly affected by the components of accelerators as well as by the medium in which the electrons propagate.

The simulated electron beam at the focal point has a diameter of 0.3 μm in the transverse plane and has a bunch length of 20 μm . The divergence angle is 0.9°, which results in a beam size of 3.14 cm at 100 cm source to surface distance at FWHM (Fig. 4a), which grows to 4.1 cm at the depth of dose maximum (Fig. 4b). This electron beam produces a dose distribution having a transverse dose profile with a high central dose, which rapidly falls forming non-uniform transverse dose distribution. This significantly affects the usability of the beam.

The above results were obtained using the electron beam parameters taken from the PIC simulation, which describe the electron bunch right after it exits the plasma medium. However, the electron beam suffers changes during propagation toward the irradiation target. These changes strongly correlate with the design and components of the accelerator and affect both dose distribution and the usability of the beam. In this raw form, this electron beam exhibits favorable properties for radiotherapy, but further beam preparations maybe needed for real applications. The geometrical properties (field shape and dimensions) are too large for pencil beam irradiation techniques, and too small for conventional techniques that usually require square fields measuring up to 25 cm \times 25 cm. Such fields can be achieved using either a dual scattering foil system or the spot scanning technique. The former is the most common technique used in LINAC based radiotherapy systems due to its reliability.

A dual scattering foil consists of a scatterer foil and a second flattening foil. The former is made from a material with a high atomic number, and it has an optimal thickness which produces the desired scattering effect. The second foil is made from a material with a low atomic number, it has a conical shape and is designed to flatten the scattered beam. When designing such a system one needs to consider the size and flatness of the obtained beam as well as the decrease in the number of electrons, the degradation of the energy spectrum (broadening and shifting toward the lower energies) and the Bremsstrahlung photon contamination. However, even a carefully designed system may suffer from beam degradation, which can be compensated by the adjustment of the incoming beam parameters (particle numbers, energy, etc.)

We performed several simulations to estimate the feasibility of this solution, although the development of a dual scattering foil system is beyond the scope of this paper. Using an Au foil as the scattering foil and a conical Al foil as the flattening foil, together with a rectangular diaphragm to collimate the beam to the desired shape we obtained a rough estimate of the dose rate. The dose rate obtained for two beams with fields of 15 cm \times 15 cm and 20 cm \times 20 cm is 1.1 mGy/pC/s at a depth of 1.8 cm and 0.9 mGy/pC/s at a depth of 2.2 cm, respectively. From these preliminary results we can conclude that this solution cannot be applied to our case without the need to significantly increase the pulse charge.

In contrast, the scanning beam technique seems to be a viable alternative to produce larger field sizes. Based on our MC simulations, we can demonstrate that with the available dose rate obtained with 1 pC pulse charge, the spot scanning system can produce a beam size

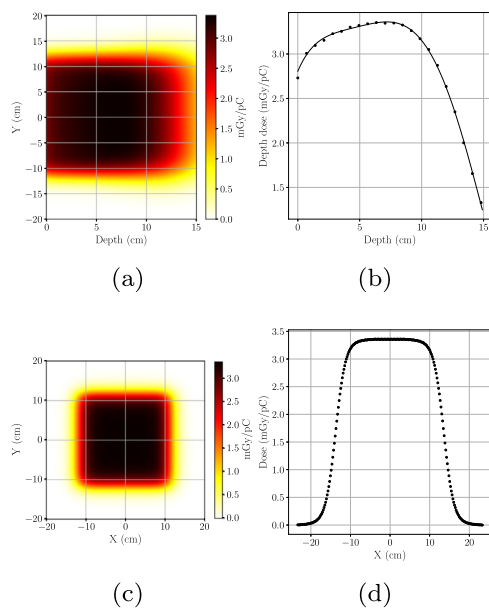


Fig. 5. Dose map, depth dose curve and dose profile at maximum dose depth, obtained with the spot scanning technique. The dose distribution was obtained by summing as many beams as necessary to produce a 20 cm \times 20 cm square beam. In Fig. 5 it can be observed that the therapeutic range is enlarged, due to electronic equilibrium which is only partially realized in case of the original beam.

of 20 cm \times 20 cm in a few tens of milliseconds, with a central axis depth dose of about 0.275 mGy at the depth of dose maximum. This means, that the dose rate which can be achieved with spot scanning method is 1.65 Gy/min/pC. Considering the pulse charge of 3 pC, obtained from PIC simulations, the dose rate improves to a modest but usable value of 4.95 Gy/min. These results were obtained by simulating the spot scanning technique using the previously generated depth dose data. Fig. 5 presents the dose maps, the depth dose curve and profile at the depth of dose maximum for a beam field of 20 cm \times 20 cm. As it can be seen, both the beam width, and the therapeutic range are enlarged, and dose profile homogeneity also improves due to the increased field size.

The spot scanning technique offers beams with less Bremsstrahlung contamination and without energy spectra broadening. Scanning beam techniques generally produce a deeper therapeutic range and steeper fall-off when compared with the scattering foil method. Furthermore, in the conventional electron beam therapy usually individually shaped, irregular fields are needed, therefore the spot scanning technique would be a possible solution. However, this technique assumes more complex technical solutions, which increases the possibilities of errors. For this reason, this technique is not preferred in clinical accelerators.

4. Conclusion

Laser driven electron acceleration represents a long-awaited breakthrough in the development of novel radiotherapy facilities. The feasibility and suitability of real particle beam parameters can be investigated using currently available high-power laser systems.

Electron beams produced in plasma by a 1 kHz high repetition rate laser system may provide a promising alternative for conventional accelerators. In this study we have shown that this laser system can produce electron beams with high energies (35.97 MeV mean kinetic energy) and acceptable dose rates (18 Gy/min considering the electron bunch charge of 3 pC obtained by PIC simulations) and doses delivered with very high precision, due to the high repetition rate of the system.

Our results suggest that this LWFA acceleration technique can be a promising alternative for RF-based conventional LINAC electron accelerators. The beam energy and charge can be controlled by modifying

the target length and plasma density via changing the gas jet pressure, even during the operation. This will enable researchers to perform intensity and energy modulated irradiation. The energy modulation and the spot scanning technique together could open extremely important application spectra for electron irradiation of superficial targets with uneven thickness, providing significant normal tissue protection.

Moreover, theoretical studies suggest several possible novel applications of the presented LWFA system. Due to the small divergence of the beam, it is relatively easy to further narrow the beam and produce pencil beams for spot scanning techniques. Furthermore, we see the possibility of producing so-called microbeams, which are extensively researched due to their improved therapeutic effects.

The mean bunch length (pulse duration) of an electron shot is 2 ps at 100 cm from the source, which leads to an instantaneous dose rate of an electron shot with 1 pC charge of 6×10^5 Gy/s. This very high instantaneous dose rate can open a new avenue to studying the so-called FLASH effects where the ultrahigh instantaneous dose rate can substantially enhance the therapeutic window [14–16]. However, it is important to note that the conditions to produce the FLESH effect are not clearly defined in the literature. It seems that the instantaneous dose rate may be one of the conditions, however, the repetition rate must be not too high to mitigate the oxygen scavenging effect of a high dose rate (see Wilson et al. [16]).

As we can see, there are many possibilities as well as issues to be solved prior to real applications. Our in silico study represents a promising start for further scientific work on laser driven electron source development. As soon as the experimental facility is assured, intensive work is planned to find the best beam steering solution, to develop the suitable beam monitoring and dosimetry system and to realize the necessary technical conditions for the first radiobiological experiments.

CRediT authorship contribution statement

R. Polanek: Conceptualization, Methodology, Software, Visualization, Investigation, Writing - original draft. **Nasr A.M. Hafz:** Conceptualization, Validation, Supervision, Writing - review & editing. **Zs. Lécz:** Software, Validation. **D. Papp:** Conceptualization, Validation, Supervision. **C. Kamperidis:** Conceptualization, Supervision. **Sz. Brunner:** Resources. **E.R. Szabó:** Resources. **T. Tóké:** Project administration. **K. Hideghéty:** Conceptualization, Supervision.

Declaration of competing interest

The authors declare that they have no known competing financial interests or personal relationships that could have appeared to influence the work reported in this paper.

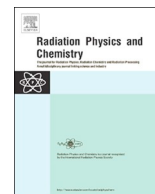
Acknowledgments

This work was supported in part by the European Union and co-financed by the European Regional Development Fund through the ELI-ALPS project (GINOP-2.3.6-15-2015-00001), and in part by Horizon 2020, the EU Framework Programme for Research and Innovation under Grant Agreement No. 654148 and No. 871124 Laserlab-Europe.

N. A. M. H. acknowledges the President International Fellowship Initiative (PIFI) of the Chinese Academy of Sciences; the International Partnership Program (181231KYSB20170022) of CAS; the Inter-Governmental Science and Technology Cooperation of MOST.

References

- [1] K.R. Hogstrom, P.R. Almond, Review of electron beam therapy physics, *Phys. Med. Biol.* 51 (13) (2006) R455–R489, <http://dx.doi.org/10.1088/0031-9155/51/13/r25>.
- [2] T. Tajima, J.M. Dawson, Laser electron accelerator, *Phys. Rev. Lett.* 43 (4) (1979) 267–270, <http://dx.doi.org/10.1103/physrevlett.43.267>.
- [3] A.J. Gonsalves, K. Nakamura, J. Daniels, C. Benedetti, C. Pieronek, T.C.H. de Raadt, S. Steinke, J.H. Bin, S.S. Bulanov, J. van Tilborg, C.G.R. Geddes, C.B. Schroeder, C. Tóth, E. Esarey, K. Swanson, L. Fan-Chiang, G. Bagdasarov, N. Bobrova, V. Gasilov, G. Korn, P. Sasorov, W.P. Leemans, Petawatt laser guiding and electron beam acceleration to 8 gev in a laser-heated capillary discharge waveguide, *Phys. Rev. Lett.* 122 (8) (2019) 084801, <http://dx.doi.org/10.1103/physrevlett.122.084801>.
- [4] J. Wenz, A. Döpp, K. Khrennikov, S. Schindler, M.F. Gilljohann, H. Ding, J. Götzfried, A. Buck, J. Xu, M. Heigoldt, W. Helm, L. Veisz, S. Karsch, Dual-energy electron beams from a compact laser-driven accelerator, *Nature Photonics* 13 (4) (2019) 263–269, <http://dx.doi.org/10.1038/s41566-019-0356-z>.
- [5] S. Li, G. Li, Q. Ain, M.S. Hur, A.C. Ting, V.V. Kulagin, C. Kamperidis, N.A.M. Hafz, A laser-plasma accelerator driven by two-color relativistic femtosecond laser pulses, *Sci. Adv.* 5 (11) (2019) eaav7940, <http://dx.doi.org/10.1126/sciadv.aav7940>.
- [6] R. Budrinas, T. Stanislauskas, J. Adamonis, A. Aleknavičius, G. Veitas, D. Gadonas, S. Balickas, A. Michailovas, A. Varanavičius, 53 w average power cep-stabilized opcpa system delivering 55 tw few cycle pulses at 1 khz repetition rate, *Opt. Express* 25 (5) (2017) 5797, <http://dx.doi.org/10.1364/oe.25.005797>.
- [7] M. Bazalova-Carter, B. Qu, B. Palma, B. Hårdemark, E. Hynning, C. Jensen, P.G. Maxim, B.W. Loo, Treatment planning for radiotherapy with very high-energy electron beams and comparison of VHEE and VMAT plans: Treatment planning for VHEE radiotherapy, *Med. Phys.* 42 (5) (2015) 2615–2625, <http://dx.doi.org/10.1118/1.4918923>.
- [8] C. DesRosiers, V. Moskvina, M. Cao, C.J. Joshi, M. Langer, Laser-plasma generated very high energy electrons in radiation therapy of the prostate, *Proc. SPIE* 6881 (2008) 688109, <http://dx.doi.org/10.1117/12.761663>.
- [9] E. Schueler, K. Eriksson, E. Hynning, B. Loo, P. Maxim, TU-H-BRC-03: Evaluation of very high-energy electron (VHEE) beams in comparison to VMAT and PBS treatment plans, *Med. Phys.* 43 (6Part36) (2016) 3766, <http://dx.doi.org/10.1118/1.4957610>.
- [10] B. Palma, M. Bazalova-Carter, B. Hårdemark, E. Hynning, B. Qu, B.W. Loo, P.G. Maxim, Assessment of the quality of very high-energy electron radiotherapy planning, *Radiother. Oncol.* 119 (1) (2016) 154–158, <http://dx.doi.org/10.1016/j.radonc.2016.01.017>.
- [11] S. N. A. Laboratory, Next linear collider test accelerator, URL: https://portal.slac.stanford.edu/sites/ard_public/facet/newnav/Pages/tnlcta/whatis.aspx.
- [12] A. Giuliotti (Ed.), *Laser-Driven Particle Acceleration Towards Radiobiology and Medicine*, in: *Biological and Medical Physics, Biomedical Engineering*, Springer International Publishing, 2016, <http://dx.doi.org/10.1007/978-3-319-31563-8>.
- [13] A. Giuliotti, G. Bussolino, L. Fulgentini, P. Koester, L. Labate, L.A. Gizzi, Laser-plasma particle sources for biology and medicine, in: *Progress in Ultrafast Intense Laser Science XII*, Springer International Publishing, 2015, pp. 151–178, <http://dx.doi.org/10.1007/978-3-319-23657-8>.
- [14] M. Durante, E. Brauer-Krisch, M. Hill, Faster and safer? Flash ultra-high dose rate in radiotherapy, *Br. J. Radiol.* 91 (1082) (2017) 20170628, <http://dx.doi.org/10.1259/bjr.20170628>.
- [15] M.-C. Vozenin, J. Hendry, C. Limoli, Biological benefits of ultra-high dose rate flash radiotherapy: Sleeping beauty awoken, *Clin. Oncol.* 31 (7) (2019) 407–415, <http://dx.doi.org/10.1016/j.clon.2019.04.001>.
- [16] J.D. Wilson, E.M. Hammond, G.S. Higgins, K. Petersson, Ultra-high dose rate (FLASH) radiotherapy: Silver bullet or fool's gold?, *Front. Oncol.* 9 (nil) (2020) nil, <http://dx.doi.org/10.3389/fonc.2019.01563>.
- [17] O. Lundh, J. Lim, C. Rechatin, L. Ammoura, A. Ben-Ismaïl, X. Davoine, G. Gallot, J.-P. Goddet, E. Lefebvre, V. Malka, J. Faure, Few femtosecond, few kiloampere electron bunch produced by a laser-plasma accelerator, *Nat. Phys.* 7 (3) (2011) 219–222, <http://dx.doi.org/10.1038/nphys1872>.
- [18] A. Ogata, T. Kondoh, J. Yang, A. Yoshida, Y. Yoshida, Lwfa of atto-second and femto-second bunches for pulse radiolysis, *Internat. J. Modern Phys. B* 21 (03n04) (2007) 447–458, <http://dx.doi.org/10.1142/s0217979207042239>.
- [19] A.R. Maier, N.M. Delbos, T. Eichner, L. Hübner, S. J alas, L. Jeppe, S.W. Jolly, M. Kirchen, V. Leroux, P. Messner, M. Schnepf, M. Trunk, P.A. Walker, C. Werle, P. Winkler, Decoding sources of energy variability in a laser-plasma accelerator, *Phys. Rev. X* 10 (2020) 031039, <http://dx.doi.org/10.1103/PhysRevX.10.031039>.
- [20] N.A.M. Hafz, T.M. Jeong, I.W. Choi, S.K. Lee, K.H. Pae, V.V. Kulagin, J.H. Sung, T.J. Yu, K.-H. Hong, T. Hosokai, J.R. Cary, D.-K. Ko, J. Lee, Stable generation of gev-class electron beams from self-guided laser-plasma channels, *Nature Photonics* 2 (9) (2008) 571–577, <http://dx.doi.org/10.1038/nphoton.2008.155>.
- [21] D. Guénot, D. Gustas, A. Vernier, B. Beaufort, F. Böhle, M. Bocum, M. Lozano, A. Jullien, R. Lopez-Martens, A. Lifschitz, J. Faure, Relativistic electron beams driven by khz single-cycle light pulses, *Nature Photonics* 11 (5) (2017) 293–296, <http://dx.doi.org/10.1038/nphoton.2017.46>.
- [22] M. Ouilé, A. Vernier, F. Böhle, M. Bocum, A. Jullien, M. Lozano, J.-P. Rousseau, Z. Cheng, D. Gustas, A. Blumenstein, P. Simon, S. Haessler, J. Faure, T. Nagy, R. Lopez-Martens, Relativistic-intensity near-single-cycle light waveforms at khz repetition rate, *Light: Sci. Appl.* 9 (1) (2020) 47, <http://dx.doi.org/10.1038/s41377-020-0280-5>.
- [23] S. Agostinelli, J. Allison, K. Amako, J. Apostolakis, H. Araujo, P. Arce, M. Asai, D. Axen, S. Banerjee, G. Barrand, F. Behner, L. Bellagamba, J. Boudreau, L. Broglia, A. Brunengo, H. Burkhardt, S. Chauvie, J. Chuma, R. Chytráček, G. Cooperman, G. Cosmo, P. Degtyarenko, A. Dell'Acqua, G. Depaola, D. Dietrich, R. Enami, A. Feliciello, C. Ferguson, H. Fesefeldt, G. Folger, F. Foppiano, A. Forti, S. Garelli, S. Giani, R. Giannitrapani, D. Gibin, J.G. Cadenas, I. González, G.G. Abril, G. Greeniaus, W. Greiner, V. Grichine, A. Grossheim, S. Guatelli, P. Gumplinger, R. Hamatsu, K. Hashimoto, H. Hasui, A. Heikkinen, A. Howard, V. Ivanchenko, A. Johnson, F. Jones, J. Kallenbach, N. Kanaya, M. Kawabata, Y. Kawabata, M. Kawaguti, S. Kelner, P. Kent, A. Kimura, T. Kodama, R. Kokoulin, M. Kossow, H. Kurashige, E. Lamanna, T. Lampén, V. Lara, V. Lefebvre, F. Lei, M. Liendl, W. Lockman, F. Longo, S. Magni, M. Maire, E. Medernach, K. Minamimoto, P.M. de Freitas, Y. Morita, K. Murakami, M. Nagamatsu, R. Nartallo, R. Nieminen, T. Nishimura, K. Ohtsubo, M. Okamura, S. O'Neale, Y. Oohata, K. Paech, J. Perl, A. Pfeiffer, M. Pia, F. Ranjard, A. Rybin, S. Sadilov, E.D. Salvo, G. Santin, T. Sasaki, N. Savvas, Y. Sawada, S. Scherer, S. Sei, V. Sirotenko, D. Smith, N. Starkov, H. Stoecker, J. Sulkimo, M. Takahata, S. Tanaka, E. Tcherniaev, E.S. Tehrani, M. Tropeano, P. Truscott, H. Uno, L. Urban, P. Urban, M. Verderi, A. Walkden, W. Wander, H. Weber, J. Wellisch, T. Wenaus, D. Williams, D. Wright, T. Yamada, H. Yoshida, D. Zschiesche, Geant4-a simulation toolkit, *Nucl. Instrum. Methods Phys. Res. A* 506 (3) (2003) 250–303, [http://dx.doi.org/10.1016/s0168-9002\(03\)01368-8](http://dx.doi.org/10.1016/s0168-9002(03)01368-8).
- [24] J. Allison, K. Amako, J. Apostolakis, H. Araujo, P.A. Dubois, M. Asai, G. Barrand, R. Capra, S. Chauvie, R. Chytráček, G. Cirrone, G. Cooperman, G. Cosmo, G. Cuttone, G. Daquino, M. Donszelmann, M. Dressel, G. Folger, F. Foppiano, J. Generowicz, V. Grichine, S. Guatelli, P. Gumplinger, A. Heikkinen, I. Hrivnacova, A. Howard, S. Incerti, V. Ivanchenko, T. Johnson, F. Jones, T. Koi, R. Kokoulin, M. Kossow, H. Kurashige, V. Lara, S. Larsson, F. Lei, O. Link, F. Longo, M. Maire, A. Mantero, B. Mascialino, I. McLaren, P.M. Lorenzo, K. Minamimoto, K. Murakami, P. Nieminen, L. Pandola, S. Parlati, L. Peralta, J. Perl, A. Pfeiffer, M. Pia, A. Ribon, P. Rodrigues, G. Russo, S. Sadilov, G. Santin, T. Sasaki, D. Smith, N. Starkov, S. Tanaka, E. Tcherniaev, B. Tome, A. Trindade, P. Truscott, L. Urban, M. Verderi, A. Walkden, J. Wellisch, D. Williams, D. Wright, H. Yoshida, Geant4 developments and applications, *IEEE Trans. Nucl. Sci.* 53 (1) (2006) 270–278, <http://dx.doi.org/10.1109/tns.2006.869826>.
- [25] J.S. Coursey, D.J. Schwab, J.J. Tsai, R.A. Dragoset, Atomic Weights and Isotopic Compositions with Relative Atomic Masses, NIST Physical Measurement Laboratory Web Page, 2015, URL: <https://www.nist.gov/pml/atomic-weights-and-isotopic-compositions-relative-atomic-masses>.
- [26] T.D. Arber, C. Bennett, C.S. Brady, A. Lawrence-Douglas, M.G. Ramsay, N.J. Sircombe, P. Gillies, R.G. Evans, H. Schmitz, A.R. Bell, C.P. Ridgers, Contemporary particle-in-cell approach to laser-plasma modelling, *Plasma Phys. Control. Fusion* 57 (11) (2015) 113001, <http://dx.doi.org/10.1088/0741-3335/57/11/113001>.
- [27] R. Lehe, A. Lifschitz, C. Thauray, V. Malka, X. Davoine, Numerical growth of emittance in simulations of laser-wakefield acceleration, *Phys. Rev. ST Accel. Beams* 16 (2013) 021301, <http://dx.doi.org/10.1103/PhysRevSTAB.16.021301>, URL: <https://link.aps.org/doi/10.1103/PhysRevSTAB.16.021301>.
- [28] Geant4 Book For Application Developers, Online book, 2019, URL: <http://geant4-userdoc.web.cern.ch/geant4-userdoc/UsersGuides/ForApplicationDeveloper/html/index.html>.
- [29] S.P.D. Mangles, C.D. Murphy, Z. Najmudin, A.G.R. Thomas, J.L. Collier, A.E. Dangor, E.J. Divall, P.S. Foster, J.G. Gallacher, C.J. Hooker, D.A. Jaroszynski, A.J. Langley, W.B. Mori, P.A. Norreys, F.S. Tsung, R. Viskup, B.R. Walton, K. Krushelnick, Monoenergetic beams of relativistic electrons from intense laser-plasma interactions, *Nature* 431 (7008) (2004) 535–538, <http://dx.doi.org/10.1038/nature02939>.
- [30] J. Faure, Y. Glinec, A. Pukhov, S. Kiselev, S. Gordienko, E. Lefebvre, J.-P. Rousseau, F. Burgy, V. Malka, A laser-plasma accelerator producing monoenergetic electron beams, *Nature* 431 (7008) (2004) 541–544, <http://dx.doi.org/10.1038/nature02963>.
- [31] C.R. Geddes, C. Toth, J. van Tilborg, E. Esarey, C.B. Schroeder, D. Bruhwiler, C. Nieter, J. Cary, W.P. Leemans, High-quality electron beams from a laser wakefield accelerator using plasma-channel guiding, *Nature* 431 (7008) (2004) 538–541, <http://dx.doi.org/10.1038/nature02900>.
- [32] H. Svensson, P. Almond, A. Brahma, A. Dutreix, H.K. Leetz, Report 35, *J. Int. Comm. Radiat. Units Meas.* os18 (2) (1984) NP, <http://dx.doi.org/10.1093/jicru/os18.2.report35>.



Improved FBX chemical dosimeter system with enhanced radiochemical yield for reference dosimetry in radiobiology and radiotherapy research

R. Polanek^{a,*}, Z. Varga^b, E. Fodor^b, Sz. Brunner^a, E.R. Szabó^a, T. Tóké^s, K. Hideghéty^a

^a ELI-ALPS, H6728, Szeged, Wolfgang Sandner u. 3, Hungary

^b University of Szeged, Faculty of Medicine, Department of Oncotherapy, H6720, Szeged, Korányi Fásor 12, Hungary

ARTICLE INFO

Keywords:

FBX chemical dosimeter
PMMA slab Phantom
Enhanced radiochemical yield
Reference dosimetry

ABSTRACT

Radiation dosimetry plays important role in the reproducibility of radiobiology experiments, in the replicability of results, as well as in the successful and safe use of radiotherapy procedures. The consistency and accuracy of the applied dosimetry methods pre-define the outcomes of these applications. This paper presents a version of the well-known ferrous sulphate – benzoic acid – xylenol orange (FBX) chemical dosimeter with improved sensitivity, accuracy and precision. Sensitivity is increased due to a slight modification in composition and the preparation procedures. We use stock solutions for the preparation of the dosimeter solution, which consists of 1 mM ferrous sulphate and 16 mM benzoic acid with 0.25 mM xylenol orange added post-irradiation. The nonlinear response to the absorbed dose of this system is eliminated by the increased ferrous sulphate concentration, permitting the calculation of the absorbed dose by a linear relationship between the absorbed dose and the optical absorbance of the solution. The measured chemical yield of our dosimeter is $9.08 \cdot 10^{-6} \text{ mol/J}$ for 6 MV photon beams and $6.42 \cdot 10^{-6} \text{ mol/J}$ for 250 kVp x-rays. This is a 24% enhancement over the original FBX solution, which permits a finer dose resolution. The accuracy and precision of our method is assured by a well-designed and consistently used practice. A custom designed multipurpose PMMA slab phantom was used for irradiation in reference conditions. This phantom can be used for irradiation in reference conditions of dosimetric solutions, dosimetric films and chemical or biological samples. The combined standard uncertainty of this system is 1.12%, which can be improved by using an appropriate temperature correction factor. Furthermore, a working protocol has been established which allows dosimetry measurements using less than 1 mL dosimetric solutions.

1. Introduction

Ferrous ammonium sulphate based chemical dosimeters are well known in dosimetry. Their most common form, known as the Fricke dosimeter system, is made from 1 mM ferrous ammonium sulphate, 1 mM sodium chloride and 0.4 M sulphuric acid, which can be used in the absorbed dose range from 20 Gy to 400 Gy. The ISO/ASTM51026-15 (2015) international standards recommend that the Fricke dosimetry system can be used as a reference standard dosimeter. However, due to time and technical constraints, it is not used in routine radiotherapy practice or radiobiological experiment dosimetry. These applications require a lower detection window with an upper dose limit of 20 Gy.

Ferrous ammonium sulphate – benzoic acid – xylenol orange (FBX) dosimeters belong to the group of ferrous sulphate based chemical dosimeters which can be used for low dose applications, up to 20 Gy. The original FBX chemical dosimeter was developed by Gupta, B.L.

(1970) and is made from 0.2 mM ferrous ammonium sulphate, 5.0 mM benzoic acid and 0.2 mM xylenol orange in 25 mM sulphuric acid. In this system benzoic acid increases the radiolytical oxidation of Fe^{2+} ions, which subsequently bind to the xylenol orange dye molecules and form a complex with an absorption line around 540 nm. This line can be subsequently detected and measured.

The radiation chemistry of this system has been studied in detail by Geisselsoder et al. (1963); Gupta et al. (1978); Gupta and Nilekani (1998); Gupta et al. (1997); Gupta (1989); Gupta et al. (1983); Jia-Shan et al. (1982). Its chemical yield has been determined for different beam qualities. For example, Gupta et al. (1976) measured the chemical yield for $^{10}B(n, \alpha)^7Li$ neutron beam, while Bhat et al. (2003) and Semwal et al. (2002) measured the response to ^{12}C and 7Li ions. Low dose rate and dose fractionation FBX dosimeter responses were also studied by Gupta and Madhvanath (1985); Gupta et al. (1981).

Thanks to its high sensitivity, the FBX dosimeter can be used for a

* Corresponding author.

E-mail address: robert.polanek@eli-alps.hu (R. Polanek).

variety of applications. Gupta et al. (1992) studied the possibilities of using the FBX dosimeter for ^{60}Co therapy unit calibration and quality assurance Gupta et al. (1992, 1982). Moussous et al. (2011) used the FBX dosimeter for measuring dosimetric parameters, and Gupta et al. (2000) studied the usability of chemical dosimetry techniques, including the FBX solution, for various applications under different geometries.

To date, several attempts have been made to further enhance the FBX dosimeter. For example, Brindha et al. (2002) introduced the stock solution techniques in the preparation process to increase the shelf-life of prepared solutions, while Upadhyay et al. (1982) modified the FBX composition to obtain a more tissue-equivalent composition, resulting in its use for neutron dosimetry.

Moreover, xylenol orange (XO) is used as an analytical tool in chemistry for the determination of iron ion concentration. The protocol established by Gay et al. (1999) to measure Fe^{3+} concentration differs slightly from the FBX method. The measured wavelength is stated as 560 nm, and the amount of the xylenol orange is increased to ensure that the absorbance of the XO-Fe complex is independent of the concentration of XO. This occurs when the XO: Fe^{3+} ratio is above 3. Xylenol orange dye is added to the Fe^{3+} ion solution before the spectrophotometric measurements using pre-prepared stock solutions. The method described by Gay et al. (1999) is recommended to measure the Fe^{3+} ions in concentrations between $5\ \mu\text{M}$ and $50\ \mu\text{M}$. We started out from this study to improve the sensitivity of our FBX dosimeter.

Ferrous ammonium sulphate based dosimetry can be considered as a precise method to measure Fe^{3+} concentration produced by ionizing radiation. This can be performed measuring the absorbance at a certain wavelength, and the dose can be calculated from this value with the following equation:

$$D = \frac{A - A_0}{\epsilon \rho d G(\text{Fe}^{3+})}, \quad (1)$$

where A and A_0 are the absorbance of irradiated and non-irradiated reference solutions, respectively, ϵ is the molar absorption coefficient, ρ is the density of the solution, d is the optical path length used in spectrophotometric determination and $G(\text{Fe}^{3+})$ is the radiochemical yield of the Fe^{3+} ions.

All quantities in Equation (1) are subject to some uncertainties. Density can be measured with relatively high precision, and its variation in the prepared solutions is negligible. The cuvette optical path length is well defined by the manufacturer, and in most cases it has a 0.5 % error. Both the molar absorption coefficient and the radiochemical yield depend on the accuracy of the measurements of the optical absorbance of solutions with different Fe^{3+} concentrations.

The relation between the relative uncertainty of the measured absorbance can be derived using the Lambert-Beer law of optical absorption. It has a minimum at $A = 0.43$, where the theoretical relative uncertainty is 0.2% Sommer (1989). Below $A = 0.2$, relative uncertainty increases considerably, and for very low absorbance, this tends to infinity. The concentration of Fe^{3+} ions in a freshly prepared FBX solution is around $1.36\ \mu\text{M}$, depending on the purity, storage time and conditions of the Fe^{2+} salt. This concentration corresponds to an absorption of $A = 0.02$ and a theoretical relative uncertainty of 1.6 % in spectrophotometric measurements.

It is well known that a more than 5% difference in absorbed dose can lead to considerable differences in the outcomes of radiobiological experiments or radiotherapy procedures. Therefore, the reproducibility of radiobiological experiments or the replicability of treatment results depend on the precision and accuracy of dosimetric measurements. The main objective of this work was to develop an FBX formula based, enhanced chemical dosimetry system to be used in radiobiological research as a routine reference dosimetry method in various irradiation arrangements where common dosimetry tools are not suitable or are difficult to use. To achieve this, a standard operational procedure has been established and validated to guarantee the necessary accuracy and

precision. Related to this, we have developed a custom designed multipurpose PMMA slab phantom to ensure reference irradiation conditions.

2. Methods

Dosimetric solutions were prepared from analytical grade reagents and HPLC grade water using suitably cleaned glassware. A high level of laboratory cleanliness was established and maintained through an in-house practice protocol. Reagents were weighed with the help of a calibrated analytical balance, precision pipettes, class A cylinders and volumetric flasks. Apart from the ferrous ammonium sulphate stock solution all prepared solutions were stored in dark media bottles with screw caps at room temperature.

2.1. Dosimeter preparation

The dosimetric solutions were prepared from pre-prepared stock solutions, based on the following preparation procedure:

- Sulphuric acid stock solution – All stock solutions were made with 25 mM H_2SO_4 , which was prepared before use from 0.5 M analytical grade sulphuric acid solution (5 mL 0.5 M H_2SO_4 dissolved in 100 mL HPLC water). The latter was obtained from concentrated H_2SO_4 solution (an ampoule contains 49.04 g H_2SO_4 , Firma Chempure) and stored in dark screw-cap bottles at room temperature.
- The ferrous ammonium sulphate stock solution (FS) – ammonium Fe^{2+} sulphate hexahydrate $((\text{NH}_4)_2\text{Fe}(\text{SO}_4)_2 \times 6\text{H}_2\text{O})$, 3.921 g, Sigma-Aldrich) was dissolved in sulphuric acid (H_2SO_4 , 25 mM, 50 mL). This was further diluted with 25 mM H_2SO_4 (100 mL). The resulting solution of ferrous ammonium sulphate (100 mM) was stored in a refrigerator to prevent the thermal oxidation of iron ions.
- The benzoic acid stock solution (BA) – benzoic acid ($\text{C}_7\text{H}_6\text{O}_2$, 1.974 g, Sigma-Aldrich) was dissolved in sulphuric acid (H_2SO_4 , 25 mM, 900 mL). This was further diluted with 25 mM H_2SO_4 (100 mL). The final solution was 16.16 mM benzoic acid. (Dissolution can be accelerated by heating.)
- The xylenol orange stock solution (XO) – xylenol orange disodium salt (, 179.16 mg, Sigma-Aldrich) was dissolved in sulphuric acid (H_2SO_4 , 25 mM, 50 mL) and was then further diluted with 25 mM H_2SO_4 (100 mL).

The dosimetric solution was prepared in a 100 mL volumetric flask using 1 mL FS stock solution diluted with the BA stock solution, which resulted in a 1 mM ferrous ammonium sulphate, 16 mM benzoic acid solution in 25 mM sulphuric acid. This solution was stored, until use, in dark screw-cap bottles or in sterile Eppendorf tubes in a refrigerator.

2.2. Reference irradiation

All irradiation was performed in reference conditions using an in-house made PMMA slab phantom and different beam qualities. A conventional LINAC ($\text{SSD} = 100\ \text{cm}$, field size $15\ \text{cm} \times 15\ \text{cm}$) was used for 6 MV and 15 MV photon beams and for 6 MeV, 9 MeV and 12 MeV electron beams, respectively. A cell and small animal irradiator facility was used (Xstrahl, RS320 type self-contained X-Ray irradiator) for 250 kVp X-ray beams ($\text{HVL} = 1.53\ \text{mm Cu}$ equivalent).

Fig. 1 shows the PMMA slab phantom which measures $30\ \text{cm} \times 30\ \text{cm}$ and has variable heights which can be changed using slabs with different thicknesses. The 2.5 cm thick sheet has a $15\ \text{cm} \times 15\ \text{cm}$ square hollow in the middle with a depth of 1.5 cm, in which different inserts with the same dimensions can be placed. These inserts are prepared to hold different sample vials: 0.5, 1.5, 2 mL Eppendorf tubes, well plates and cell culture dishes. This slab phantom can be used for the reference irradiation of dosimetric solutions, dosimetric films or both at the same time, and for the irradiation of different

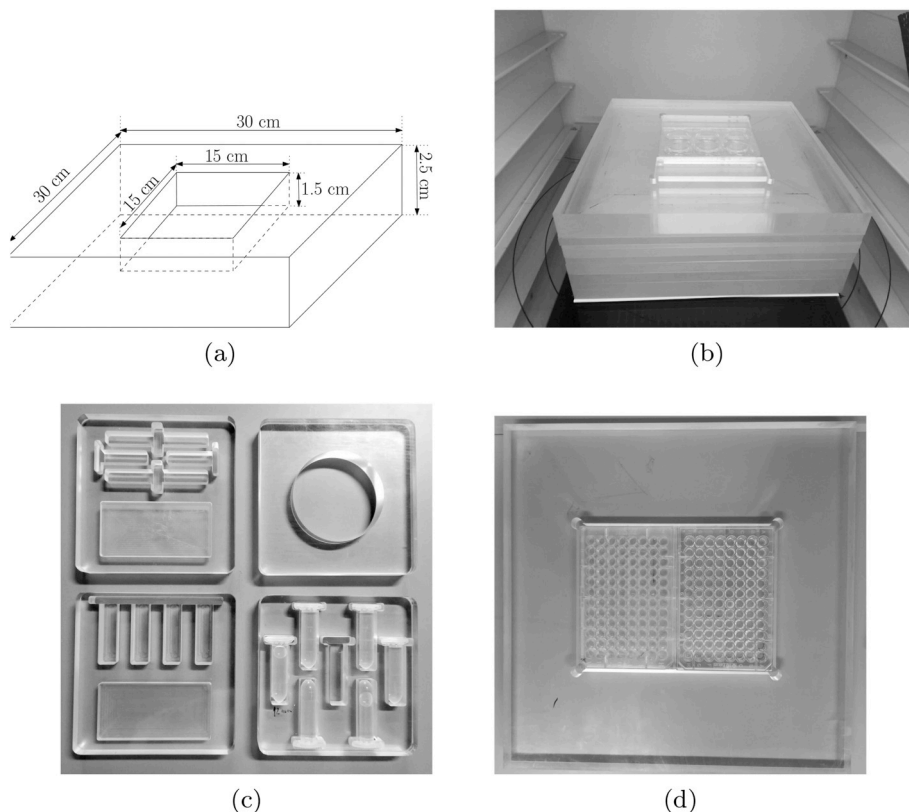


Fig. 1. Acrylic slab phantom for reference irradiation. The phantom has two functional parts: a 30 cm × 30 cm PMMA sheet with different thicknesses for variable PMMA phantom heights (1b) and a PMMA sheet with thickness of 2.5 cm with a 15 cm × 15 cm and 1.5 cm deep hollow in the middle of it which can accept inserts with the same dimensions (1a). These inserts are designed to accept different types of sample holders (1c). Another piece of 2.5 cm thick PMMA sheet is designed so it can be inserted in it one or two multi-wells plates with dosimetric solutions or biological samples (1d).

radiobiological samples (cell cultures, Zebrafish embryos etc.).

Samples for conventional LINAC irradiation were placed at an equivalent depth chosen so that 1 MU would yield the same dose as in water. This was determined by a series of measurements made with a PTW Unidose universal dosimeter and a Farmer type ionization chamber calibrated with a secondary standard in terms of absorbed dose to water.

In the cell and small animal irradiator, a beam hardening filter (consisting of a 1.06 mm aluminium foil and a 0.51 mm copper foil) was used to obtain an X-ray beam quality equivalent to $HVL = 1.53$ mm Cu. The correction factor of $k_{Q_0} = 0.9978$ was determined through the interpolation of the beam quality factors provided by the calibration laboratory. The reference dose measurements were carried out in a PTW RW3 type solid slab phantom with a PTW Farmer Chamber type 30013, and a PTW Unidos^{webline} dosimeter calibrated relative to water.

The absorbed dose was measured in a RW3 solid slab phantom used for daily calibrations. The measured dose was converted into absorbed dose to water using the manufacturer's conversion factors. Data were available neither for the 250 kVp X-ray RW3 solid slab phantom, nor for the plexi slab phantom. Consequently, a phantom dose conversion factor was determined using the procedure published by Seuntjens et al. (2005). The depth dose was measured in water at different depths (z_{ref}) and in the RW3 and PMMA slab phantoms at an equivalent depth (z_{eq}). The phantom dose conversion factor was calculated with the following equation:

$$k_{s,w}^Q = \frac{M_w^Q}{M_s^Q}, \tag{2}$$

where $k_{s,w}^Q$ is the phantom dose conversion factor, M_w^Q is the ionization chamber readings in water at reference depth, z_{ref} and M_s^Q are the ionization chamber readings in the slab phantom at equivalent depth z_{eq}

with the same Q beam quality and corrected for influence quantities.

The equivalent depth is the inverse ratio of the relative electron densities (ρ_e) in the two phantom materials using the following equation Seuntjens et al. (2005):

$$\frac{z_{eq}}{z_{ref}} = \frac{\rho_e^w}{\rho_e^s}. \tag{3}$$

This Equation (3) should be used in conjunction with a similar equation for the ratio of the reference and equivalent field size. However, for the lack of an appropriate collimator, these conditions were not reproducible and because it does not significantly affect the final results, we neglected this condition.

Table 1 shows the equivalent depth and the phantom dose conversion factor for RW3 and PMMA, and for the 250 kVp X-ray ($HVL = 1.53$ mm).

Table 1
Phantom dose conversion factor for RW3 and PMMA materials.

Water	RW3	PMMA		
z_{ref} (cm)	z_{eq} (cm)	$k_{s,w}^Q$	z_{eq} (cm)	$k_{s,w}^Q$
0.5	0.5	0.9539	0.4	0.9329
1.0	1.0	0.9492	0.9	0.9262
1.5	1.5	0.9421	1.3	0.9128
2.0	2.0	0.9241	1.7	0.8874
2.5	2.5	0.9158	2.2	0.8762
3.0	3.0	0.9122	2.6	0.8633
3.5	3.5	0.9083	3.0	0.8490
4.0	4.0	0.8893	3.5	0.8270
4.5	4.4	0.8837	3.9	0.8183
5.0	4.9	0.8785	4.3	0.8011

2.3. Spectrophotometric measurements

After irradiation, 0.1 mL xylenol orange stock solution (XO) was added to each 0.9 mL of irradiated dosimetric solution. The final solution contained 0.25 mM xylenol orange disodium salt. After waiting at least 10 min for the xylenol orange to form complexes with the Fe^{3+} ions Gay et al. (1999), we measured the solution's absorbance at 560 nm against the xylenol orange blank solution. The blank sample was prepared in a sample vial from the XO stock solution (0.1 mL) and sulphuric acid (0.9 mL 25 mM), in the same manner as the dosimetric samples.

Absorption measurements were performed using an UV-VIS spectrophotometer (Lambda 35, PerkinElmer, double light path) and a quartz cuvette with a 1 cm path length. The recommendation of the ISO/ASTM 51026:2014 standard was followed to ensure the reproducibility and accuracy of the measurements.

2.4. Density measurements

The density of the eFBX solution was measured with an Anton Paar DMA 35 portable density meter (accuracy, 0.001 g/cm^3) and the classical gravimetric method. The results of the two methods were compared and a mean value was generated.

2.5. Determination of the molar mass absorption coefficient

A simplified version of the recommendations of ISO/ASTM 5106:2014 were followed to determine the molar absorption coefficient. An Fe^{3+} stock solution was prepared by dissolving ammonium iron(III) sulphate dodecahydrate (Sigma Aldrich, 4.82 mg) in sulphuric acid (25 mM, 50 mL), and was then diluted down to 100 mL. From this stock solution and the BA stock solution a series of samples were prepared with Fe^{3+} ion concentrations between $10 \mu\text{M}$ and $60 \mu\text{M}$, and 0.1 mL XO stock solution was added to each 0.9 mL solution.

The concentration of Fe^{3+} ions for each sample was determined by measuring absorption at 560 nm. The molar linear absorption coefficient was obtained from the gradient of the plot of the absorbance/path length versus concentration.

2.6. Determining the radiochemical yield of ferric ions

The radiochemical yield of ferric ions $G(Fe^{3+})$ was determined using a freshly prepared eFBX solution that was irradiated with different doses in 2 mL Eppendorf tubes using the PMMA slab phantom and the reference irradiation geometry. Optical absorption was measured for irradiated and nonirradiated samples and $\Delta A_i = A_i - A_0$ were calculated, where A_i is the absorption of the irradiated sample and A_0 is the absorption of the nonirradiated sample.

Plotting $\Delta A/\varepsilon\rho$ values as a function of dose results in a linear correlation where the gradient corresponds to the radiochemical yield of ferric ions ($G(Fe^{3+})$).

2.7. Dose determination

Whenever possible, we irradiated at least three FBX samples, together or separately, with the same dose. After irradiation we performed spectrophotometric measurements, and using Equation (1) we calculated the absorbed dose from the obtained absorption value.

The absorbed dose to water, D_w , can be determined from the mean absorbed dose using the relation:

$$D_{\text{water}}^{\text{ref}} = k_{w, \text{PMMA}} \cdot D_{\text{PMMA}}^{\text{ref}} \quad (4)$$

where $k_{w, \text{PMMA}}$ is the PMMA to water conversion factor, calculated as the ratio of the measured dose in water at reference depth ($D_{\text{water}}^{\text{ref}}$) and the dose in PMMA at equivalent depth ($D_{\text{PMMA}}^{\text{ref}}$).

2.8. Diluted eFBX solution measurements

For the measurement of doses with volumes less than 1 mL, the irradiated eFBX solution was diluted with a well defined amount of nonirradiated eFBX solution. XO stock solution was added to these diluted eFBX solutions. Based on the degree of dilution, the change in absorbance induced by the absorbed dose can be calculated with the following formula:

$$\Delta A = \frac{A_m - \left(1 - \frac{1}{9}\beta\right)A_0}{0.9 - \beta}, \quad (5)$$

where ΔA is the change in absorbance, A_m is the measured absorbance of samples without correction, A_0 is the absorbance of the non-irradiated solution and β is equal to the ratio of the solvent volume and the total volume of samples $\beta = V_0/V_T$.

3. Results and discussions

To improve the sensitivity of the FBX dosimeter, attempts have been made to increase the chemical yield of ferric ions and to enhance the photometric measurement techniques by applying Gay et al. (1999) recommendation. We performed a series of experiments varying the chemical composition to increase the sensitivity of the FBX dosimetric solution.

It is well known that the radiochemical yield of Fe^{3+} ions is higher in the ferrous sulphate – benzoic acid system (FB) than in the ferrous sulphate – benzoic acid – xylenol orange system (FBX) Gupta et al. (1978).

The primary species formed by radiolysis in aqueous solutions are the H, OH, H_2O_2 and H_2 radicals. In the FB system each hydrogen atom oxidizes two ferrous ions, and each hydrogen-peroxide molecule oxidizes one ferrous ion, while one hydroxyl radical is produced. This secondary hydroxy radical reacts with benzoic acid and forms hydroxycyclohexadienyl radicals, which oxidize the ferrous ions in a chain reaction Jia-Shan et al. (1982):



Concurrently, benzoic acid can effectively compete with oxygen for H atom releasing HO_2 radicals Gupta et al. (1978). Gupta et al. (1978) showed that the radiochemical yield for the FB system can be written as:

$$G(Fe^{3+}) = 12 \cdot G_{H_2O_2} + 11 \cdot G_{OH} + 13 \cdot G_H, \quad (7)$$

where $G_{H_2O_2} = 0.79 \cdot 10^{-7} \text{ mol/J}$, $G_{OH} = 2.9 \cdot 10^{-7} \text{ mol/J}$ and $G_H = 3.5 \cdot 10^{-7} \text{ mol/J}$ are the radiochemical yield of hydrogen peroxide, hydroxyl radical and atomic hydrogen, respectively.

However, in the FBX system, H_2O_2 oxidizes 8 ferrous ions, instead of 12, and the xylenol orange competes for OH radicals with benzoic acid, producing $XO \cdot OH$ radical, which can oxidize one ferrous ion. According to Jia-Shan et al. (1982) and Gupta et al. (1978) the reaction chain length of the oxidation of Fe^{2+} decreases and the Equation (7) can be written as:

$$G(Fe^{3+}) = 8 \cdot G_{H_2O_2} + 7 \cdot G_{OH} + 11 \cdot G_H. \quad (8)$$

The main drawback of the FB system is that there is a nonlinear response to dose. This behaviour was reported by Gupta et al. (1978) and shown in Fig. 2, where the dose response of the Fricke and FBX dosimeters is nonlinear above 5 Gy in the FB system. This behaviour can be qualitatively explained by the spur theory of water radiolysis, which states that the initial radiolysis species of water exist in a spur. These species then diffuse in the medium and react forming intermediates and the final product, Fe^{3+} ions. The probability of interaction with Fe^{2+} ions is determined on the basis of the concentration of Fe^{2+} ions and the initial radiolysis species, as well as the spatial distribution

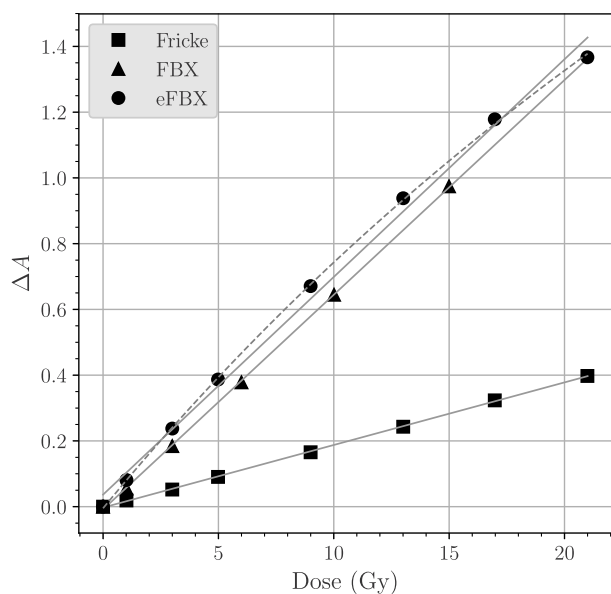


Fig. 2. Dose response curve of different dosimetric solutions for a standard Fricke solution, measured with xylenol orange techniques; an FBX solution and an FB solution.

of these spurs. The spatial distribution of spurs is strongly related to the linear energy transfer (LET) value of radiation. At high LET, spurs are superposed, whilst at low LET the spatial distribution of spurs is scattered. This means that:

- the radiochemical yield of ferric ions is lower at high than at low LET radiations, because the probability of a reaction with a Fe^{2+} ion is higher when the spatial distribution of spurs is scattered, and
- the probability of a reaction with a Fe^{2+} ion at the same LET radiation level is higher in case of higher Fe^{2+} ion concentrations.

Consequently, the nonlinearity of the FB solution suggests that the solution becomes saturated at high doses, which means that there is a reduced probability of a reaction with a Fe^{2+} . This in turn leads to a decreasing chemical yield, which prompted us to remove the non-linearity of the system by increasing the Fe^{2+} concentration. Fig. 3 shows the effects of increasing the ferrous ammonium sulphate concentration from 0.2 mM to 1 mM, which corresponds to the ferrous ammonium sulphate concentration of the classical Fricke dosimeter.

Studying the relation between the response of the FB system and the concentration of benzoic acid has revealed that the chemical yield of Fe^{3+} ions can improve if the amount of benzoic acid is increased in the system. The variation of absorbance as a function of BA concentration is shown in Fig. 4. When the FB samples with increased benzoic acid concentration were irradiated with 4 Gy, the response showed saturation effects, which became significant above 7.5 mM of benzoic acid. However, the response curve was not completely saturated in the measured concentration range. The extrapolation of the data revealed that complete saturation occurs above 16 mM.

On the other hand, variations in benzoic acid concentrations, due to poor measurement or improper dilution do not significantly influence the dosimetric response of the solution. Fig. 4 shows that a change in the BA concentration from the standard 5 mM–16 mM results in an 8% increase in absorbance, which corresponds to an 8% growth in radiochemical yield. At the same time, there is a 0.3% difference in absorbance at 14 mM and 16 mM. Therefore, at higher benzoic acid concentrations the error which may occur in the solution preparation process is negligible.

A further increase in benzoic acid concentration is hindered by its poor solubility in water (21.9 mM at 18 °C). No further improvements in

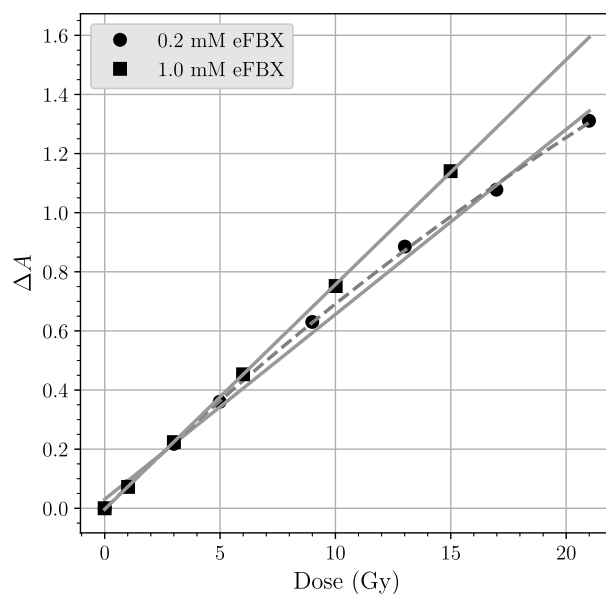


Fig. 3. The effects of increased ferrous sulphate concentrations. The lower line is the graph of linear fitting of the measurement points (marked with circles) in case of eFBX solutions with 0.2 mM ferrous sulphate concentration. The dashed line is the graph of fitting with a rational function of the same measurements points. The upper line represents the graph of linear fitting of the measurements points (marked with squares) obtained with 1 mM ferrous sulphate concentration.

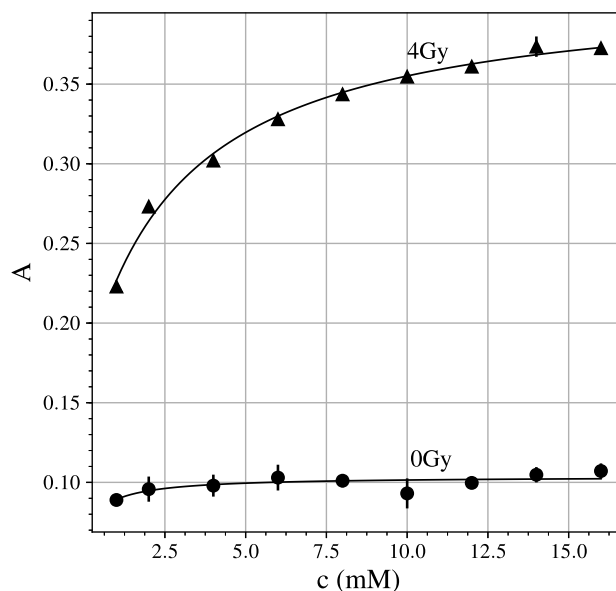


Fig. 4. Optical absorbance as a function of benzoic acid concentration for irradiated solution and for nonirradiated solution.

absorbance are expected above 16 mM, so there is no point in experimenting with even higher concentrations.

The radiochemical yield of Fe^{3+} ions in an FB solution with 5 mM benzoic acid concentration can be calculated using Equation (7) and is found to be $8.75 \cdot 10^{-6}$ mol/J. These measurements show that the radiochemical yield of dosimetric solutions with 16 mM is $9.08 \cdot 10^{-6}$ mol/J for a beam quality of 6 MV. This equals a 3.9% increase in yield, and is due to the higher benzoic acid concentration. Using the logic proposed by Jia-Shan et al. (1982) we can conclude that in the presence of 16 mM benzoic acid, the OH radical oxidizes 12 rather than 11 Fe^{3+} ions, and Equation (7) becomes:

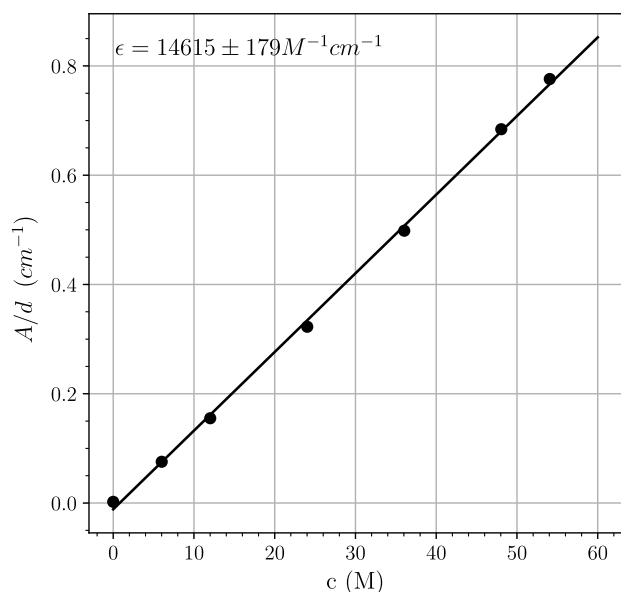


Fig. 5. Graphical representation of absorbance variation as a function of Fe^{3+} ion concentrations. The gradient is the molar attenuation coefficient, $\epsilon = 14615 \pm 18 M^{-1} cm^{-1}$.

$$G(Fe^{3+}) = 12 \cdot G_{H_2O_2} + 12 \cdot G_{OH} + 13 \cdot G_H. \quad (9)$$

By using a concentration of 16 mM benzoic acid, and by irradiating an FB solution instead of an FBX solution, the radiochemical yield can be increased from a mean literature value of $6.89 \cdot 10^{-6}$ mol/J, to $9.08 \cdot 10^{-6}$ mol/J, which equals to a 24% enhancement. We named this system enhanced FBX (eFBX).

Our eFBX dosimetric solution has a density of $0.9978 g/cm^3$, and the measured molar attenuation coefficient is $14615 \pm 18 M^{-1} cm^{-1}$, which was obtained by fitting the measured absorbance at different Fe^{3+} concentrations (Fig. 5). This value is in agreement with literature values, and any difference may be attributed to the degree of purity of xylenol orange dyes, which varies from manufacturer to manufacturer. This is a common problem, and it is always recommended to measure the molar attenuation coefficient when a new lot of xylenol orange is used. A summary of different molar absorption coefficient values was published by Moussous et al. (2008).

The radiochemical yields of ferric ions resulting from different beam qualities are presented in Table 2. All values are in terms of dose to water, and were determined by applying the appropriate conversion factors.

The effects of the dilution of the irradiated solution were investigated to perform measurements with dosimetric solutions of less than 1 mL, for example solutions from single wells of a 96-well plate, $250 \mu L$. Table 3 shows $G(Fe^{3+})$ values for various diluted eFBX solutions, and it can be seen that to some extent the radiochemical yield values

Table 2
The radiochemical yield of the eFBX dosimetric solution for different beam qualities.

Beam	$G(Fe^{3+})$ $mol \cdot J^{-1}$
6 MV photon	$9.08 \pm 0.17 \cdot 10^{-6}$
15 MV photon	$9.10 \pm 0.17 \cdot 10^{-6}$
6 MeV e^-	$8.98 \pm 0.15 \cdot 10^{-6}$
9 MeV e^-	$9.03 \pm 0.08 \cdot 10^{-6}$
12 MeV e^-	$8.97 \pm 0.26 \cdot 10^{-6}$
250 kVp X-ray	$6.46 \pm 0.08 \cdot 10^{-6}$

Table 3

The radiochemical yield of diluted eFBX dosimetric solution for different dilutions grades. All values refer to 250 kVp X-ray beam quality.

Dilution	Sample	Solvent	$G(Fe^{3+})$
	ml	ml	$mol \cdot J^{-1}$
4/0.9	0.9	2.6	$6.07 \pm 0.18 \cdot 10^{-6}$
4/0.5	0.5	3.1	$5.86 \pm 0.23 \cdot 10^{-6}$
4/0.25	0.25	3.35	$5.88 \pm 0.23 \cdot 10^{-6}$

differ for diluted and nondiluted solutions. This can be attributed to some matrix effects the origins of which have not yet been identified.

We established a standardized measurement protocol to ensure that eFBX is an easy-to-handle chemical dosimeter. For this purpose, we started out from the ISO standard on the practice for using the Fricke reference standard dosimetry system. Our protocol describes the preparation, handling and storage of the solution; irradiation in reference conditions; the photometric measurements and subsequent data processing.

Stock solutions were introduced similarly to Brindha et al. (2002) with some modifications for the preparation of dosimetric solutions. All but one of the stock solutions were stored at room temperature. The 1 mM FS stock solution was stored in a refrigerator due to its short, two-week shelf-life (caused by the relatively high thermal oxidation rate of ferrous ammonium sulphate, which is a function of Fe^{2+} ion concentration and temperature). The BA and XO stock solutions can be stored at room temperature for a long time without any observable degradation.

The initial ferric ion concentration depends on the thermal oxidation of the dosimetric solution, which reduces the measurable dose range. The freshly prepared eFBX solution has an optical absorption of 0.1, which can increase to 0.3 with a change in ferric ion concentration over time. For this reason it is always recommended to use freshly prepared FS stock solutions to avoid any uncontrolled change in dosimetric solution consistency, and to ensure complete control over the quality of dosimetric solutions.

Fig. 6 shows that the blank solution has considerable absorption at the maximum absorption wavelength (525 nm) of the eFBX system. This means that the Beer-Lambert law cannot be used here. A

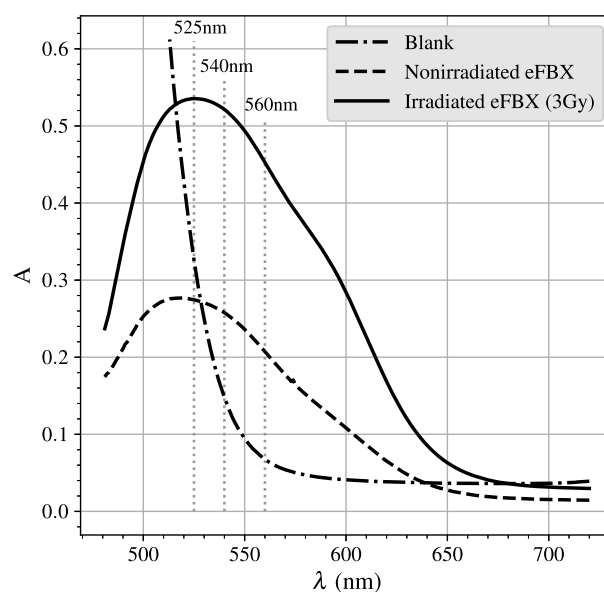


Fig. 6. The absorption spectra of the blank solution and of the irradiated eFBX solution. The dotted vertical lines represent the wavelengths for maximum absorptions and for the actual measurement wavelength.

Table 4

Uncertainty budget of the eFBX solution. Temperature correction was calculated based on the relations used for the Fricke dosimeter ISO/ASTM51026-15 (2015) as the temperature dependence measurement has not yet been performed. The combined standard uncertainty without this term becomes 1.0%.

Source of uncertainty	Relative standard uncertainty (%)	
	Type A	Type B
<i>Reference dose rate</i>		
N_k secondary standard	–	0.20
Positioning	–	0.02
Temperature and pressure correction	0.03	0.10
Measurement of current	0.05	0.10
<i>Calibration of OFBX solution</i>		
Positioning of dosimeter	–	0.02
N_{pw} plexi-water conversion	0.20	–
Photometric and volumetric correction	0.35	0.61
G value determination	0.6	–
ϵ determination	0.2	–
Temperature correction	–	0.50
Quadratic summation	0.75	0.83
Combined standard uncertainty	1.12	
Extended uncertainty ($k = 2$)	2.24	

convenient method is to measure absorption at a different wavelength where there are no considerable xylenol orange absorptions Gay et al. (1999). Hence, all photometric measurements were conducted at 560 nm, in accordance with the observations of Gay et al. (1999).

It is also interesting to note that the xylenol orange technique can be successfully applied to standard Fricke solutions in the low dose domain. The initial concentration of ferric ions is the same as in the case of the eFBX solution, and the chemical yield of the Fricke solution is 1.6 mol/J ISO/ASTM51026-15 (2015). The concentration change induced by irradiation can be measured with the xylenol orange technique. If we apply this technique to the Fricke solution, the chemical yield is $1.62 \cdot 10^{-6}$ mol/J for a 6 MV photon beam and $1.44 \cdot 10^{-6}$ mol/J for a 250 kVp X-ray beam, respectively.

3.1. Uncertainty budget

Table 4 summarizes the uncertainty budget for eFBX dosimeter calibration, made using the recommendations of IAEA International Atomic Energy Agency (2009). In this phase we encountered two major problems: the uncertainty of spectrophotometric measurements and that introduced by pipetting.

Theoretically, the most precise value for absorbance is $A = 0.434$, which is the minimum of function:

$$\frac{dA}{A} = -\frac{0.434}{10^{-A}} dT, \quad (10)$$

where A is the absorbance and dT is the standard deviation of transmittance. Equation (10) can be obtained using the Lambert-Beer law Sommer (1989) (Fig. 7). The graph shows that the uncertainty of measurements at low absorbance is relatively high. In a freshly prepared eFBX dosimeter solution, absorbance is usually between 0.01 and 0.02, and increases with storage time. The relative uncertainty of absorption is between 3.12% and 1.6%. However, a rise in the concentration of ferrous sulphate to 1 mM in the eFBX dosimetric solution increases the absorbance of the freshly prepared solution to 0.1 with a theoretical relative uncertainty of 0.38%.

The final ferric ion concentration of the eFBX solution is determined both by the absorbed dose and by the pipetting of the solution after irradiation. Section 2 states that for sample preparation 0.9 mL eFBX

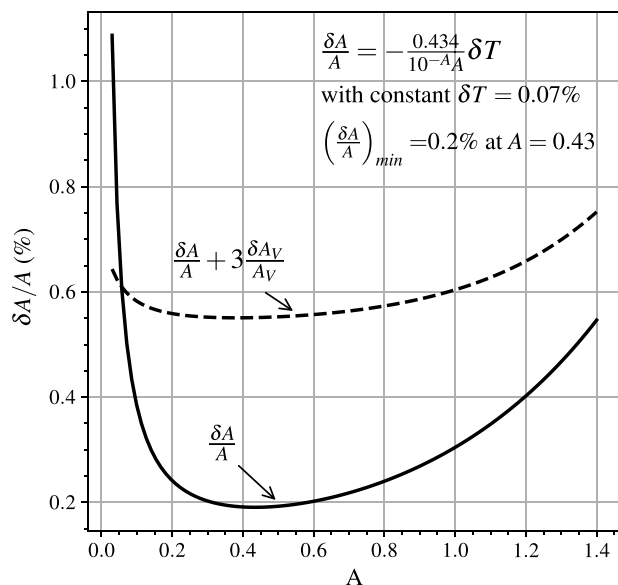


Fig. 7. The relative uncertainties for the eFBX dosimeter due to the photometric measurements (solid curve) and due to the combination of photometric and volume measurements (dashed line).

solution was extracted from the irradiated sample and 0.1 mL XO stock solution was added. Therefore, the final concentration of the solution was $0.9 \text{ ml} \cdot c_0 / (0.9 + 0.1) \text{ ml}$, where c_0 is the initial ferric ion concentration. If we apply the rule of propagation of uncertainty we obtain:

$$\left(\frac{\delta A_B}{A_B}\right)^2 = n \cdot \left(\frac{\delta V}{V}\right)^2 + \left(\frac{\delta A_m}{A_m}\right)^2 + \left(\frac{\delta A_0}{A_0}\right)^2, \quad (11)$$

where $\delta A_B/A_B$ is the total uncertainty of absorbance of the irradiated solution; $\delta A_m/A_m$ is the uncertainty of absorbance of the irradiated solution; $\delta A_0/A_0$ is the uncertainty of absorbance of the nonirradiated solution, which is discussed here separately, because low absorbance results in higher uncertainty, and $\delta V/V$ is the uncertainty associated with pipetting. The parameter n represents the volumes which were measured with pipette. For example, two samples of 0.9 mL can be extracted with a 1 mL pipette from a single 2 mL Eppendorf tube. With the addition of the XO stock solution the parameter n increases to 3. In an ideal situation, the uncertainty attributed to volume determination with a precise pipette is 0.2%. Equations (10) and (11) provide the combined uncertainties for absorbance measurements represented in Fig. 7 (dotted line).

Fig. 7 shows that the uncertainty introduced by pipetting resulted in a greater but flatter relative uncertainty in absorbance measurements. In the 0.1 to 1.2 absorbance interval, the relative uncertainty is between 0.64% and 0.65% with a minimum of 0.55%. This absorption interval corresponds to an absorbed dose range up to 9 Gy for 6 MV photon beams and up to 12 Gy for 250 kVp X-ray (with a $HVL = 1.53$ mm Cu equivalent).

Table 4 summarizes these calculations and considers other sources of errors. The combined standard uncertainty can be considerably improved by eliminating uncertainty type B assigned to temperature correction. Temperature correction was not considered in this study, but on the basis of the spur theory and the increased amount of ferrous sulphate in the final composition, a similar relation can be assumed between temperature and radiochemical yield as in case of the Fricke dosimeter ISO/ASTM51026-15 (2015). The same connection is true for the temperature correction of absorbance measurements, which is related to the associated volume change with temperature. Correction for this variation means that the combined standard uncertainty becomes 1.0%.

4. Conclusions

In this paper we studied some of the properties of the well-known FBX dosimetric solution in terms of sensitivity and dose range. The photometric determination of ferric ions is the major obstacle to obtaining good results with low uncertainties. This problem can be eliminated by improving the sensitivity of the solution, which we achieved by increasing the benzoic acid concentration and by adding xylenol orange dye after irradiation. Nonlinearity, a hallmark of an FB system, was eliminated by increasing the ferrous sulphate concentration from the original 0.2 mM value to 1 mM.

For reference irradiation, we constructed a special, multipurpose PMMA slab phantom to hold Eppendorf tubes filled with dosimetric solutions. This phantom can also be used for irradiation under the same conditions as those used for biological and/or chemical samples kept in cell culture dishes or multi-well plates. Moreover, one can perform the cross-calibration of the eFBX dosimeter with other dosimeters, such as films, ionization chambers etc.

Further improvements to the system can be made by studying the influence of temperature on chemical yield and absorbance measurements. If there is indeed a relation between chemical yield and temperature, and between absorbance and temperature, the obtained 1.12% combined standard uncertainty can be further reduced to 1.0%.

We are planning to conduct further experiments to make our reference dosimetry system more widely accepted. Our aim is to further optimize and refine the dosimetric characteristics and measurement practices and to ensure the reliability of this system as a reference dosimeter. It is also crucial to prove its suitability in various practical situations, especially in the dosimetry of radiobiological experiments, as well as in radiotherapy measurements.

CRedit authorship contribution statement

R. Polanek: Conceptualization, Methodology, Investigation, Validation, Formal analysis, Writing - original draft. **Z. Varga:** Methodology, Investigation, Validation, Supervision. **E. Fodor:** Validation, Visualization. **Sz. Brunner:** Investigation, Resources. **E.R. Szabó:** Investigation, Resources. **T. Tórkés:** Investigation, Writing - review & editing. **K. Hideghéty:** Conceptualization, Supervision, Writing - review & editing, Project administration.

Declaration of competing interest

The authors declare that they have no known competing financial interests or personal relationships that could have appeared to influence the work reported in this paper.

Acknowledgements

This work was supported in part by the European Union through the ELI-ALPS Project (GINOP-2.3.6-15-2015-00001) and co-financed by the European Regional Development Fund and in part by the European Union's Horizon 2020 research and innovation programme under grant agreement No. 654148 and No. 871124 Laserlab-Europe.

We are indebted to K. Mogyorósi for his valuable guidance, and to Cs. Janáky and Z. Vajna for their technical support.

References

Bhat, N., Choudhary, D., Sarma, A., Gupta, B., Siddappa, K., 2003. Response of an FBX

- dosimeter to high LET 7Li and 12C ions. *Radiat. Phys. Chem.* 68, 909–916. [https://doi.org/10.1016/s0969-806x\(03\)00112-9](https://doi.org/10.1016/s0969-806x(03)00112-9).
- Brindha, S., Rose, J., Sathyan, S., Singh, I.R.R., Ravindran, B.P., 2002. Modified ferrous ammonium sulfate benzoic acid xylenol orange (MFBX) and thermoluminescent dosimeters – a comparative study. *Phys. Med. Biol.* 47, N153–N158. <https://doi.org/10.1088/0031-9155/47/11/403>.
- Gay, C., Collins, J., Gebicki, J.M., 1999. Determination of iron in solutions with the ferric-xylenol orange complex. *Anal. Biochem.* 273, 143–148. <https://doi.org/10.1006/abio.1999.4207>.
- Geisselsoder, J., Kingkade, M.J., Laughlin, J.S., 1963. The radiation chemistry of aqueous ferrous sulfate-benzoic acid solutions. *Radiat. Res.* 20, 263. <https://doi.org/10.2307/3571532>.
- Gupta, B., 1989. Radiation chemistry of xylenol orange in aqueous solutions at different acidities. *Int. J. Radiat. Appl. Instrum. C Radiat. Phys. Chem.* 33, 75–80. [https://doi.org/10.1016/1359-0197\(89\)90097-0](https://doi.org/10.1016/1359-0197(89)90097-0).
- Gupta, B., Bhat, R., Narayan, G., Nilekani, S., 2000. Chemical dosimetry techniques for various applications under different geometries. *Radiat. Phys. Chem.* 59, 81–90. [https://doi.org/10.1016/s0969-806x\(00\)00187-0](https://doi.org/10.1016/s0969-806x(00)00187-0).
- Gupta, B., Bhat, R., Narayan, G., Susheela, B., 1983. Acid and xylenol orange effects in the FBX dosimeter. *Int. J. Appl. Radiat. Isot.* 34, 887–890. [https://doi.org/10.1016/0020-708x\(83\)90148-5](https://doi.org/10.1016/0020-708x(83)90148-5).
- Gupta, B., Kini, U., Bhat, R., 1976. Sensitivity of ferrous sulphate-benzoic acid-xylenol orange dosimeter (FBX system) to $^{10}\text{B}(n, \alpha)^7\text{Li}$ recoils. *Int. J. Appl. Radiat. Isot.* 27, 31–34. [https://doi.org/10.1016/0020-708x\(76\)90165-4](https://doi.org/10.1016/0020-708x(76)90165-4).
- Gupta, B., Kini, U., Bhat, R., 1981. Dose-rate and fractionation studies with FBX dosimeter. *Int. J. Appl. Radiat. Isot.* 32, 701–704. [https://doi.org/10.1016/0020-708x\(81\)90017-x](https://doi.org/10.1016/0020-708x(81)90017-x).
- Gupta, B., Kini, U., Bhat, R., Madhvanath, U., 1982. Use of the FBX dosimeter for the calibration of Cobalt-60 and high-energy teletherapy machines. *Phys. Med. Biol.* 27, 235–245. <https://doi.org/10.1088/0031-9155/27/2/005>.
- Gupta, B., Madhvanath, U., 1985. $G(\text{Fe}^{3+})$ values in the FBX dosimeter at low dose-rates. *Int. J. Appl. Radiat. Isot.* 36, 985–987. [https://doi.org/10.1016/0020-708x\(85\)90261-3](https://doi.org/10.1016/0020-708x(85)90261-3).
- Gupta, B., Narayan, G., Bhat, R., Kini, U., Ramaswamy, R., Suseela, B., 1992. Use of the FBX dosimeter for the quality assurance of 60Co and high energy teletherapy machines by mail. *Phys. Med. Biol.* 37, 2095–2102. <https://doi.org/10.1088/0031-9155/37/11/006>.
- Gupta, B., Nilekani, S., 1998. Ferrous ion oxidations by H, OH and H₂O₂ in aerated FBX dosimetry system. *Radiat. Phys. Chem.* 53, 643–650. [https://doi.org/10.1016/s0969-806x\(97\)00283-1](https://doi.org/10.1016/s0969-806x(97)00283-1).
- Gupta, B., Nilekani, S., Bhat, R., Narayan, G., 1997. Free radical reactions in the FBX dosimetric system at low doses and dose-rates. *Radiat. Phys. Chem.* 49, 67–70. [https://doi.org/10.1016/s0969-806x\(96\)00108-9](https://doi.org/10.1016/s0969-806x(96)00108-9).
- Gupta, B.L., Bhat, R.M., Gomathy, K.R., Susheela, B., 1978. Radiation chemistry of the ferrous sulfate-benzoic acid-xylenol orange system. *Radiat. Res.* 75, 269. <https://doi.org/10.2307/3574902>.
- Gupta, B.L., 1970. A Low-Level Chemical Dosimetry System. Chemistry and Metallurgy Committee, India Technical Report INIS-MF-209. Department of Atomic Energy, Bombay (India).
- International Atomic Energy Agency, 2009. Calibration of reference dosimeters for external beam radiotherapy. I. A. E. A. OCLC 463338844.
- ISO/ASTM51026-15, 2015. Standard Practice for Using the Fricke Dosimetry System. ASTM International, West Conshohocken.
- Jia-Shan, Z., Zhi-Li, W., Xin-Wei, C., 1982. Studies on the reaction mechanism in the irradiation of solutions containing ferrous ions, benzoic acid and xylenol orange. *Radiat. Phys. Chem.* 19 (1977), 439–441. [https://doi.org/10.1016/0146-5724\(82\)90134-0](https://doi.org/10.1016/0146-5724(82)90134-0).
- Moussou, O., Medjadj, T., Benguerba, M., 2011. FBX aqueous chemical dosimeter for measurement of dosimetric parameters. *Appl. Radiat. Isot.* 69, 399–402. <https://doi.org/10.1016/j.apradiso.2010.10.001>.
- Moussou, O., Yahiche, K., Medjadj, T., 2008. Study of the metrological characteristics of the FBX dosimeter in the photon beam using a secondary standard. *Proc. Sixth Nucl. Part. Phys. Conf.* 477–484.
- Semwal, M.K., Banerjee, M., Sarma, A., Vidyasagar, P.B., 2002. Response of the FBX system to a carbon beam: its potential as a dosimeter in heavy particle radiotherapy. *Phys. Med. Biol.* 47, N179–N183. <https://doi.org/10.1088/0031-9155/47/12/403>.
- Seuntjens, J., Olivares, M., Evans, M., Podgorsak, E., 2005. Absorbed dose to water reference dosimetry using solid phantoms in the context of absorbed-dose protocols. *Med. Phys.* 32, 2945–2953. <https://doi.org/10.1118/1.2012807>.
- Sommer, L., 1989. *Analytical Absorption Spectrophotometry in the Visible and Ultraviolet: the Principles*. Elsevier, Amsterdam New York.
- Upadhyay, S., Reddy, A., Gupta, M., Nagaratnam, A., 1982. A tissue-equivalent modified FBX dosimetric system. *Int. J. Appl. Radiat. Isot.* 33, 47–49. [https://doi.org/10.1016/0020-708x\(82\)90205-8](https://doi.org/10.1016/0020-708x(82)90205-8).